Doctoral Dissertation

Surface atomic-layer superconductors modified by adsorption of organic molecules

(有機分子吸着により変調された表面原子層超伝導体の研究)

Kenta Yokota

Department of Condensed Matter Physics
Graduate School of Science

Hokkaido University

March 2023

Contents

Chapter 1 Introduction

1.1 Background

1.1.1 Superconductivity

In 1911, Kamerlingh Onnes discovered a peculiar phenomenon in which the electrical resistance of Hg becomes zero at a certain temperature as it cools down. This phenomenon was named superconductivity, and similar phenomena were reported in various other metals. The superconductors have two fundamental properties: perfect conductivity and perfect diamagnetism (the Meissner effect). These phenomena and the thermodynamic properties of superconductivity were explained by the London and Ginzburg-Landau theories, but they were phenomenological theories, and the mechanism of superconductivity remained a mystery for a long time. However, this problem was solved by the BCS theory proposed by Bardeen, Cooper, and Schrieffer in 1957. According to the BCS theory, superconductivity occurs when electrons form electron pairs, called Cooper pairs, which are quantum mechanically identical. In the superconducting state, phonon-mediated attractive interactions between electrons on the Fermi surface create a bound state with energies lower than the Fermi level. As the electron-lattice interaction increases, the superconducting transition temperature (T_c) also increases. The BCS theory predicts a maximum T_c of about 30-40 K, but the discovery of cuprate superconductors has overturned this prediction [1, 2]. The mechanism of superconductivity in cuprate superconductors cannot be explained by the BCS theory, and no unified view has yet been obtained. Such superconductors that do not fit into the framework of BCS theory are called unconventional superconductors, and various other material groups, such as iron-based superconductors, have been reported in addition to cuprate superconductors [3]. On the other hand, by the end of 2022, the material group that has recorded the highest T_c is hydrogen-based compounds under high pressure, with zero resistance observed above 250 K in $LaH_{10 \pm x}$ at 188 GPa [4]. The isotope effects in hydrogen-based compounds are in good agreement with BCS theory, suggesting that they are conventional superconductors. Thus, the scope of superconductivity research continues to expand and fascinate researchers today.

Materials that exhibit high T_c at normal pressure are often layered materials. Cuprate superconductors, which are typical high-temperature superconductors, also belong to layered materials and are essentially insulators. It is known that superconductivity appears

when carriers are doped in the CuO_2 layer, which serves as the conduction layer. In other words, since only the CuO_2 layer is responsible for superconductivity, it is a superconductor with quasi-two-dimensional properties. But, does superconductivity appear in the extreme case where the number of CuO_2 layers is reduced to one, or where the metal of a conventional superconductor is made into a single atomic-layer? In general, the lower the dimensionality of the system, the greater the effect of fluctuations and the harder it is for phase transitions such as superconductivity to occur, so this question is not obvious.

1.1.2 Two-dimensional superconductivity

The study of two-dimensional superconductors has a long history, dating back to the 1960s [5], and in the 1980s, Goldman et al. reported a superconducting transition in Bi amorphous thin films [6]. This thin film is an amorphous structure containing many defects and disorderly arrangements at the atomic level, but on a larger scale, it can be regarded as a homogeneous film. They fabricated this Bi amorphous film by the quench condensation method. In this method, atoms are deposited on a substrate cooled by liquid helium, which suppresses the diffusion of adsorbed atoms and the formation of large clusters, thus improving the uniformity of the film [7]. In order to avoid structural changes in the film as temperature increases, "in-situ" electron transport measurements were performed while varying the film thickness. Fig.1.1(a) shows the temperature dependence of sheet resistance of the Bi amorphous film. T_c decreases with decreasing film thickness, and after a resistance value of $R_c = h/4e^2 = 6.45k\Omega$, the conductivity changes to an insulator. This superconductor-insulator (S-I) transition is considered to be a quantum phase transition that appears as a result of the introduction of disorder into the two-dimensional system. From the uncertainty principle $\Delta N\ \Delta\theta\ \sim\ 1$ (θ: phase of Cooper pair, N: number of particles), when electrons are localized due to the effect of disorder, the phase fluctuation of the superconducting order parameter increases and a vortex is induced. When the vortex is driven, voltage is induced, and superconductivity is suppressed consequently. Thus, atomic-level defects and irregular structures suppress two-dimensional superconductivity as a disorder.

As described above, as the thickness of the 2D superconductor is reduced, the system undergoes a transition to an insulator. However, since this phase transition is caused by the effect of disorder, it should be possible to realize an atomic-layer superconductor if we can fabricate a two-dimensional thin film with low disorder and high crystallinity such that the sheet resistance of the system is sufficiently smaller than the critical resistance R_c in the S-I transition. This was realized in the 2000s with the development of surface science and ultrahigh vacuum technology.

The first reported superconducting metal thin films with low atomic-level disorder and

high crystallinity were Pb films grown on Si(111)-(7 × 7) surfaces [8]- [10]. By heating the Si(111) substrate to high temperatures (∼ 1200 °C) in an ultrahigh vacuum environment, an atomic-level and clean semiconductor surface can be obtained. Furthermore, Pb is deposited on this surface using the Molecular Beam Epitaxy (MBE) method in an ultra-high vacuum environment to obtain an ideal Pb 2D thin film. Pb and Si do not alloy and form atomically sharp interfaces. The highly crystalline islands grown on these surfaces can be examined in detail using scanning tunneling microscopy (STM) to study the structure and electronic state at the atomic-level. The STM image of Fig.1.1(b) shows that the Pb islands are atomically flat and have a film thickness of 5, 6, and 7 ML [11]. Scanning tunneling spectroscopy (STS) measurements also confirmed a superconducting gap in these Pb islands (Fig.1.1(c)). From the temperature dependence of the superconducting gap,

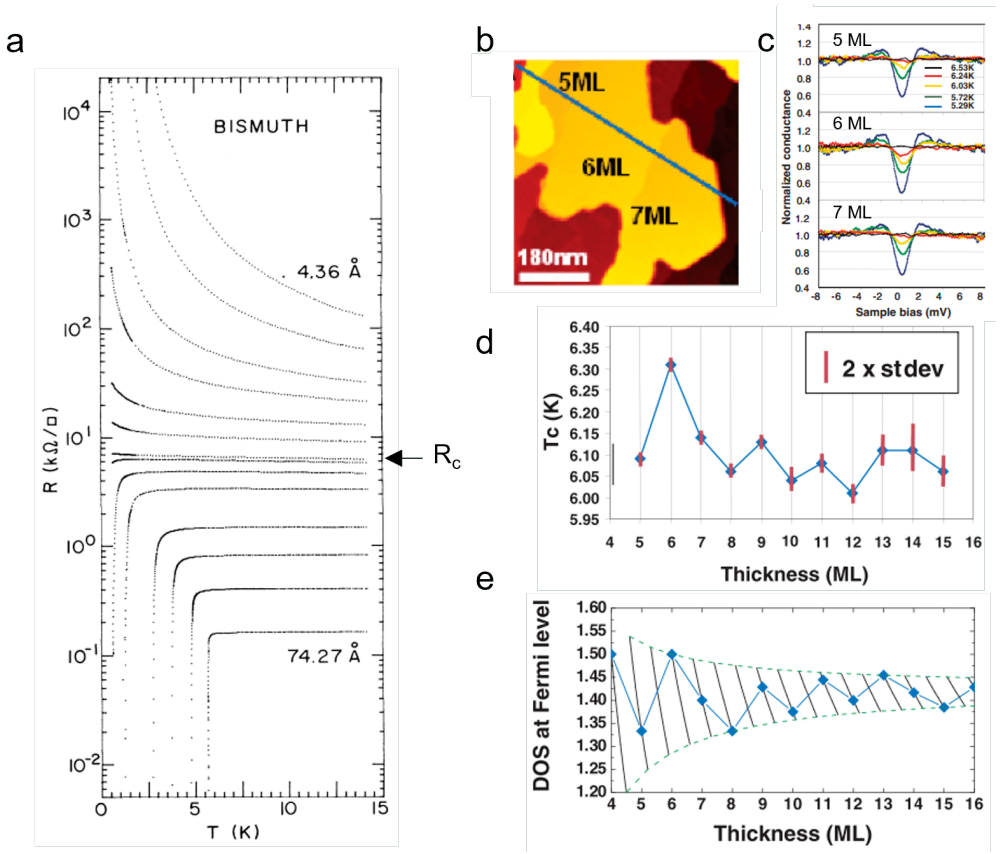

Figure 1.1 (a) Temperature dependence of resistance of Bi amorphous thin films at various thicknesses[6]. (b) STM image of Pb ultrathin film on Si(111) substrate. (c) STS measurement results showing the existence of a superconducting gap in a Pb ultrathin film grown on a Si substrate. (d) Thickness dependence of T_c in Pb ultrathin films estimated by STM and STS measurements. (e) Thickness dependence of density of states in Pb ultrathin films at the Fermi level obtained by STS measurements. (b–e) are taken from [10].

the T_c of the islands of 5ML, 6ML, and 7ML were determined to be 6.09, 6.31, and 6.14 K, respectively; considering that the T_c of Bulk Pb is 7.12 K, it is suggested that the T_c of the islands in atomic-layers holds similar levels and is less disorderly. In other words, the T_c of the highly crystalline metal atomic-layer thin film hardly decreases with decreasing film thickness, indicating that it behaves as an atomic-layer thin film as the ultimate limit of three-dimensional crystals.

In the ideal atomic-layer of Pb thin film superconductors, quantum size effects were observed, reflecting the two-dimensionality. Fig.1.1(d) shows that the T_c of the Pb island oscillates with a period of 2 ML depending on the film thickness. This is a result of the quantization of the electron wavefunction and the formation of a quantum well state due to the [111] crystallographic orientation perpendicular to the plane. When the wavenumber λ(E) of the electron wavefunction in the [111] direction satisfies the following Bohr-Sommerfeld quantization condition, the density of states at that energy takes a maximum value [12].

$$\frac{4\pi d}{\lambda(E)} + \Phi(E) = 2n\pi \tag{1.1}$$

where d is the film thickness, n is an integer representing the quantum number, and Φ(E) is the total phase shift at the interface. Since the wavelength of the electron wavefunction of Pb in the [111] direction of the Fermi level is $\lambda(\mathrm{E_F}) \approx 4$ ML, the film thickness d at which the Fermi level density of states $N(\mathrm{E_F})$ has a maximum value appears every period of $\lambda(\mathrm{E_F})/2 \approx 2$ ML. That is, it is derived that $N(\mathrm{E_F})$ oscillates every 2 ML of film thickness. This phenomenon has been directly observed using STS, as shown in Fig.1.1(e). Comparing Fig.1.1(d) and (e), we can see that the density of states $N(\mathrm{E_F})$ and T_c at the Fermi level oscillate in the same way. This can be understood from the exponential dependence of T_c on $N(\mathrm{E_F})$ in the BCS theory.

In this way, island-shaped atomic-layer thin films are superconductors with unique two-dimensional properties, and their properties can be investigated in detail by STM. On the other hand, since each island has a different phase and T_c, it is difficult to directly relate them to physical properties on a macro scale. Therefore, an atomic-layer thin film with high crystallinity over the entire surface system is desired. Also, the electronic states in the wavenumber space of atomic-layer superconductors can be observed by angle-resolved photoemission spectroscopy (ARPES). While ARPES measurements are surface sensitive, they integrate macroscopic data. Therefore, in order to perform ARPES measurement, an atomic-layer with uniform surface coverage is required as a sample.

1.1.3 Surface superstructure superconductor

Atomic-layer superconductors uniformly covered by a surface have been found in metal surface superstructures on semiconductor surfaces. Dangling bonds are exposed on semiconductor surfaces due to the interrupted periodicity of the crystals. When dangling bonds are exposed, surface reconstruction occurs to lower the surface energy. The most famous system is Si(111)-(7×7) [13]. This structure is a seven-fold change in the periodic structure of the Si(111) unit cell to reduce the total number of dangling bonds. Such a long-period structure appearing on the surface is called a surface superstructure. The deposition of metal atoms on the surface terminates the dangling bonds and stabilizes the system. Depending on the type and amount of metal deposited, various surface superstructures appear, which have been studied intensively in the field of surface science [14, 15]. As the amount of deposited metal atoms increases and the orbitals between adjacent atoms overlap, a band is formed by the surface metal. This surface metal band becomes a two-dimensional electronic state localized on the surface with different features from the bulk.

In 2010, Zhang et al. reported the existence of superconducting gaps in three types of surface superstructures [16]. These surface superstructure superconductors Si(111)-SIC-Pb (SIC-Pb), Si(111)-$\left(\sqrt{7} \times \sqrt{3}\right)$-Pb ($\left(\sqrt{7} \times \sqrt{3}\right)$-Pb), Si(111)-$\left(\sqrt{7} \times \sqrt{3}\right)$-In ($\left(\sqrt{7} \times \sqrt{3}\right)$-In) has the structure shown in Fig.1.2(a-c) and consists of one to two atomic-layers. Atomic images corresponding to these periodic structures have also been observed by STM measurements (Fig.1.2(d-f)). They also estimated T_c from the superconducting gaps obtained by STS measurements (Fig.1.2(g,h), Fig.4.3(a)): T_c for SIC-Pb, $\left(\sqrt{7} \times \sqrt{3}\right)$-Pb, and $\left(\sqrt{7} \times \sqrt{3}\right)$-In were estimated to be 1.83 K, 1.52 K, and 3.18 K, respectively. In particular, $\left(\sqrt{7} \times \sqrt{3}\right)$-In shows almost no change in T_c compared to Bulk In (T_c = 3.4 K), suggesting very little disorder. These experimental facts indicate that the surface superstructure superconductor is the ultimate metal thin film atomic-layer superconductor with the thinnest bulk possible. However, the T_c obtained here is only determined from the locally measured superconducting gap, and it is not obvious whether the Cooper pair forms a coherent superconducting state over a wide area.

As mentioned above, STS measurements measure a local superconducting gap, which only indicates that Cooper pairs are forming locally. On the other hand, a superconducting state is one in which the wavefunction of the Cooper pair is coherent over a long distance. Therefore, to show that the superconducting state is manifested over the entire system, it is essential to observe the zero-resistance by transport measurements. However, because electrode fabrication is generally performed under atmospheric conditions in transport measurements, surface superstructures can easily lose their superconducting properties

due to the breakdown of atomic-layers in the atmosphere. Therefore, it is necessary to fabricate electrodes and perform "in-situ" transport measurements in an ultra-high vacuum environment. This problem was solved by Uchihashi et al. in 2011, and they reported the zero-resistance of $\left(\sqrt{7}\times\sqrt{3}\right)$-In [17]. The results of this study revealed that macroscopic superconducting states can also occur in atomic-layer superconductors. In 2013, zero-resistance was also confirmed in SIC-Pb at $T_c = 1.1$ K from transport

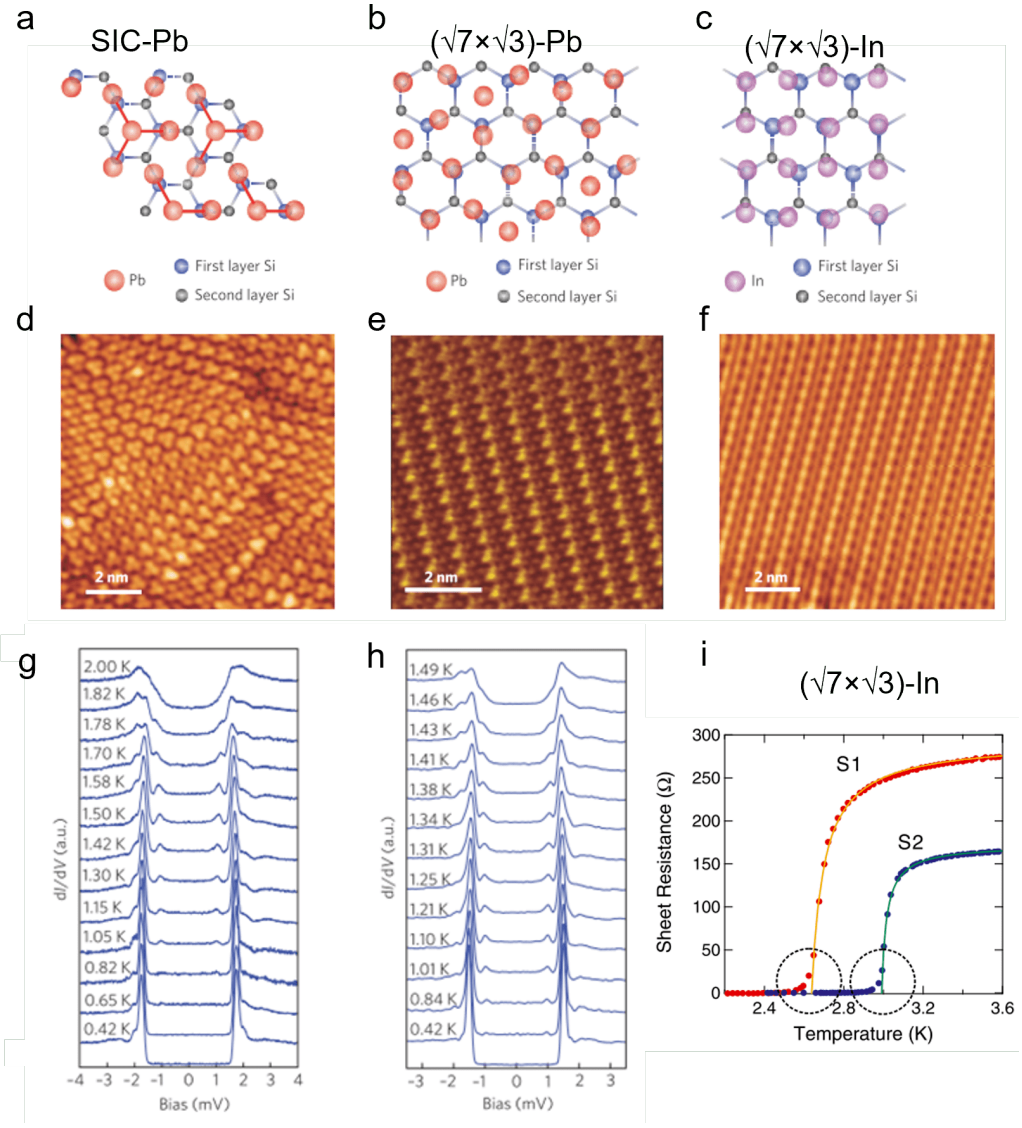

Figure 1.2 (a-c) and (d-f) are schematic diagrams and STM images of atomic structure arrangements of surface superstructure superconductors SIC-Pb, $\left(\sqrt{7}\times\sqrt{3}\right)$-Pb, and $\left(\sqrt{7}\times\sqrt{3}\right)$-In, respectively. The superconducting gaps of SIC-Pb (g) and $\left(\sqrt{7}\times\sqrt{3}\right)$-Pb (h) obtained by STS measurements, respectively. Temperature dependence of the superconducting gap of SIC-Pb. (i) Temperature dependence of sheet resistance of $\left(\sqrt{7}\times\sqrt{3}\right)$-In. (a–h) and (k) are taken from [16] and [19] respectively.

measurements by Yamada et al. They noted that the sheet resistance decreased rapidly in the temperature region of $T > T_c$ near T_c due to thermal fluctuations. Uchihashi et al. also reported that a sharp decrease in the sheet resistance appears at $T > T_c$ and that the sheet resistance decreases with a finite value at $T_c < T$ near T_c (Fig.1.2(i)) [19]. The former is the precursor state of superconductivity and represents amplitude fluctuations of the superconducting order in a two-dimensional system, while the latter represents the effect of phase fluctuations of the superconducting order.

With the recent discovery of various surface atomic-layer superconductors [20]-[22], superconducting phenomena reflecting the properties of the surface atomic-layers themselves have attracted much attention. Surface atomic-layer superconductors have three main features: 1) the superconducting properties are sensitive to the surface/interface, 2) the superconducting properties are completely two-dimensional, and 3) the superconducting properties can be modulated by breaking the inversion symmetry at the surface. Due to the property of 2), the orbital pair-breaking effect is suppressed when a magnetic field is applied in the in-plane direction, and the paramagnetic pair-breaking effect becomes apparent. Also, due to the property 3), atomic-layer superconductors with Rashba splitting due to large spin-orbit interactions have also been reported [23]. In this study, we focus on the surface/interface sensitivity among these properties. By using this property, macroscopic superconducting properties such as T_c can be modulated by depositing other materials. In fact, Yoshizawa et al. reported an increase in T_c by depositing organic molecules [24]. Since this study is directly related to our study, we summarize its details in Chapter 4. In the following, we introduce three studies on two-dimensional superconductivity that have attracted much attention in recent years and are related to surface/interface sensitivities.

1.1.4 Monolayer FeSe on $SrTiO_3$ substrate

Among the studies on surface atomic-layer superconductivity, the study of single-layer FeSe on $SrTiO_3$ substrates has probably attracted the most attention. However, when single-layer FeSe is epitaxially grown on $SrTiO_3$ substrate using MBE method as shown in Fig.1.3(a), the T_c increases abnormally [26]. As we have introduced, even if the superconducting transition occurs in atomic-layer materials, the T_c decreases compared to bulk crystals. In contrast, the T_c of FeSe is increased due to the surface/interface sensitivity derived from atomic-layers. The T_c of single-layer FeSe depends on the type of measurement and experimental environment, and has been measured in the range of 23 - 109 K [27]-[30],[32]. In transport measurements performed under atmospheric conditions, a decrease in resistance began to appear at 40.2 K, and zero resistance was observed at 23.5 K [28]. As shown in Fig.1.3(b), the T_c obtained by micro four-terminal probe transport

measurements in an ultrahigh vacuum environment was anomalously large at 109 K [32].

The most important question here is why single-layer FeSe shows a higher T_c than bulk FeSe. Although various contributions by the substrate are possible, electron doping from the substrate is considered to be the most important role based on the following experimental results [30]. The Fermi surface of bulk FeSe consists of a hole pocket near the Γ point and an electron pocket near the M point in the Brillouin zone, making bulk FeSe a multiband superconductor. This Fermi surface is also observed in three-layer FeSe,

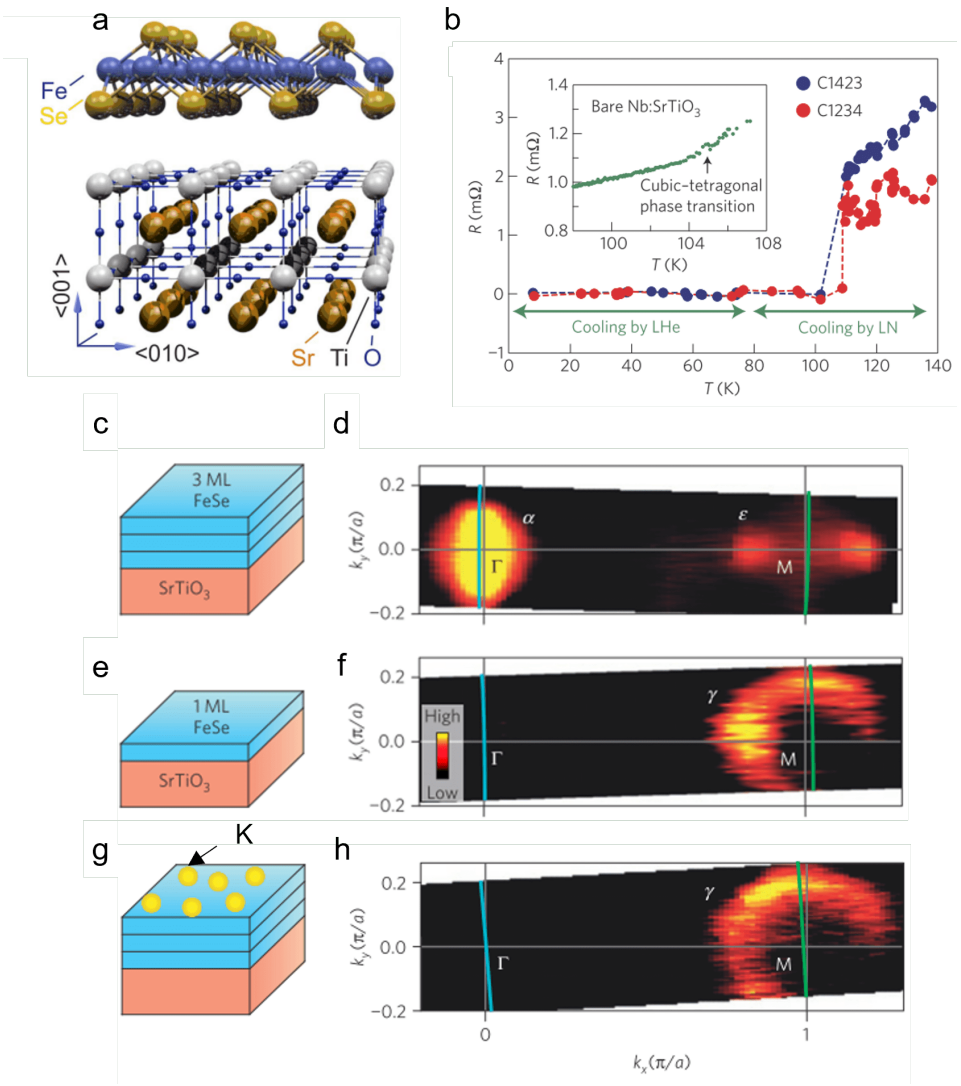

Figure 1.3 (a) Schematic diagrams of atomic structure of monolayer FeSe/$SrTiO_3$(001) [26]. (b) Temperature dependence of sheet resistance of monolayer FeSe [32]. Schematic diagram of 3 ML FeSe (c), 1 ML FeSe (e), and K-doped 3 ML FeSe (g). Fermi surfaces of 3 ML FeSe (d), 1 ML FeSe (f), and K-doped 3 ML FeSe (h) obtained by ARPES measurements. (c-h) are taken from [30].

as shown in Fig.1.3(d). On the other hand, in single-layer FeSe, as shown in Fig.1.3(f), the hole pocket disappears and a larger electron pocket is formed near the M point. This is considered to be electron doping from the $SrTiO_3$ substrate. The fact that this phenomenon is due to electron doping is confirmed by the fact that a similar Fermi surface is obtained when K atoms are deposited on triple-layer FeSe and electron-doped (Fig.1.3(h)). When the optimum amount of electrons was doped into the triple-layer FeSe, $T_c = 48 \pm 3$ K was observed, indicating that the origin of the high T_c is not due to the monolayer nature.

The very high T_c of single-layer FeSe on $SrTiO_3$ substrates is clearly due in large part to the reconstruction of the Fermi surface by electron doping from the substrate. This is a result of carrier doping using the interface sensitivity of surface atomic-layer superconductors, suggesting that carrier doping using surface/interface sensitivity may increase T_c in other materials as well.

1.1.5 Atomic-layer superconductivity induced at the interface of an electric double layer field effect transistor

The control of carriers is important for the development of superconductors with high T_c as described above. A common method for carrier doping that can be adapted to a wider variety of systems is to use a field effect transistor (FET) structure based on an electric double layer. This FET structure can induce a higher carrier density than the usual one because the distance between the positive and negative charges in the electric double layer is about subnanometer, which is smaller than the thickness of the insulating layer, and because an electrolyte with a high relative dielectric constant can be used. By using this technique to induce carriers in $SrTiO_3$, field-induced superconductivity was realized for the first time in a chemically undoped insulator [35].

Although the method described above can be adapted for a variety of insulators, only the study performed by Iwasa et al. is presented here [36]. They employed MoS_2 as the insulating sample. They fabricated a FET structure using a flake-like sample obtained by cleaving MoS_2, as shown in Fig.1.4(a). The dependence of the sheet resistance R_s of the sample on the sample temperature T and the gate voltage V_{LG} of the ionic liquid is shown in Fig.1.4(b). For $V_{LG} <$ V, an insulating conduction characteristic is exhibited where the sheet resistance R_s increases as the temperature decreases. On the other hand, for gate voltages of 1 V $\leq V_{LG} <$ 4 V, a metallic conduction characteristic is observed. In the $4 \leq V_{LG}$ region, a sharp decrease in the sheet resistance is observed at low temperatures, indicating a superconducting transition. Fig.1.4(c) shows that the highest value, $T_c = 10.8$ K, is about 40 % higher than the T_c obtained by chemical doping. The temperature dependence of the in-plane critical magnetic field indicates that the two-

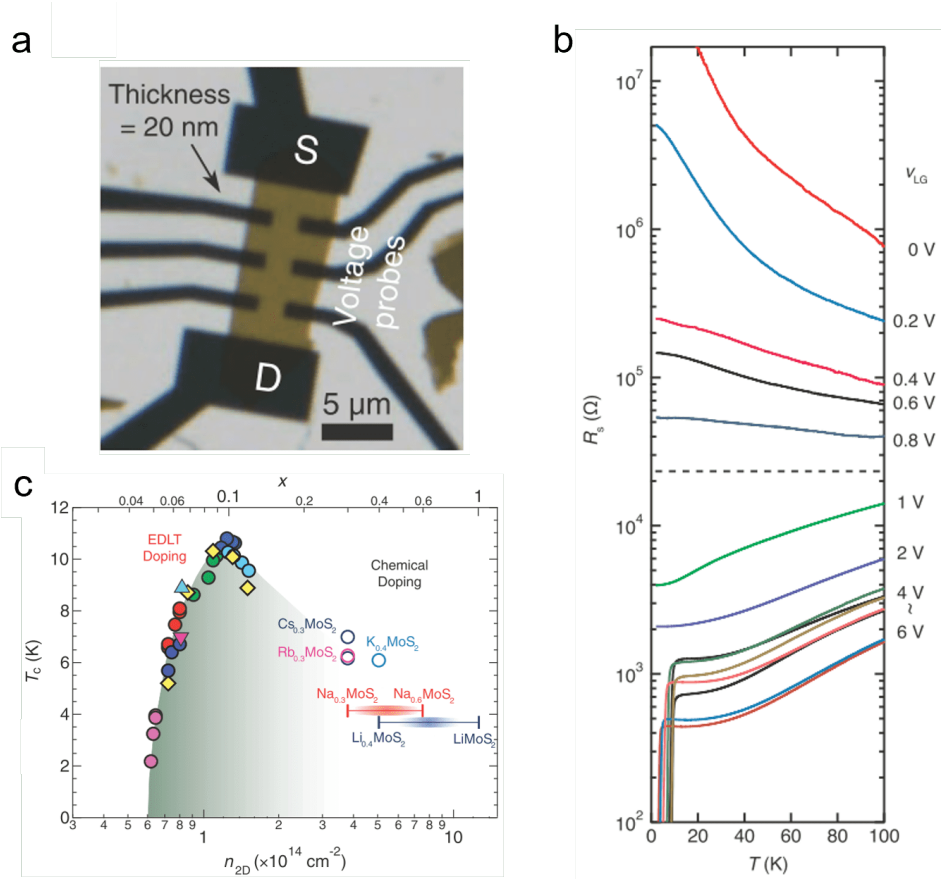

Figure 1.4 (a) Optical micrograph of MoS_2 FET device used for superconductivity measurements. (b) Temperature dependence of resistance of MoS_2 electrical double layer FET modulated by the gate voltage. (c) Dependence of superconducting transition temperature T_c of both electrostatically and chemically doped MoS_2 on carrier density n_{2D}. Fig.1.4 are taken from [36].

dimensional electron system induced in MoS_2 is concentrated in 2-3 atomic layers near the interface.

1.1.6 Intercalated bilayer graphene

To correlate surface atomic-layer superconductivity with carrier doping, it is preferable to use surface scientific methods. For example, the local structure and superconducting properties can be obtained by STM, and the band dispersion can be obtained by ARPES, allowing a comparison between the two. The superconducting transition phenomenon in chemically doped bilayer graphene has been studied by surface science methods, and the origin of the superconducting transition has been elucidated. The studies on bilayer graphene are introduced below.

Ichinokura et al. prepared bilayer graphene by heating a SiC(0001) substrate at 1550

°C. They deposited Ca and Li onto this bilayer graphene in an ultrahigh vacuum environment and performed "in-situ" transport measurements. Metals deposited on graphene can intercalate between graphene layers (intercalation), resulting in the structure shown in Fig.1.5(a). Such materials are called intercalated bilayer graphene. The temperature dependence of the sheet resistance of C_6CaC_6 and C_6LiC_6 shows that only C_6CaC_6 undergoes a superconducting transition at $T_c = 2$ K (Fig.1.5(b)).

The reason why superconductivity did not develop in C_6LiC_6 was explained as follows. Fig.1.5(c) shows the band dispersion of C_6CaC_6 and C_6LiC_6 [41]. In C_6CaC_6, the free electron-like intercalation bands produced by the interlayer interactions cross the Fermi level, forming a Fermi surface. On the other hand, in C_6LiC_6, no intercalation bands are

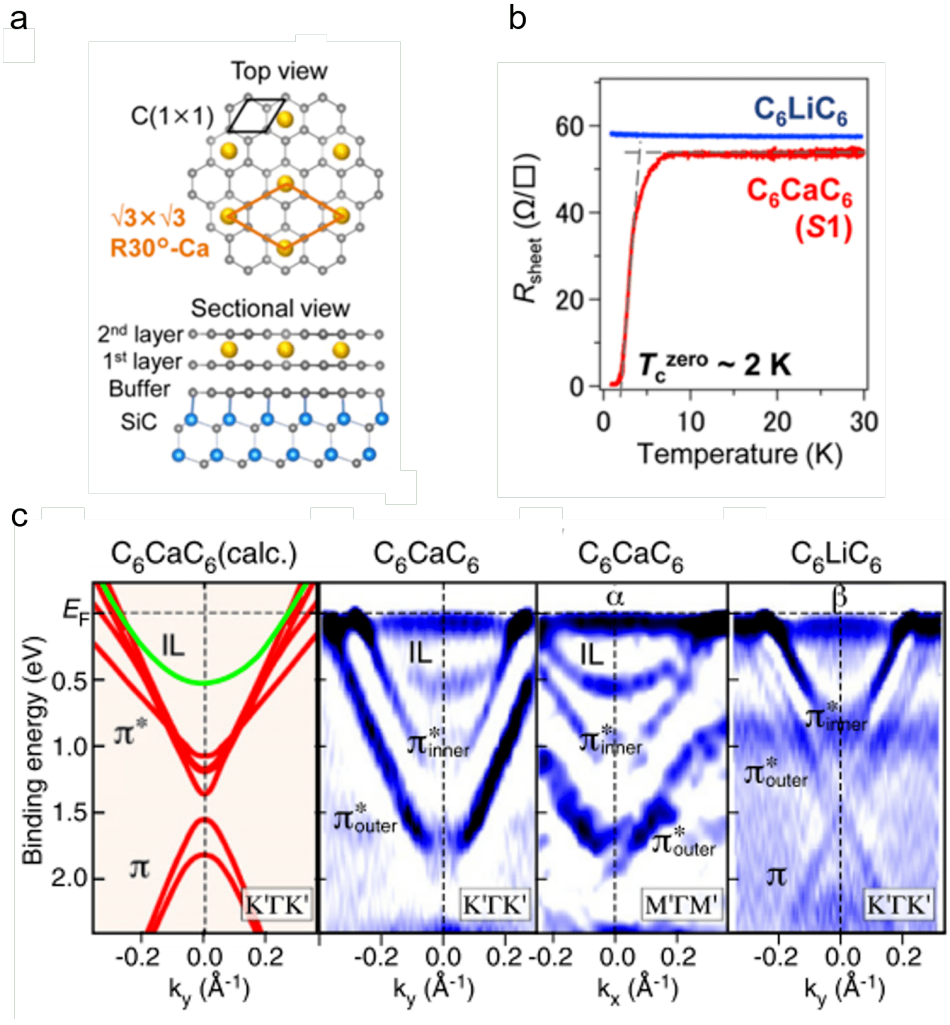

Figure 1.5 (a) Top and sectional views of the crystal structure of C_6CaC_6 on SiC. (b) Temperature dependences of sheet resistance of C_6CaC_6 and C_6LiC_6. (c) Band dispersions at the K point of C_6CaC_6 and C_6LiC_6 obtained by ARPES and *ab initio* calculation [41]. (a,b) are taken from [40].

observed at the Fermi level, which is theoretically predicted to be located at higher energy than the Fermi level [42]. Intercalation bands have been pointed out to have an important role in the occurrence of superconductivity in graphene interlayers.

By correlating the band structure obtained by ARPES with the superconducting properties obtained by transport as described above, the mechanism of superconductivity appearance is being elucidated. Thus, it is possible to clarify the correlation between carrier doping and the superconducting properties of atomic-layer superconductors through a comprehensive study using surface science experimental techniques.

1.2 Research objectives

As introduced so far, ultra-high vacuum technology and surface science have greatly contributed to research on atomic-layer superconductors. In recent years, various systems of atomic-layer superconductors have been discovered, and research on special superconducting states derived from atomic-layers has attracted attention. The three recent research results mentioned above show that atomic-layer superconductivity can be an effective platform for both "new material production" and "T_c increase". In atomic-layer superconductors, the influence of the surface interface extends to the entire system. This is an advantageous feature for artificially modulating the superconducting properties. In this study, we aimed to modulate the superconducting properties of surface atomic-layer superconductors by organic molecule adsorption and to elucidate the mechanism. In general, organic molecules exert only weak interactions such as van der Waals forces with surfaces and do not destroy atomic-layer materials. Therefore, this method is expected to be applicable to various surface atomic-layer superconductors. Since organic molecules have a high degree of freedom in fabrication, clarifying the effects of organic molecules on atomic-layer superconducting properties will make it possible to create more compatible combinations. Based on the above background, in this research, we aim to clarify the effects of carrier doping with organic molecules on surface atomic-layer superconductors and the effects of adsorption structures of organic molecules on surface atomic-layer superconductors. The target samples are "ZnPc adsorbed Si(111)-$\left(\sqrt{7}\times\sqrt{3}\right)$-In" and "PTCDA adsorbed Si(111)-$\left(\sqrt{7}\times\sqrt{3}\right)$-In". The reason why we chose Si(111)-$\left(\sqrt{7}\times\sqrt{3}\right)$-In as the surface atomic-layer superconductor is that it does not have a complicated chemical composition and its structure is well understood both experimentally and theoretically. This is because the interpretation of experimental results is easy.

In this study, the following methods were used for research.
We investigated the adsorption structure of organic molecular thin films on $\left(\sqrt{7}\times\sqrt{3}\right)$-In using STM. Using ARPES, we estimated the electronic state change and carrier doping of $\left(\sqrt{7}\times\sqrt{3}\right)$-In by organic molecular adsorption. From *ab initio* calculations, the amount of

carrier doping by the adsorbed organic molecules and the spin magnetic moment possessed by the organic molecules were obtained. In addition, we also calculated the density of states of $\left(\sqrt{7} \times \sqrt{3}\right)$-In. Finally, transport measurements were taken to measure T_c that changed due to organic molecular adsorption, and by clarifying the correlation with experimental results obtained by other methods, the effects of organic molecular adsorption on T_c were comprehensively investigated.

This research was conducted in collaboration with the Sakamoto Laboratory of Osaka University and the Minamitani Laboratory of Osaka University. The Sakamoto laboratory provided the ARPES measurement results, and the Minamitani laboratory provided *ab initio* calculations results for ZnPc and CuPc on $\left(\sqrt{7} \times \sqrt{3}\right)$-In. In addition, the author performed sample preparations, LEED measurements, STM measurements, transport measurements, and *ab initio* calculations of the density of state of $\left(\sqrt{7} \times \sqrt{3}\right)$-In at Uchihashi Laboratory.

1.3 Outline of the dissertation

In Chapter 2, we introduce the derivation of theories and equations necessary for the analysis and interpretation of the experimental results obtained in this study, citing several references. Chapter 3 describes the methods and principles used in the experiments and analyses. We also introduce the experimental equipment used. Chapter 4 introduces the basic physical properties and superconducting properties of $\left(\sqrt{7} \times \sqrt{3}\right)$-In. In addition, we will introduce previous studies directly related to this study and clarify the unresolved problem of the effect of organic molecule adsorption on T_c. Next, the results of this study are shown and discussed through comparison with previous studies. In Chapter 5, after introducing previous studies on PTCDA, we present and discuss the results of this study. Chapter 6 compares the results of the above two studies and presents the overall conclusion.

References

[1] J.G. Bednorz and K.A. Müler, Zeitschrift für Physik B CondensedMatter **64**, 189-193 (1986).

[2] P. H. Hor, R. L. Meng, L. Gao, Z. J. Huang, Y. Q. Wang, and C. W. Chu, Phys. Rev. Lett. **58**, 908-910 (1987).

[3] Yoichi Kamihara , Takumi Watanabe, Masahiro Hirano, and Hideo Hosono, J. AM. CHEM. SOC. **130**, 3296-3297 (2008).

[4] Maddury Somayazulu, Muhtar Ahart, Ajay K. Mishra, Zachary M. Geballe, Maria Baldini,Yue Meng, Viktor V. Struzhkin, and Russell J. Hemley, Phys. Rev. Lett. **122**, 027001 (2019).

[5] V. L. GINZBURG, Physics Letters **13**, 101-102 (1964).

[6] D. B. Haviland, Y. Liu, and A. M. Goldman, Phys. Rev. Lett. **62**, 2181-2183 (1989).

[7] Myron Strongin, R. S. Thompson, O. F. Kammerer, and J. E. Crow, Phys. Rev. B **1**, 1078-1091 (1970).

[8] Yang Guo, Yan-Feng Zhang, Xin-Yu Bao, Tie-Zhu Han, Zhe Tang, Li-Xin Zhang, Wen-Guang Zhu, E. G. Wang, Qian Niu, Z. Q. Qiu, Jin-Feng Jia, Zhong-Xian Zhao, Qi-Kun Xue, Science **30**, 1915-1917 (2004).

[9] Mustafa M. özer, James R. Thompson and Hanno H. Weitering, Nat. Phys. **2**, 173-176 (2006).

[10] Daejin Eom, S. Qin, M.-Y. Chou, and C. K. Shih, Phys. Rev. Lett. **96**, 027005 (2006).

[11] Dimitri Roditchev, Christophe Brun, Lise Serrier-Garcia, Juan Carlos Cuevas, Vagner Henrique Loiola Bessa, Milorad Vlado MiloŠević, Françoís Debontridder, Vasily Stolyarov and Tristan Cren, Nat. Phys. 11, 332-337 (2015).

[12] J. J. Paggel, T. Miller, and T.-C. ChiangAuthors Info and Affiliations, Science **283**, 1709-1711 (1999).

[13] R. E. SCHLIER AND H. E. FARNSWORTH, J. Chem. Phys. **30**, 917 (1959).

[14] J. Kraft, M. G. Ramsey, and F. P. Netzer, Phys. Rev. B **55**, 5384-5393 (1997).

[15] Takashi Uchihashi and Urs Ramsperge, Appl. Phys. Lett. **80**, 4169-4171 (2002).

[16] Tong Zhang, Peng Cheng, Wen-Juan Li, Yu-Jie Sun, Guang Wang, Xie-Gang Zhu, Ke He, Lili Wang, Xucun Ma, Xi Chen, Yayu Wang, Ying Liu, Hai-Qing Lin, Jin-Feng Jia and Qi-Kun Xue, Nat. Phys. **6**, 104-108 (2010).

[17] Takashi Uchihashi, Puneet Mishra, Masakazu Aono, and Tomonobu Nakayama, Phys.

Rev. Lett. **107**, 207001 (2011).

[18] Manabu Yamada, Toru Hirahara, and Shuji Hasegawa, Phys. Rev. Lett. **110**, 237001 (2013).

[19] Takashi Uchihashi, Puneet Mishra and Tomonobu Nakayama, Nanoscale Res. Lett. **8**, 167 (2013).

[20] Takayuki Sekihara, Ryuichi Masutomi, and Tohru Okamoto, Phys. Rev. Lett. **111**, 057005 (2013).

[21] A. V. Matetskiy, S. Ichinokura, L. V. Bondarenko, A. Y. Tupchaya, D. V. Gruznev, A. V. Zotov, A. A. Saranin, R. Hobara, A. Takayama, and S. Hasegawa, Phys. Rev. Lett. **115**, 147003 (2015).

[22] Fumikazu Oguro, Yudai Sato, Kanta Asakawa, Masahiro Haze, and Yukio Hasegawa, Phys. Rev. B **103**, 085416 (2021).

[23] Shunsuke Yoshizawa, Takahiro Kobayashi, Yoshitaka Nakata, Koichiro Yaji, Kenta Yokota, Fumio Komori, Shik Shin, Kazuyuki Sakamoto and Takashi Uchihashi, Nat. Commun. **12**, 1462 (2021).

[24] Shunsuke Yoshizawa, Emi Minamitani, Saranyan Vijayaraghavan, Puneet Mishra, Yasumasa Takagi, Toshihiko Yokoyama, Hiroaki Oba, Jun Nitta, Kazuyuki Sakamoto, Satoshi Watanabe, Tomonobu Nakayama, and Takashi Uchihashi, Nano Lett. **17**, 2287-2293 (2017).

[25] S. Medvedev, T. M. McQueen, I. A. Troyan, T. Palasyuk, M. I. Eremets, R. J. Cava, S. Naghavi, F. Casper, V. Ksenofontov, G. Wortmann and C. Felser, Nat. Mater. **8**, 630-633 (2009).

[26] Lili Wang, Xucun Ma and Qi-Kun Xue, Supercond. Sci. Technol. **29**, 123001 (2016).

[27] Wenhao Zhang, Zhi Li, Fangsen Li, Huimin Zhang, Junping Peng, Chenjia Tang, Qingyan Wang, Ke He, Xi Chen, Lili Wang, Xucun Ma, and Qi-Kun Xue, Phys. Rev. B **89**, 060506 (2014).

[28] W.-H. Zhang, Y. Sun, J.-S. Zhang, F.-S. Li, M.-H. Guo, Y.-F. Zhao, H.-M. Zhang, J.-P. Peng, Y. Xing, H.-C. Wang, T. Fujita, A. Hirata, Z. Li, H. Ding, C.-J. Tang, M. Wang, Q.-Y. Wang, K. He, S.-H. Ji, X. Chen, J.-F. Wang, Z.-C. Xia, L. Li, Y.-Y. Wang, J. Wang, L.-L. Wang, M.-W. Chen, Q.-K. Xue, and X.-C. Ma, Chin. Phys. Lett. **31**, 017401 (2014).

[29] Yi Sun, Wenhao Zhang, Ying Xing, Fangsen Li, Yanfei Zhao, Zhengcai Xia, Lili Wang, Xucun Ma, Qi-Kun Xue and Jian Wang, Sci. Rep. **4**, 6040 (2014).

[30] Y. Miyata, K. Nakayama, K. Sugawara, T. Sato and T. Takahashi, Nat. Mater. **14**, 775-779 (2015).

[31] Manabu Yamada, Toru Hirahara, Rei Hobara, Shuji Hasegawa, Hiroyuki Mizuno, Yutaka Miyatake, Toshihiko Nagamura, e-J. Surf. Sci. Nanotech. **10**, 400-405 (2012).

[32] Jian-Feng Ge, Zhi-Long Liu, Canhua Liu, Chun-Lei Gao, Dong Qian, Qi-Kun Xue, Ying Liu and Jin-Feng Jia, Nat. Mater. **14**, 285-289 (2015).

[33] Can-Li Song, Yi-Lin Wang, Ye-Ping Jiang, Zhi Li, Lili Wang, Ke He, Xi Chen, Xu-Cun Ma and Qi-Kun Xue, Phys. Rev. B **84**, 020503 (2011).

[34] Can-Li Song, Hui-Min Zhang, Yong Zhong, Xiao-Peng Hu, Shuai-Hua Ji, Lili Wang, Ke He, Xu-Cun Ma, and Qi-Kun Xue, Phys. Rev. Lett. **116**, 157001 (2016).

[35] K. Ueno, S. Nakamura, H. Shimotani, A. Ohtomo, N. Kimura, T. Nojima, H. Aoki, Y. Iwasa and M. Kawasaki, Nat. Mater. **7**, 855-858 (2008).

[36] J. T. Ye, Y. J. Zhang, R. Akashi, M. S. Bahramy, R. Arita, Y. Iwasa, Science **338**, 1193-1196 (2012).

[37] K. S. Novoselov, A. K. Geim, S. V. Morozov, D. Jiang, M. I. Katsnelson, I. V. Grigorieva, S. V. Dubonos and A. A. Firsov, Nature **438**, 197-200 (2005).

[38] K. S. Novoselov, Z. Jiang, Y. Zhang, S. V. Morozov, H. L. Stormer, U. Zeitler, J. C. Maan, G. S. Boebinger, P. Kim, and A. K. Geim, Science **315**, 1379 (2007).

[39] Changgu Lee, Xiaoding Wei, Jeffrey W. Kysar and James Hone, Science **321**, 385-388 (2008).

[40] Satoru Ichinokura, Katsuaki Sugawara, Akari Takayama, Takashi Takahashi and Shuji Hasegawa, ACS Nano **10**, 2761 − 2765 (2016). https://pubs.acs.org/doi/10.1021/acsnano.5b07848

[41] Kohei Kanetani, Katsuaki Sugawarab, Takafumi Sato, Ryota Shimizu, Katsuya Iwaya , Taro Hitosugi and Takashi Takahashi, Proc. Natl. Acad. Sci. **109**, 19610- 19613 (2012).

[42] M. Calandra, C. Attaccalite, G. Profeta, and F. Mauri, Phys. Rev. Lett. **108**, 149701 (2012).

Chapter 2 Fundamentals

2.1 BCS theory

In this section, we introduce the Bardeen-Cooper-Schrieffer (BCS) theory, which is the standard theory for superconductivity in metals.

The ground state of a metal in the normal conduction state is a state in which all energy states below the Fermi energy E_F are occupied (Fermi sea). Consider a pair of electrons interacting via a two-body attraction potential on a filled Fermi surface; the influence of electrons other than the one-electron pair is assumed to be incorporated only through Pauli's principle. At the lowest energy state of the electron pair, the total momentum is expected to be zero, so the wavefunction is

$$\Psi(\mathbf{r}_1, \mathbf{r}_2) = \sum_k g(\mathbf{k}) e^{i\mathbf{k}\mathbf{r}_1} e^{-i\mathbf{k}\mathbf{r}_2} \tag{2.1}$$

where $g(\mathbf{k})$ is the probability amplitude of finding a two-electron in state $\mathbf{k}$,$-\mathbf{k}$. The two-body wave function of the Fermi particle must be antisymmetric with respect to the coordinate exchange of the particles. That is, this two-body wavefunction must be antisymmetric with respect to either the pair wavefunction or the spin wavefunction, which describes the relative motion between the electrons. Since the electron-electron interaction is an attractive one, the closer the two electrons are, the smaller the energy should be. Therefore, the two-body wave function should be in a spin-singlet state with zero center-of-gravity motion of the electron pairs.

Substituting Eq.2.1 into the Schrödinger equation with the interaction potential between two electrons as $V(\mathbf{r})$, the energy eigenvalue E can be expressed by the following equation.

$$g(\mathbf{k})(E - 2\epsilon(k)) = \sum_{k'} V(\mathbf{k}.\mathbf{k}') g(\mathbf{k}') \tag{2.2}$$

where $V(\mathbf{k}, \mathbf{k}')$ is the Fourier component of $V(\mathbf{r})$ and $\epsilon(k) = \hbar^2 k^2 / 2m$. The gravitational potential in BCS theory is an interaction through phonons. Therefore, no more energy can be exchanged than the energy $\hbar\omega_D$ ($\hbar\omega_D$: Debye frequency) of the phonon with the highest energy in the solid. Therefore, the range of momentum that the electron can take is specified as follows.

$$E_F - \hbar\omega_D < \epsilon_k < E_F + \hbar\omega_D \tag{2.3}$$

In general, since $\hbar\omega_D << E_F$ in metals, the range of possible energies for electrons is very narrow. Also, assuming that the attractive interaction is isotropic

$$V_{\mathbf{kk}'} = \begin{cases} -V & (E_F - \hbar\omega_D < \epsilon_k < E_F + \hbar\omega_D) \\ 0 & (otherwise) \end{cases} \tag{2.4}$$

In this case, the right-hand side of Eq.2.2 is constant regardless of $\mathbf{k}$, therefore

$$g(\mathbf{k}) = V\frac{\sum_{k'} g(\mathbf{k}')}{2\epsilon(k) - E} \tag{2.5}$$

Summing over k on both sides and dividing by $\sum g(\mathbf{k})$

$$\frac{1}{V} = \sum_k \frac{1}{2\epsilon(k) - E)} \tag{2.6}$$

Using the density of states $N(E_F)$ at the Fermi level and replacing the sum of states with the energy integral

$$\frac{1}{V} = \int_{E_F}^{E_F + \hbar\omega_D} d\epsilon \frac{N(\epsilon - E_F)}{2\epsilon(k) - E)} = \frac{1}{2}N(E_F)\ln\frac{2E_F - E + 2\hbar\omega_D}{2E_F - E} \tag{2.7}$$

Since $N(E_F) << 1$ for most general superconductivity, we transform Eq.2.7 using the weak coupling approximation.

$$E \sim E_F - 2\hbar\omega_D \exp\left(-\frac{2}{N(E_F)V}\right) \tag{2.8}$$

From Eq.2.8 we can see that: the energy of the electron pair with $\mathbf{k} > \mathbf{k}_F$ is lower than that of the E_F. This means that it is energetically more beneficial for the two electrons to form a bound state. Also, no matter how small the attractive interaction is, the energy of the two-electron pair on the Fermi surface is always lower than the group of electrons occupying the Fermi surface and below. Therefore, the Fermi sea corresponding to the ground state of the normal-conducting metal becomes unstable and must change to another ground state.

In BCS theory, Cooper pairs are spin-singlet electron pairs with zero center-of-momentum and the attractive interaction between electrons is assumed to be isotropic. The previous discussion has shown that when Cooper pairs are formed due to the attractive interaction between electrons, the formation of a new ground state is required. In this new ground state (BCS ground state), electrons below the E_F are redistributed above the E_F. Only the scattering process via phonons such that the momentum vector of the Cooper pair changes from $(\mathbf{k}\uparrow, -\mathbf{k}\downarrow) \rightarrow (\mathbf{k}'\uparrow, -\mathbf{k}'\downarrow)$ is taken out and under the assumption of the Cooper pair in the BCS theory the Hamiltonian of the BCS ground state can be described as follows.

$$H = \sum_{k,\sigma} \xi(\mathbf{k}) c^\dagger_{k\sigma} c_{k\sigma} + \sum_{k,k'} V(\mathbf{k},\mathbf{k}') c^\dagger_{-k'\downarrow} c^\dagger_{k'\uparrow} c_{k'\uparrow} c_{-k'\downarrow} \tag{2.9}$$

where $c^\dagger(c)$ is the electron creation (annihilation) operator, $\xi(\mathbf{k})$ is the electron energy measured from the chemical potential, and $V(\mathbf{k}.\mathbf{k}')$ is the attractive interaction required to create Cooper pairs. This Hamiltonian is called BCS reduced Hamiltonian. However, since it is difficult to treat the interaction term of the Hamiltonian as it is, a mean-field approximation is performed. We introduce $< c^\dagger_{k\uparrow} c^\dagger_{-k\downarrow} >$ as the mean field.

$$c^\dagger_{k\uparrow} c^\dagger_{-k\downarrow} = \left\langle c^\dagger_{k\uparrow} c^\dagger_{-k\downarrow} \right\rangle + \left(c^\dagger_{k\uparrow} c^\dagger_{-k\downarrow} - \left\langle c^\dagger_{k\uparrow} c^\dagger_{-k\downarrow} \right\rangle \right) \tag{2.10}$$

$$c_{-k\downarrow} c_{k\uparrow} = \langle c_{-k\downarrow} c_{k\uparrow} \rangle + \left(c_{-k\downarrow} c_{k\uparrow} - \langle c_{-k\downarrow} c_{k\uparrow} \rangle \right) \tag{2.11}$$

Also, using this mean field, the gap function $\Delta(\mathbf{k})$ is defined as follows.

$$\Delta(\mathbf{k}) \equiv -\sum_{k'} V(\mathbf{k}, \mathbf{k}') \langle c_{-k'\downarrow} c_{k'\uparrow} \rangle \tag{2.12}$$

$$\Delta^*(\mathbf{k}) \equiv -\sum_{k'} V(\mathbf{k}, \mathbf{k}') \left\langle c^\dagger_{k\uparrow} c^\dagger_{-k\downarrow} \right\rangle \tag{2.13}$$

Substituting equations 2.10 - 2.13 into Eq.2.9, the mean-field approximation Hamiltonian is as follows.

$$H_{MF} = \sum_{k\sigma} \xi(\mathbf{k}) c^\dagger_{k\sigma} c_{k\sigma} - \sum_k \left(\Delta(\mathbf{k}) c^\dagger_{k\uparrow} c^\dagger_{-k\downarrow} + \Delta^*(\mathbf{k}) \left\langle c^\dagger_{k\uparrow} c^\dagger_{-k\downarrow} \right\rangle \right) \tag{2.14}$$

Equation 2.14 can be diagonalized using the following Bogoliubov transformation.

$$b_{k\uparrow} = u_k c_{k\uparrow} - v_k c^\dagger_{-k\downarrow} \tag{2.15}$$

$$b^\dagger_{-k\downarrow} = u^*_k c^\dagger_{-k\downarrow} + v^*_k c_{k\uparrow} \tag{2.16}$$

The newly introduced particles (elementary excitations) described by $b^\dagger, b$ are called quasi-particles because they are different from the electrons described by the usual creation and annihilation operators acting on the vacuum state. Since quasiparticles are also fermions, an anticommutation relation is required. As a result, the coefficients should have the following relationships:

$$|u_k|^2 + |v_k|^2 = 1 \tag{2.17}$$

Also, rewrite Eq.2.14 using equations 2.15 and 2.16. Then the condition for the off-diagonal term to be 0 is

$$2\xi(\mathbf{k}) u_k v^*_k - \Delta(\mathbf{k}) v^{*2}_k + \Delta(\mathbf{k})^* u^2_k = 0 \tag{2.18}$$

From equations 2.17 and 2.18

$$|u_k|^2 = \frac{1}{2}\left[1 + \frac{\xi(\mathbf{k})}{E(\mathbf{k})}\right], \quad |v_k|^2 = \frac{1}{2}\left[1 - \frac{\xi(\mathbf{k})}{E(\mathbf{k})}\right] \tag{2.19}$$

$$E(\mathbf{k}) = \sqrt{\xi^2(\mathbf{k}) + |\Delta(\mathbf{k})|^2} \tag{2.20}$$

$\Delta(\mathbf{k})$ corresponds to the energy of an unpaired electron excited to the state designated by $\mathbf{k}$. In particular, considering an electron lying on the Fermi surface ($\xi(\mathbf{k}=0)$, it is excited with infinitesimal energy in the normal state, whereas in the BCS ground state, an energy of at least $|\Delta(\mathbf{k})|$ is required for excitation. When Eq.2.18 holds, the Hamiltonian is diagonalized and reduced to the following form, where W_S is the ground state energy.

$$H_{MF} = W_S + \sum_k E(\mathbf{k}) \left(b^\dagger_{k\uparrow} b_{k\uparrow} + b^\dagger_{-k\downarrow} b_{-k\downarrow} \right) \tag{2.21}$$

If $b^\dagger_{k\uparrow} b_{k\uparrow}$ and $b^\dagger_{-k\downarrow} b_{-k\downarrow}$ in the second term on the right side of Eq.2.21 are interpreted as the number density operators of quasiparticles with upward spin and downward spin, is isomorphic to the free-particle Hamiltonian. In other words, within the mean-field approximation, the quasiparticles excited from the BCS ground state can be regarded as forming a free Fermi particle system with the energy given by Eq.2.20.

Since quasiparticles are in a free Fermi system, the statistical mean of the number of quasiparticles with excitation energy $E(\mathbf{k})$ follows the Fermi-Dirac function $f(E(\mathbf{k}))$.

$$\left\langle b^\dagger_{k\uparrow} b_{k\uparrow} \right\rangle = \left\langle b^\dagger_{-k\downarrow} b_{-k\downarrow} \right\rangle = f(E(\mathbf{k})) \tag{2.22}$$

With $\beta = 1/k_B T$, substituting equations 2.15, 2.16, and 2.22into Eq.2.12 yields the following equations.

$$\Delta(\mathbf{k}) = -\sum_{k'} V(\mathbf{k}, \mathbf{k}') \frac{\Delta(\mathbf{k}')}{2E} \tanh \left[\frac{1}{2} \beta E(\mathbf{k}') \right] \tag{2.23}$$

This is the general gap equation extended to finite temperatures. Under the assumption of the BCS theory, the attractive interaction is isotropic, so we can set $V(\mathbf{k}, \mathbf{k}') = -V$. Therefore, $\Delta(\mathbf{k})$ on the left side also becomes isotropic and does not depend on $\mathbf{k}$. First, both sides of Eq.2.23 are divided by Δ. Next, the transition temperature T_c can be defined as the temperature at which $\Delta(T) \to 0$ when $T \to T_c$, and considering that $E(\mathbf{k}') \to |\xi(\mathbf{k}')|$.

$$1 \simeq -V \sum_{k'} \frac{1}{2E} \tanh \left[\frac{\xi(\mathbf{k}')}{2k_B T_c} \right] \simeq V N(E_F) \int_{-\omega_D}^{\omega_D} d\xi \frac{1}{2E} \tanh \left[\frac{\xi(\mathbf{k}')}{2k_B T_c} \right] \tag{2.24}$$

Also, considering that $k_B T_c << \hbar\omega_D$ for ordinary metals, the following equation is obtained.

$$k_B T_c = 1.13 \hbar\omega_D \exp \left(-\frac{1}{N(E_F) V} \right) \tag{2.25}$$

From Eq.2.25, it can be seen that the transition temperature T_c depends on the attractive interaction V and the density of states $N(E_F)$ at the Fermi level. In other words, in order to increase the T_c of a superconductor, it is necessary to increase the attractive interaction V and the density of states $N(E_F)$ at the Fermi level. This is very important in considering this research.

Also, from Eq.2.23, $\Delta(T=0)$ at absolute zero is obtained as follows.

$$\Delta(0) = 2\hbar\omega_D \exp\left(-\frac{1}{N(E_F)V}\right) \tag{2.26}$$

Comparing equations 2.25 and 2.26,

$$\frac{\Delta(0)}{k_B T_c} = 1.76 \tag{2.27}$$

Equation 2.27 is a material-independent universal constant within the BCS theory. Furthermore, since $E(\mathbf{k})$ in the superconducting state has a one-to-one relationship with $\xi(\mathbf{k})$ in the normal state, the superconducting density of states $N_s(E)$ is expressed by the following equation.

$$N_s(E)dE = N_n(\xi)d\xi \tag{2.28}$$

Therefore, from equations 2.20 and 2.28,

$$\frac{N_s(E)}{N_n(E_F)} = \begin{cases} 0 & (|E| < \Delta) \\ \frac{|E|}{\sqrt{E^2-\Delta^2}} & (|E| > \Delta) \end{cases} \tag{2.29}$$

The constant $N_n(\xi) = N_n(E_F)$ is set because only the vicinity of the Fermi level is focused. This result also indicates that an energy gap of 2Δ opens near E_F. In the normal state, the state in the gap moves to $E = E_F \pm \Delta$, and a density of states peak appears. This is called a coherence peak.

2.2 Fundamentals of two-dimensional superconductivity

In layered materials and thin films, the thickness of the superconducting electronic system may be thinner than the GL coherence length $\xi_{GL}(0)$. Such superconductivity can be regarded as a two-dimensional superconductor with a degree of freedom only in the two-dimensional plane direction because the macroscopic wave function Ψ cannot change in the thickness direction. Two-dimensional superconductors transform into insulators when disturbances are introduced into the system. In general, Anderson's theorem states that superconductivity is not significantly affected by perturbations unless the time-reversal symmetry is violated. However, this theorem does not consider the effects of Anderson localization and superconducting phase fluctuations due to disturbances. Therefore, in two-dimensional systems, these effects become important, making superconductivity vulnerable to perturbations.

When the whole d-dimensional system is in the normal state, the energy required to generate a pair of Cooper pairs is the superconducting condensation energy $\mu_0 H_{c2}/2$ per unit volume. Changes in the order parameter occur within the coherence volume ξ^d.

Therefore, when the thermal energy k_BT satisfies the following equation, the generation of Cooper pairs begins near T_c due to thermal fluctuation.

$$k_BT \sim \xi^d \frac{\mu_0 H_{c2}}{2} \tag{2.30}$$

Vortexes are also generated even if the whole system is in a superconducting state. The former is called amplitude fluctuation in superconductivity, and when the volume of the system is larger than the coherence volume, the normal resistance begins to decrease above T_c. The latter is called phase fluctuation in superconductivity and causes residual resistance below T_c. As can be seen from Eq.2.30, the lower the dimension d, the smaller the energy required for these quantum fluctuations. Therefore, the effect appears more prominently in two-dimensional superconductors.

The correction of electrical resistance near T_c due to amplitude fluctuation is expressed as follows[1] - [3].

$$\rho = \frac{1}{\sigma_0 + \sigma_{AL} + \sigma_{MT}} \tag{2.31}$$

$$\sigma_{AL} = \frac{e^2}{16\hbar} \cdot \frac{T_c}{T - T_c} \tag{2.32}$$

$$\sigma_{MT} = \frac{e^2}{8\hbar} \cdot \frac{T_c}{T - (1+\delta)T_c} \ln \frac{T - T_c}{\delta T_c} \tag{2.33}$$

σ_{AL} is called the Aslamazov-Larkin (AL) term and represents the decrease in resistivity due to Cooper pairs generated by thermal fluctuations. Also, σ_{MT} is called the Maki-Thompson (MT) term and represents the decrease in resistivity due to quasiparticles caused by the destruction of Cooper pairs after formation. Therefore, the MT term includes a pair-breaking parameter δ that expresses the strength of the anti-breaking effect. δ is a material-specific value, typically around 0.1. A large value of δ means deviation from mean-field superconductivity.

References

[1] A. Larkin and A. Varlamov, Theory of Fluctuations in Superconductors (Claren- don Press, 2005).

[2] R. S. Thompson, Phys. Rev. **B**. 1, 327 (1970).

[3] T. Uchihashi, P. Mishra, and T. Nakayama, Nanoscale Res. Lett. **8**, 167 (2013).

Chapter 3 Experimental techniques

Chapter 3 introduces the experimental methods used in this study.

3.1 Vacuum

Atomic-layer superconductors easily transition to insulators when disturbances such as adsorption of impurities are introduced. Therefore, this research was carried out in an ultra-high vacuum (UHV) environment from sample preparation to measurement.

The temperature dependence of the pressure with the number of molecules N incident on a unit area per unit time is expressed by the following equation [1].

$$N[/m^2 s] = 2.6 \times 10^{24} \times \frac{P}{\sqrt{MT}} \tag{3.1}$$

where M is molecular weight, T is temperature, and P is pressure. Since the gas molecules contained in the atmosphere are mainly nitrogen, when the incident molecule is nitrogen ($M = 28$) at room temperature environment ($T = 300$ K), Eq.3.1 is converted to the following equation.

$$N = 2.8 \times 10^{24} \times P \tag{3.2}$$

The density of a monoatomic-layer is about $10^{19}/m^2$ when the molecular size is 3 Å, so it is $N \sim 3 \times 10^{18}$ in a high vacuum ($\sim 10^{-4}$ Pa). Assuming that all nitrogen molecules colliding with the sample are adsorbed, the surface layer is covered with impurities in about 3 seconds. However, under the same conditions, in UHV ($\sim 10^{-8}$ Pa), it is calculated that one layer of the surface is covered with impurities in about 8 hours, and it is possible to keep the surface clean at the atomic level for several hours. In reality, not all the gas molecules that collide are adsorbed, so the measurement conditions are less strict than this measurement condition, but it can be understood that a good vacuum is important for accurate surface analysis [2].

3.2 Low Energy Electron Diffraction

Low Energy Electron Diffraction (LEED) can identify the periodic structure of the material surface by measuring the diffraction pattern of electrons that are irradiated and scattered when the surface of the sample forms a periodic structure. In this study, it was

used to confirm whether Indium atoms adsorbed on a Si(111) substrate form a $\sqrt{7} \times \sqrt{3}$ superstructure.

3.2.1 Fundamentals of LEED

When an electron collides with a solid, it either reflects off the solid surface or enters the solid interior. When electrons collide with a solid surface, some of the electrons are scattered by the atoms that make up the solid because the electrons have wave properties. This reflection reflects the regularity of the atomic arrangement on the solid surface. The wavelength λ of the electron beam can be expressed as $\lambda = h/p$ from the de Broglie wave relational expression, where p is the electron's momentum and h is the Planck constant. Since the kinetic energy E_k $[eV]$ of an electron can be expressed by $E_k = p^2/2m$ when the effective mass of the electron is m^*, the relationship between the energy of the electron and the wavelength is given by the following equation.

$$\lambda = \frac{h}{\sqrt{2m^* E_k}} \approx \sqrt{\frac{1.504}{E_k}} \ \ [nm] \tag{3.3}$$

From Eq.3.3, it can be seen that the wavelength of electron beams with energies of several tens to several hundred electron volt is about 0.1 to 0.5 nm, which is about the same as the lattice spacing. Therefore, even when the electron beam is incident perpendicular to the surface, diffraction reflecting the atomic arrangement of the surface occurs. In addition, since electrons with energies of several tens to several hundred electron volt penetrate into the solid to a depth of about 1 nm, the reflected electron beam produces a diffraction pattern that reflects only the information near the surface.

Next, consider the case where electrons with wavelength λ are diffracted by homogeneous atoms arranged one-dimensionally on the surface with a spacing d (Fig.3.1). Electrons are incident at the incident angle θ_0 and is reflected in the direction of the reflection angle θ.

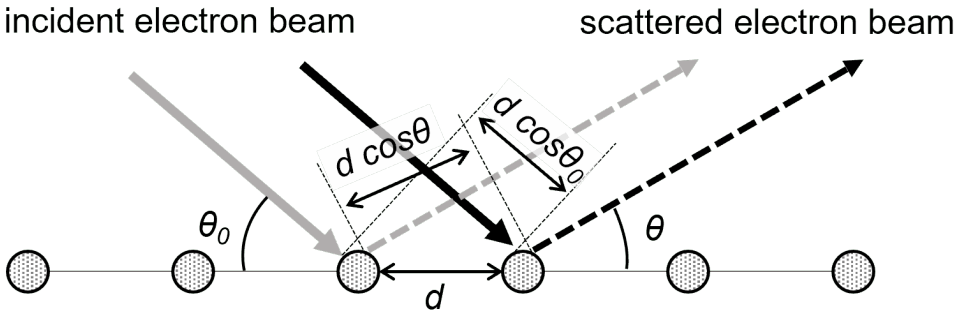

Figure 3.1 **Electron diffraction by atoms in one-dimensional array.** The incident electron beam come from the incident angle θ_0 and are reflected to the reflect angle θ.

The path difference is $d\cos\theta_0 - d\cos\theta$, and electrons reinforce each other when this path difference is an integral multiple of the wavelength n.

$$\frac{\cos\theta_0 - \cos\theta}{\lambda} = \frac{n}{d} \tag{3.4}$$

Therefore, the surface atomic spacing d and the periodic structure of the atomic arrangement can be obtained from the reflection angle θ and the diffraction pattern.

3.2.2 Ewald sphere

The atomic arrangement on the crystal surface can be treated as a two-dimensional crystal. In the case of diffraction from a three-dimensional crystal, the intersection of a reciprocal lattice point on the reciprocal space and a sphere with a radius of $1/\lambda$ (Ewald sphere) gives the diffraction point. On the other hand, in the energy region of the electron beam used in LEED, the penetration depth of the electron beam is near the surface where there is no periodicity in the vertical dimension, so the diffraction condition is relaxed in a rod-like manner. This perpendicular rod-like diffraction condition is called reciprocal lattice rods, and the intersection of the reciprocal lattice rods and the Ewald sphere is the diffraction point. Fig.3.2(a) shows a schematic diagram of the case where the electron beam is incident perpendicular to the sample surface. In the LEED measurement, the

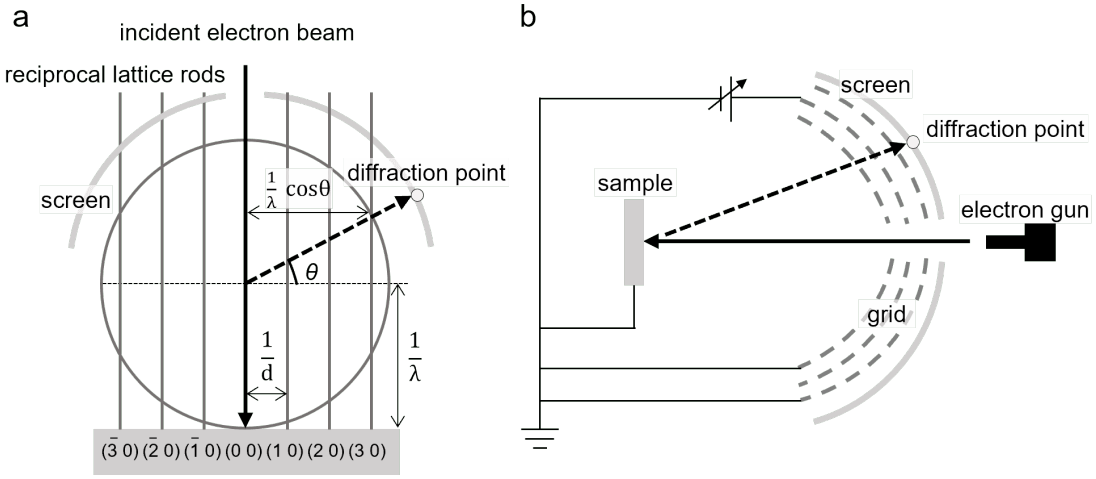

Figure 3.2 **The schematic image of LEED fundamentals.** (a) The schematic image of diffraction spot obtained by LEED. The intersection of the reciprocal lattice rods and the Ewald sphere is the diffraction point. The center of the Ewald sphere is located on the incident axis of the electron beam at a distance of $1/\lambda$ from the origin of the reciprocal lattice space. (b) The schematic image of LEED equipment. The sample and two grids are grounded. A stopping potential is applied to the central sheet to remove electrons inelastically scattered by the sample. A voltage of 2 to 6 kV is applied to the screen to accelerate the electrons that have passed through the final grid and cause the screen to emit light.

incident angle θ_0 of incident electrons is 0, so the diffraction condition is given by the following relationship from Fig.3.2(a).

$$\frac{\cos\theta}{\lambda} = \frac{n}{d} \tag{3.5}$$

That is, an electron beam reflected in a direction that satisfies the condition of Eq.3.5 is observed. From this pattern of diffraction spots, the symmetry of the ordered array on the sample surface can be identified, and if the distance between the sample screens is known, the diffraction angle θ (lattice constant of the ordered array) can be identified.

3.2.3 LEED experimental equipment

Fig.3.2(b) shows a conceptual diagram of the equipment used in general LEED measurements. Electrons are injected perpendicularly to the sample from the electron gun located at the center of the figure (black arrow). The electrons reflected by the sample surface are accelerated and collide with the fluorescent screen when they reach it. As discussed in subsection 3.2.2, diffraction spots appear on the screen that depends on the symmetry of the surface ordering (LEED pattern). As shown in the figure, since the screen is hemispherical, in the LEED pattern, the farther away from the center of the screen, the greater the contribution of the hemispherical distortion. Therefore, it is necessary to pay attention to the evaluation of the symmetry of the diffraction spots.

3.3 Scanning Tunneling Microscopy

Scanning Tunneling Microscopy (STM) is an atomic resolution microscope developed by Gerd Binnig et al. in 1982 [3]-[5]. They won the Nobel Prize in Physics in 1986. The STM detects tunneling currents by bringing a metal probe with a sharp tip close to the sample surface to about 1 nm and applying a voltage of several mV to several V between the probe and the sample. The tunneling current is exponentially dependent on the distance between the probe and the sample, and scanning the sample surface with feedback to keep the tunneling current constant allows direct observation of the sample surface structure with atomic resolution.

3.3.1 Tunnelling effect

In classical mechanics, an electron between two metal electrodes cannot cross the vacuum barrier when the electron's energy is less than the vacuum barrier. However, quantum mechanically, the electron wavefunction exponentially decays within this barrier, while the electron moves to the other electrode with a finite probability. This is called the tunneling effect. In order to understand the basic principle of STM, we explain the tunneling phenomenon of electrons in a one-dimensional finite potential barrier and show that there

is a high resolution in the height direction (z direction) of the sample.

Consider a tunneling current flowing between two electrodes A and B shielded by a potential. The one-dimensional Schrödinger equation for the one-electron wavefunction moving between electrodes A and B can be expressed as follows.

$$\left[-\frac{\hbar^2}{2m}\frac{\partial^2}{\partial z^2} + V(z)\right]\Psi = E\Psi \tag{3.6}$$

$$V(z) = \begin{cases} 0 & (z < 0, z_0 < z) \\ V_0 & (0 < z < z_0) \end{cases} \tag{3.7}$$

The general solution of this Schrödinger equation is given as follows.

$$\Psi(z) = Ae^{\kappa z} + Be^{-\kappa z}, \quad \kappa = \frac{\sqrt{2m(V_0 - E)}}{\hbar} \tag{3.8}$$

Here, A and B represent arbitrary constants. Considering that the wavefunction is single-valued continuous finite in each region, we can calculate the wavefunction Ψ and the tunneling transition probability T from the boundary conditions. Considering that the potential barrier width z_0 is sufficiently large with respect to the wavelength in STM ($\kappa z_0 >> 1$), the tunnel current and tunneling probability function are expressed by the following equations.

$$I \propto \left|T^2\right| \propto e^{-2\kappa z_0} \tag{3.9}$$

It is assumed that the tunneling current is proportional to the tunneling transition probability. Equation. 3.9 shows that the tunneling current is very surface sensitive as it depends exponentially on the tip-sample distance.

3.3.2 Tunneling current

The tunneling current in actual STM measurements does not depend only on the work function and the tip-sample distance as in Eq.3.9. Therefore, in this subsection, we formulate the tunneling current in more detail and consider its properties.

A general theory of STM was proposed by J.Tersoff and D.R.Hamann [6]. They regarded the tip shape as a spherical potential, as shown in Fig.3.3, and approximated it as an s-orbital wave function that decays exponentially in a vacuum. In this case, the tunneling current in the low temperature/low bias region is described by the following equation.

$$I \propto V\phi_t^2 \frac{R^2 e^{2\kappa R}}{\kappa^4} \rho_t(E_F) \sum_n \left|\Psi_n(r_0)\right|^2 \delta\left(\epsilon_n - E_F\right) \tag{3.10}$$

where R is the radius of curvature of the tip, ϕ_t is the work function of the tip, $\rho_t(E)$ is the local density of states (LDOS) of the tip, and r_0 is the tip position. In addition, Ψ_n, ϵ_n represent the expected value of the wavefunction seeping from the surface and its

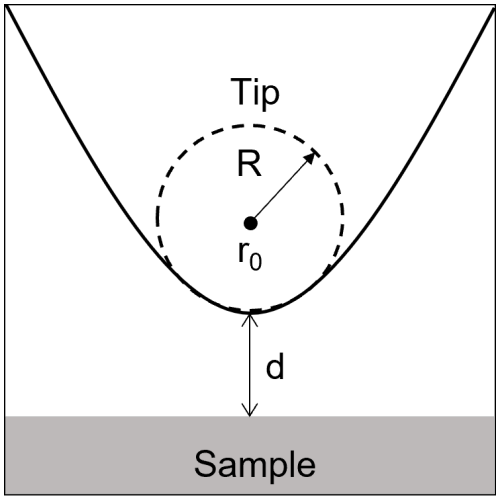

Figure 3.3 **Schematic diagram of the Terrsoff-Hamann model.** The tip shape is regarded as a spherical potential and approximated by an s-orbital wave function that decays exponentially in a vacuum.

Hamiltonian. Furthermore, this equation was extended by the new model proposed by N.Lang [7]. The model assumes that one atom is adsorbed on two metal plate electrodes. From this model, the tunneling current is expressed by the following equation.

$$I \propto \int_{E_F}^{E_F+eV} dE\ \rho_t(E-eV)\rho_s(E)T(z,E,eV) \tag{3.11}$$

where $T(z,E,eV)$ is the tunneling transition probability. From Eq.3.11, it can be seen that the tunneling current depends on the LDOS of the tip, sample and the tunneling transition probability. Therefore, the STM image in the constant current mode can be interpreted as tracing the contour lines of the local density of states on the surface. When a weak voltage is applied between the electrodes, the LDOS of the tip and the tunneling transition probability can be considered constant, so the first derivative of the tunneling current with respect to the applied voltage is proportional to the LDOS of the sample surface.

Using the quasi-classical Wentzel-Kramers-Brillouin (WKB) approximation, the tunneling transition probability is expressed by the following equation [8].

$$T(z,E,eV) \simeq \exp\left[-2z\sqrt{\frac{2m}{\hbar^2}\left(\frac{\phi_s+\phi_t}{2}+\frac{eV}{2}-E\right)}\right] \tag{3.12}$$

where ϕ_s, ϕ_t represents the work function of the sample surface and the tip. From Eq.3.12, it can be seen that the tunneling transition probability, which greatly contributes to the tunneling current, strongly depends on the probe-sample distance. Furthermore, since the work function of the probe also contributes, the tunneling current is also affected by changes in the shape of the probe due to molecular adsorption during STM measurements.

Considering the tunneling junction in STM, the LDOS can vary greatly depending on the positive and negative voltage applied to the sample. This is because the electron tunneling transition direction differs depending on the voltage. The voltage dependence of the STM image is particularly pronounced when measuring substances such as organic molecules in which the spatial distribution of electron orbits strongly depends on the voltage [9]. Fig.3.4 shows the energy diagram of the tunneling process that occurs at the tunnel junction of the organic molecular film and metal probe. When the voltage applied to the sample is positive (V>0), electrons tunnel from the occupied state of the tip to the unoccupied state of the organic molecule as shown in Fig.3.4(b). An STM image reflecting Lowest Unoccupied Molecular Orbital (LUMO) is obtained. On the other hand, when a negative voltage (V<0) is applied to the sample, electrons tunnel from the occupied state of the organic molecule to the unoccupied state of the tip, as shown in Fig.3.4(c). An STM image reflecting Highest Occupied Molecular Orbital (HOMO) is obtained.

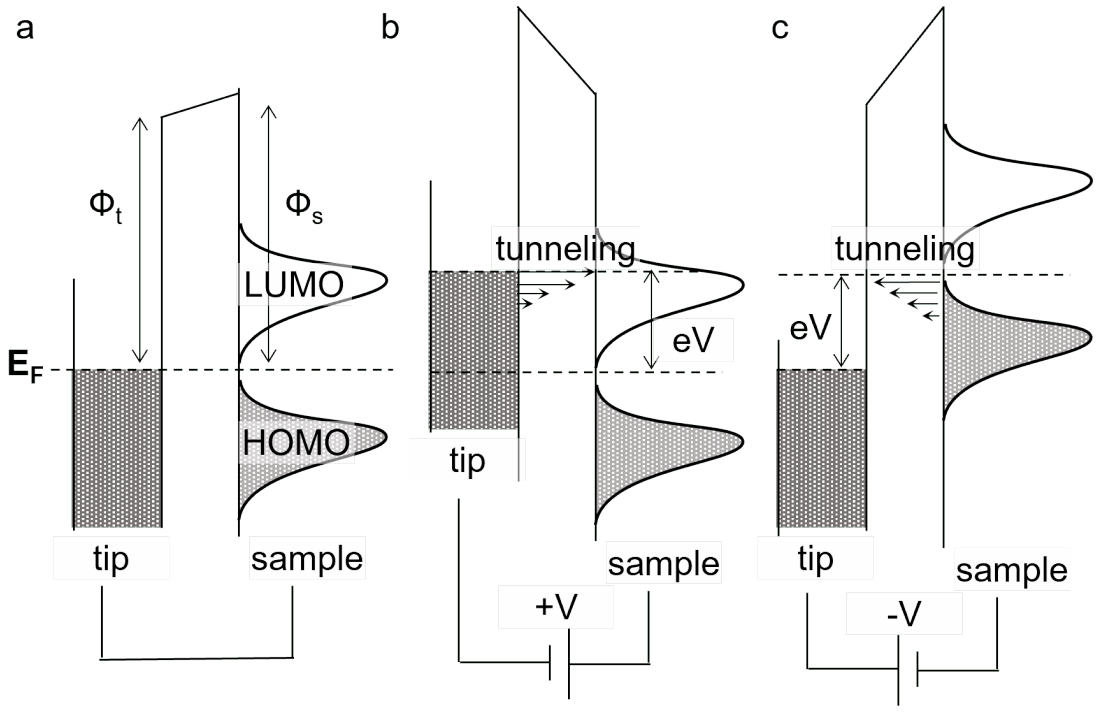

Figure 3.4 **Energy diagram of tunneling process in STM.**(a) Tunneling junction of organic molecular film and metal tip. (b) When a positive voltage is applied to the sample. Tunneling transition from the occupied level of the tip to the unoccupied level of the sample. That is, the tunneling current reflects the LDOS of the unoccupied levels of the sample. (c) When a negative voltage is applied to the sample. A tunneling transition occurs from the occupied level of the sample to the unoccupied level of the tip. That is, the tunneling current reflects the LDOS of the occupied levels of the sample.

3.3.3 STM experimental equipment

Fig.3.5 shows a schematic diagram of STM measurement. The probe scans the sample surface with a piezoelectric element called a piezo tube. By applying a voltage to the piezo tube from the controller in accordance with the detected tunneling current value, it is possible to control the movement of the probe so as to trace the surface of the sample. The changes in the voltage applied to the piezo tube and the detected tunneling current are captured as changes in surface topography.

STM has two measurement modes. One is the constant current mode. In this constant

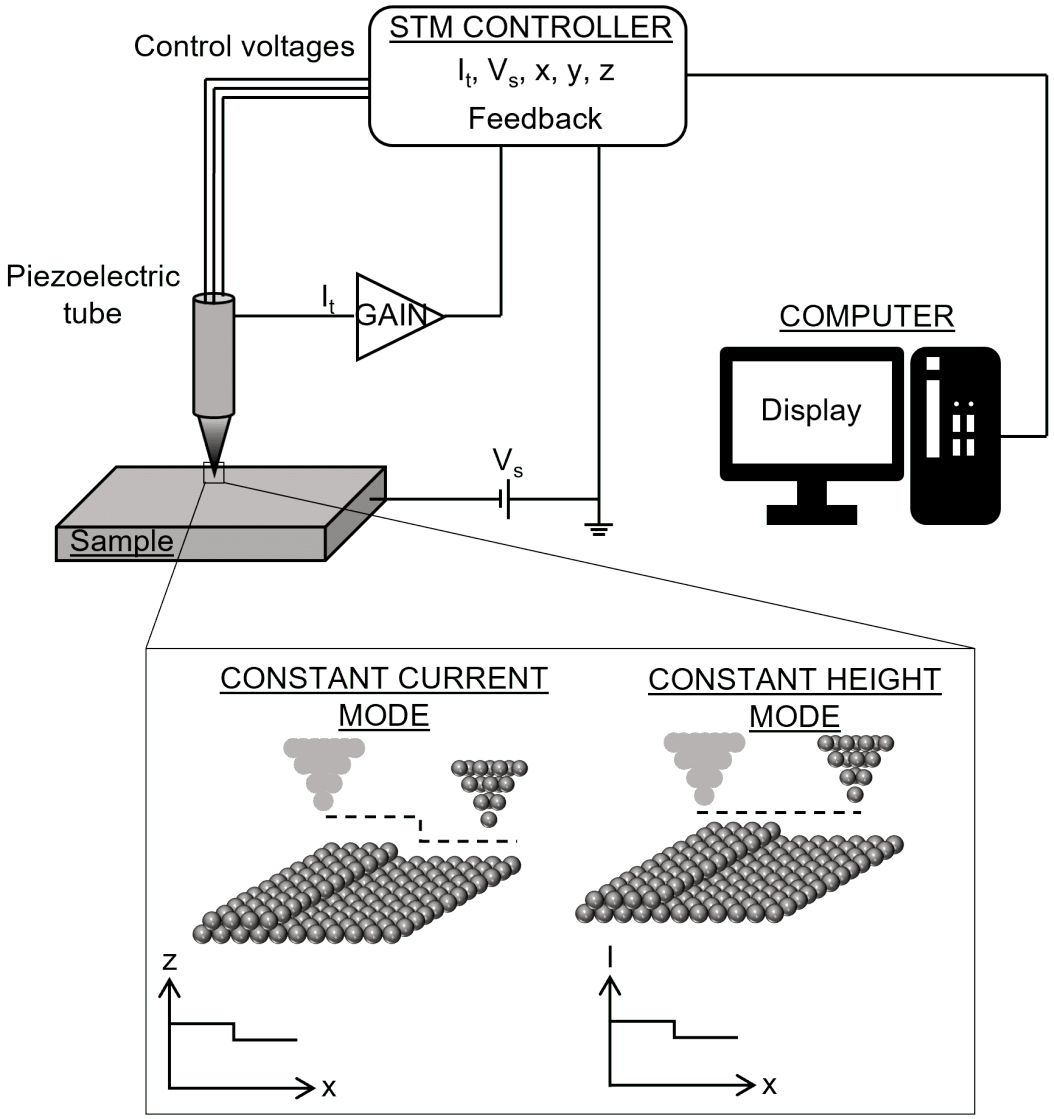

Figure 3.5 **Schematic diagram of the STM equipment.** The tunneling current and sample shape information input to the STM controller are output to a personal computer and can be monitored in real-time.

current mode, feedback is applied so that the flowing tunneling current is constant, and by scanning the sample surface, the voltage applied to the piezo tube is obtained as height information of the surface shape. Therefore, the probe moves so as to trace the surface of the sample. There is also constant height mode as the other measurement mode. In this measurement mode, feedback is turned off, and the flowing tunneling current is measured while the probe is scanned at a constant height with respect to the sample surface. Height information of the sample surface can be obtained from the intensity of this tunneling current. Both are non-contact with the sample, and it is possible to measure the surface shape without destroying the sample.

3.4 Electron transport measurements

Electron transport measurements (transport measurements) can detect zero resistance, the most typical feature in superconductivity. In this study, T_c is determined by measuring the temperature dependence of the sample resistance from transport measurements. Another representative method for detecting superconducting T_c is superconducting gap measurement by Scanning Tunneling Spectroscopy (STS) [10]. STS is a very powerful experimental technique which can be combined with STM to obtain correlations between real-space-scale microscopic structures and superconducting properties [11, 12]. However, the superconducting gap detected by STS only suggests the formation of Cooper pairs on a local scale and does not imply the formation of the long-range order of Cooper pairs that is characteristic of superconductors. In fact, the T_c obtained from superconducting gap measurements by STS is higher than that found in transport measurements [13, 14].

In this section, after explaining the four-terminal measurement generally performed in transport measurements, we introduce the electrode fabrication method and the fitting function used to determine T_c for atomic-layer superconductivity in this study.

3.4.1 Four-terminal measurement

The four-terminal measurement method, which is generally used in transport measurements, can ignore the influence of contact resistance and can accurately measure the resistance of the sample you want to measure. This subsection introduces the basic principles of four-terminal measurements and shows that in practice contact resistance can be ignored.

Consider a four-terminal measurement circuit as shown in Fig.3.6 (a). Here, R_1 and R_4 are the contact resistances of the current application terminals, and R_2 and R_3 are the contact resistances of the voltage measurement terminals. R_V is the internal impedance of the voltmeter, and R_S is the sample resistance to be measured. Considering that a current I flows through this circuit, the applied current I can be expressed by the sum of

the current I_1 flowing through the sample and the current I_2 flowing through the voltmeter according to Kirchhoff's current law.

$$I = I_1 + I_2 \tag{3.13}$$

Also, the potential difference of the sample is given by the following equation from Kirchhoff's voltage law.

$$I_1 R_S = I_2 R_2 + I_2 R_3 + I_2 R_V, \quad V = I_2 R_V \tag{3.14}$$

Here, the fact that the product of the internal impedance and the current I_2 represents the measured voltage V is used. Also, the electrical resistance can be expressed by the following equation from the ratio of the measured voltage and current.

$$\frac{V}{I} = R_S - (R_S + R_2 + R_3) \cdot \frac{I_2}{I} \tag{3.15}$$

The second term on the right side of Eq.3.15 is the difference between the measured resistance and the sample resistance. However, the ratio I_2/I between the current flowing through the voltmeter and the applied current in Eq.3.15 can be expressed by the following equation.

$$\frac{I_2}{I} = \frac{R_S}{R_2 + R_3 + R_S + R_V} \tag{3.16}$$

Considering that the contact resistance is at most about 1Ω, by using a voltmeter with a sufficiently large internal impedance R_V compared to the resistance value R_S of the sample, $I_2/I \to 0$ from Eq.3.16, that is, the current flowing through the voltmeter becomes

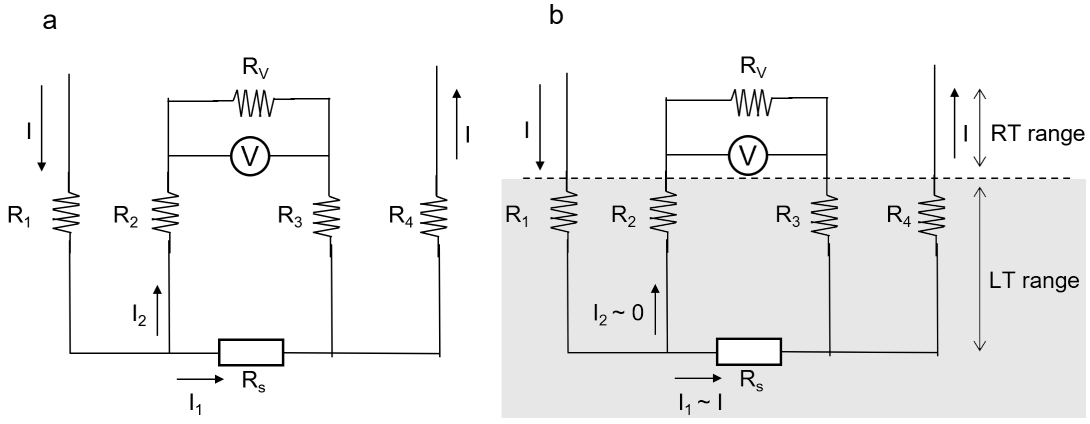

Figure 3.6 **Schematic for four-terminal measurement.** (a) Current I is applied. R_1 and R_4 are the contact resistances of the current application terminals, and R_2 and R_3 are the contact resistances of the voltage measurement terminals. R_V is the internal impedance of the voltmeter, and R_S is the sample resistance to be measured. (b) RT indicates room temperature (300 K) and LT indicates low temperature (1.7 K).

$I_2 \to 0$. Since a voltmeter with a large internal impedance V is used in actual four-terminal measurement, the contribution of contact resistance can be ignored. On the other hand, when a sample with a large sample resistance R_S is measured, I_2 does not become 0, and the error contribution increases.

The sample measured in this study is a superconductor with $T_c \sim 3K$. Therefore, it is necessary to cool the sample to an extremely low temperature, which is about 1.7 K or even lower in actual measurements. In this case, the vicinity of the measuring instrument is at room temperature, and the temperature gradient within the measuring circuit is extremely large. Since the resistance of metal used in wiring changes with temperature, the difference in resistance due to this temperature gradient appears as an error in the transport measurement of superconductors. Here, we introduce a measurement method that reduces the effect of error due to this temperature gradient. Consider a four-terminal measurement circuit using a voltmeter with sufficient internal impedance, as shown in Fig.3.6(b). Considering that the error due to the temperature gradient is incorporated as the potential difference V_{th}, the measured voltage V^+ is given by the following equation when the current I^+ is applied.

$$V^+ = IR_S + V_{th} \tag{3.17}$$

The second term on the right side of Eq.3.17 is the difference from the sample resistance. It can be seen that this resistance difference cannot be ignored even using four-terminal measurements. Next, when I^-, which is equal in magnitude to the applied current I^+ but opposite in direction, is applied, the measured voltage V^- is expressed by the following equation.

$$V^- = -IR_S + V_{th} \tag{3.18}$$

Therefore, when we measure both V^+ and V^- ,

$$\frac{V^+ - V^-}{2I} = R_S \tag{3.19}$$

from Eq.3.19, it can be seen that the error due to the temperature gradient can be ignored.

3.4.2 Electrode fabrication method

Electrode fabrication is essential for stable transport measurements. In general, electrodes are attached using silver paste or the like in the atmosphere. However, atomic-layer superconductors with surface superstructures, which are the subject of this research, are strongly affected by disturbances and easily undergo insulation transition. Therefore, it is necessary to fabricate electrodes in UHV. There are two approaches to fabricating electrodes in UHV. One is to use the STM tip as a movable nanoprobe [15, 16] and the other is to fabricate a fixed electrode structure on the sample [17, 18]. The former has the advantage of being able to freely adjust the electrode spacing and select the location on the

sample surface to be measured. However, in general, it is necessary to pay attention to the contact of the probe, and temperature drift has an effect, especially in measurements involving large temperature changes. On the other hand, in the latter method, the spacing and position of the electrodes cannot be freely selected, but once electrodes with stable and good characteristics can be produced, stable measurements can be carried out. In this study, we chose the latter method.

Generally, to fabricate an electrode on a sample, an electrode material is deposited on the surface. However, in the preparation of Si(111)-($\sqrt{7} \times \sqrt{3}$)-In used in this study, Si(111) is heated at 1250 °C for cleaning. In addition, when metals are adsorbed on ($\sqrt{7} \times \sqrt{3}$)-In, they are alloyed, and the structure is destroyed. Therefore, in this study, patterning was performed by Ar^+ sputtering. Fig.3.7(a) shows the electrode fabrication method used in this study. A shadow mask is brought close to the sample to cover the conducting area. After that, Ar^+ sputtering (E = 0.2 keV, Emission current = 32 mA) is performed, to remove unnecessary regions [19, 20]. A schematic diagram of the patterned sample is shown in Fig.3.7(b). The white area represents the unetched area, and the gray area represents the Ar^+ sputtered area. Since the conductive region is not connected to the edge of the sample, there is no need to consider the effects of current flowing along the edge. In this research, the area where the voltage is actually measured is the area within

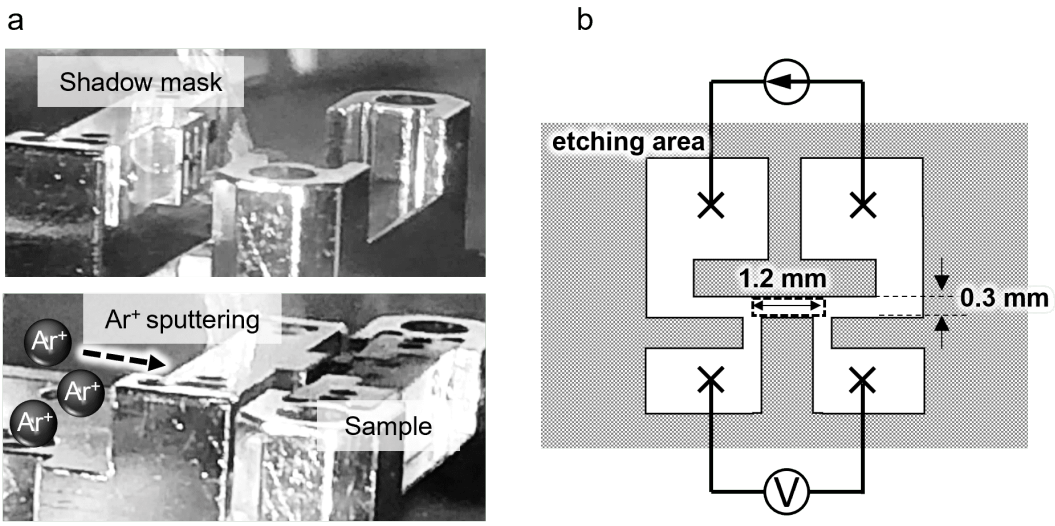

Figure 3.7 **Photograph and Schematic illustration of electrode fabrication.** (a) Fabrication of electrode patterning by Ar^+ sputtering through a shadow mask. The shadow mask is brought close to the sample and only the unnecessary area is etched by Ar^+ sputtering. (b) Schematic diagram of the patterned sample. The white areas represent the unetched areas and the gray areas represent the areas etched with Ar^+ sputtering.

the dotted frame in the center, which is 1.2 mm × 0.3 mm. Therefore, by dividing the measured resistance by 1/4, it can be converted to sheet resistance.

3.4.3 Fitting function for T_c determination

As introduced in subsection 2.4.4, two-dimensional superconductors are susceptible to quantum fluctuations, which modulate the temperature dependence of electrical resistance near T_c. Amplitude fluctuations produce a precursor state in which the resistance begins to drop above T_c. Electrical resistance can be corrected by the AL and MT terms in Eq.2.31, 2.32, 2.33, but they are complex and cumbersome. In this subsection, we introduce the simplified fitting function and the T_c determination method used in this study.

The fitting function used in this study is shown in the following equation [21].

$$R_{\mathrm{sheet}}(T) = \left(G_{\mathrm{2D,n}}(T) + G_{\mathrm{2D,s}}(T)\right)^{-1} \tag{3.20}$$

$$G_{\mathrm{2D,n}}(T) = \left(R_n + aT^b\right)^{-1} \tag{3.21}$$

$$G_{\mathrm{2D,s}}(T) = \frac{1}{R_0}\frac{T}{T - T_c} \tag{3.22}$$

where $G_{\mathrm{2D,n}}(T)$ is the normal conductance, and $G_{\mathrm{2D,s}}(T)$ is the contribution to the conductance due to superconducting amplitude fluctuations above T_c. Here, R_n is the residual normal resistance at T = 0, and aT^b is the temperature dependence of the resistance of ordinary metals. where a, b, R_0, are fitting parameters. Equation 3.22 looks very similar

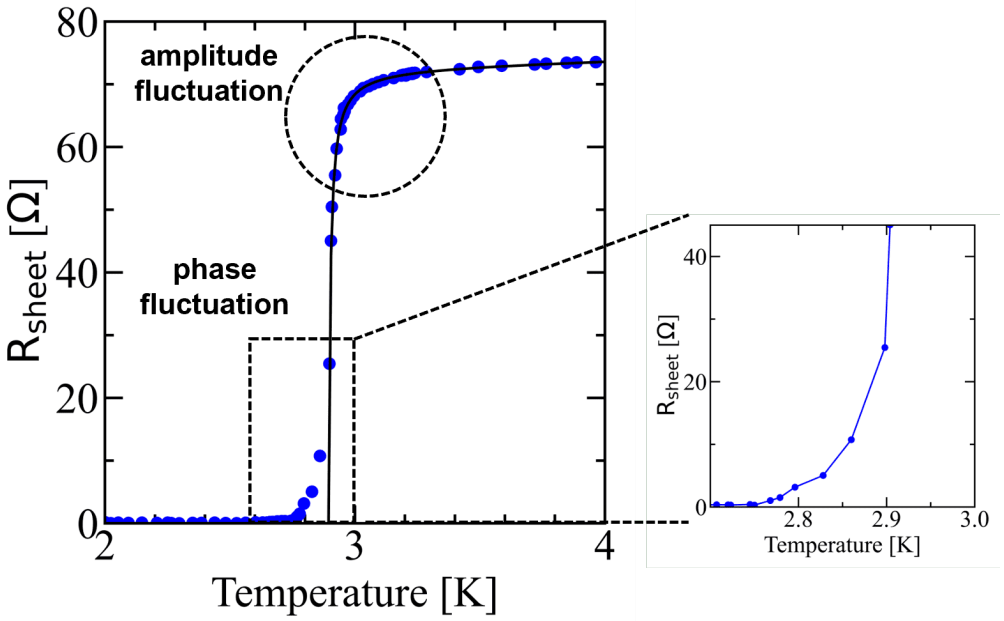

Figure 3.8 **Results of fitting for T_c determination.** Blue points indicate experimental results and black lines represent fitting functions.

to the AL term of Eq.2.32, and the fitting function Eq.3.20 does not appear to reflect the effect of the MT term. As can be seen from Eq.2.33, the MT term includes material-specific parameters, and if the MT term is incorporated into the fitting function correctly, the fitting parameters increase and become complicated. Therefore, the resistance change due to the MT term is included in R_0 to simplify the fitting function and make it easier to handle. Fig.3.8 shows the results of the actual fitting. Blue points indicate measurement results and black lines represent fitting functions. It can be seen that the fitting function agrees very well with the experimental results above T_c. Below T_c, the fitting does not go well, but this is the effect of phase fluctuations and does not affect the T_c determination. The fitting range was taken to be 0.6 $R_{mean} < R_{sheet} < R_{mean}$, where R_{sheet} is the experimental value of sheet resistance obtained by transport measurements and R_{mean} is defined as the average of R_{sheet} measured in the range 4 K < T < 5 K.

3.5 Density Functional Theory

In this study, *ab initio* calculations based on Density Functional Theory (DFT) was performed for evaluation of DOS of $(\sqrt{7} \times \sqrt{3})$-In and spin magnetic moment and charge transfer of ZnPc on $(\sqrt{7} \times \sqrt{3})$-In. This section provides a brief overview of DFT.

In 1964, Hohenberg and Kohn proved the following theory [22]. This theorem is called the Hohenberg-Kohn theorem. The total energy E_0 of an electronic system without degeneracy in the ground state is given by the function of the electron density $n_0(\mathbf{r})$ in the ground state. $n(\mathbf{r})$ that minimizes E gives the ground state of the system (energy variational principle). That is, it can be represented by the following equation.

$$E_0 = E\left[n_0(\mathbf{r})\right] \tag{3.23}$$

$$E_0 = E\left[n_0(\mathbf{r})\right] \leq E\left[n(\mathbf{r})\right] \tag{3.24}$$

These theorems are mathematically warranted for their conceptual correctness and can be considered fundamental theorems of quantum theory based on electron density. However, from the Hohenberg-Kohn theorem, we could not know the concrete form of the functional. In other words, the task was to develop functionals that give the correct minimum energy expectations for kinetic energy and electron-electron interaction energy.

In 1965, Kohn and Sham jointly developed an electronic states calculation method based on the Hohenberg-Kohn theorem to solve this problem [23]. The Kohn-Sham method is a method for obtaining the lowest energy and the corresponding molecular orbital according to the variational principle for the electron-electron interaction potential, which is a function of electron density. Here, the energy function is given by the following equation.

$$E\left[n(\mathbf{r})\right] = T\left[n(\mathbf{r})\right] + \frac{1}{2}\int\int \frac{n(\mathbf{r}')}{|\mathbf{r}-\mathbf{r}'|} n(\mathbf{r}) d\mathbf{r} d\mathbf{r}' + E_{xc}\left[n(\mathbf{r})\right] + \int V_{ext}(\mathbf{r}) n(\mathbf{r}) d\mathbf{r} \tag{3.25}$$

where $T[n(\mathbf{r})]$ is the kinetic energy, the second term on the left side is the Hartree term (Coulomb interaction), the third term on the left side is the exchange-correlation term, and the fourth term on the left side is the external potential term. The second and third terms on the left side are interactions between electrons. Considering the electron orbitals Ψ_i of the non-interacting system, the electron density $n(\mathbf{r})$ can be described using the electron orbitals Ψ_i as follows.

$$n(\mathbf{r}) = \sum_{i=1}^{N} \int \Psi_i^*(\mathbf{r})\Psi_i(\mathbf{r})d\mathbf{r} = \sum_{i=1}^{N} |\Psi_i(\mathbf{r})|^2 \tag{3.26}$$

Consider the true kinetic energy by dividing it into $T_s[n(\mathbf{r})]$ for a system without interaction and the deviation from it. Furthermore, this deviation is squeezed into the exchange-correlation term, and Eq.3.25 can be transformed using Eq.3.26 into the following equation.

$$E[n(\mathbf{r})] = T_s[n(\mathbf{r})] + \frac{1}{2}\int V_H(\mathbf{r})n(\mathbf{r})d\mathbf{r} + E_{xc}[n(\mathbf{r})] + \int V_{ext}(\mathbf{r})n(\mathbf{r})d\mathbf{r} \tag{3.27}$$

$$T_s[n(\mathbf{r})] = -\frac{\hbar^2}{2m}\sum_{i=1}^{N}\int \Psi_i^*(\mathbf{r})\nabla^2\Psi_i(\mathbf{r})d\mathbf{r} \tag{3.28}$$

where $V_H(\mathbf{r})$ denotes the Hartree term. $E_{xc}[n(\mathbf{r})]$ contains the kinetic energy deviation. This approximation makes use of the independent electron approximation formulation similar to the Hartree-Fock method for the kinetic energy rather than the electron density functional. This simple modification is most important in the Kohn-Sham method [24]. With this method, the many-body problem becomes a monolithic problem. After all, the simultaneous equations (Kohn-Sham equations) to be solved are as follows.

$$\left[-\frac{\hbar^2}{2m}\nabla^2 + V_{eff}(\mathbf{r})\right]\Psi_i(\mathbf{r}) = \epsilon_i\Psi_i(\mathbf{r}) \tag{3.29}$$

$$V_{eff}(\mathbf{r}) = \int \frac{n(\mathbf{r}')}{|\mathbf{r}-\mathbf{r}'|}d\mathbf{r}' + \frac{\delta E_{xc}}{\delta n} + V_{ext}(\mathbf{r}) \tag{3.30}$$

where the exchange-correlation functional potential is the first derivative of the exchange-correlation energy functional with respect to electron density. The remaining problem is what to adopt as the exchange/correlation functional. In this study, the DFT calculations of $(\sqrt{7}\times\sqrt{3})$-In and adsorbed $(\sqrt{7}\times\sqrt{3})$-In on ZnPc were performed using the Local Density Approximation (LDA) functional and the Generalized Gradient Approximation (GGA) functional. The iterative approximation method is adopted as the method of solving the equations.

3.6 Photoemission Spectroscopy

In this study, using Angle-resolved Photoemission Spectroscopy (ARPES), we evaluate the interaction and charge transfer between organic molecular films and $(\sqrt{7} \times \sqrt{3})$-In. This section describes the fundamentals of PES and ARPES.

3.6.1 Fundamentals of PES

When a material is irradiated with light, electrons are emitted due to the photoelectric effect. PES is a method of measuring the energy and intensity distribution of photoelectrons, and by measuring the binding energy of electrons emitted from a certain electronic state in a substance, it is possible to directly investigate the electronic states of a solid.

An energy diagram for PES measurements is shown in Fig.3.9. The lower left graph shows the density of states of the sample. The upper right graph is the photoelectron spectrum obtained by PES. When a photon with energy $h\nu > \phi$ is absorbed by a solid, electrons in the solid with binding energy E_b are excited, exceed the vacuum level E_{vac}, and are emitted into the vacuum with kinetic energy E_k. (photoelectric effect). This

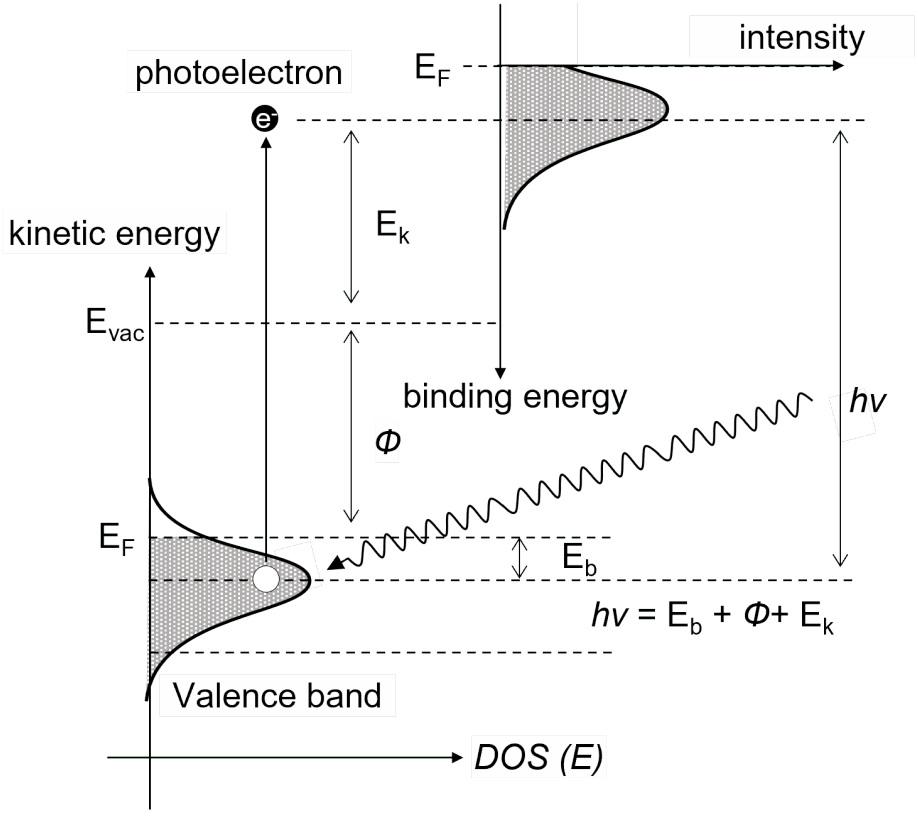

Figure 3.9 **Energy diagram of photoelectron excitation process in PES measurement.**

emitted electron is called a photoelectron. PES measures the kinetic energy E_k of this photoelectron. Assuming that the work function of the solid material surface is ϕ, the following energy conservation law holds.

$$E_k = h\nu - \phi - E_b \tag{3.31}$$

From Eq.3.31, if $h\nu$ and ϕ are known, E_b can be identified by measuring E_k. In other words, measuring E_k means measuring the electron density of states of the sample. When the sample is conductive, the energy can be specified with reference to the Fermi level by grounding the sample. However, in the photoelectron spectrum actually observed, electrons that are inelastically scattered due to the effects of multiple scattering, lattice vibration, and plasmons appear in the background as secondary electrons. Therefore, in discussing the peak position and intensity of the photoelectron spectrum obtained, it is necessary to process the background due to the secondary electrons. In addition, the escape depth of photoelectrons from the solid surface (mean free path of photoelectrons in the solid) differs due to the difference in the energy $h\nu$ of the incident photons.

3.6.2 Fundamentals of ARPES

ARPES can investigate the momentum dependence of electronic states by measuring not only the kinetic energy E_k of the photoelectrons emitted from the sample but also the momentum. A general measurement system of ARPES is shown in Fig.3.10. Among the photoelectrons emitted in all directions in a vacuum by the photoelectric effect, only those with a certain energy and momentum are detected by an electron analyzer. That is, the kinetic energy E_k of photoelectrons emitted at the emission angles θ and ϕ is measured.

Next, we describe the correspondence between the angle at which the photoelectrons are emitted and the band dispersion of the sample. When the effective mass of the photoelectron is m^* and the kinetic energy is E_k, the wave vector K of the photoelectron emitted at the angle θ is given by

$$K = \frac{\sqrt{2m^* E_k}}{\hbar} \tag{3.32}$$

In this case, the wavenumber vector $K_\perp$ in the perpendicular direction and the wavenumber vector $K_\parallel$ in the in-plane direction as viewed from the sample surface can be expressed by the following equations.

$$K_\perp = \frac{\sqrt{2m^* E_k}}{\hbar}\cos\theta, \quad K_\parallel = \frac{\sqrt{2m^* E_k}}{\hbar}\sin\theta \tag{3.33}$$

On the other hand, when the internal potential in the crystal is V_0, the wave vector k of the electron excited in the crystal is given by

$$K_\perp = \frac{\sqrt{2m^* \left(E_k + V_0\right)}}{\hbar} \tag{3.34}$$

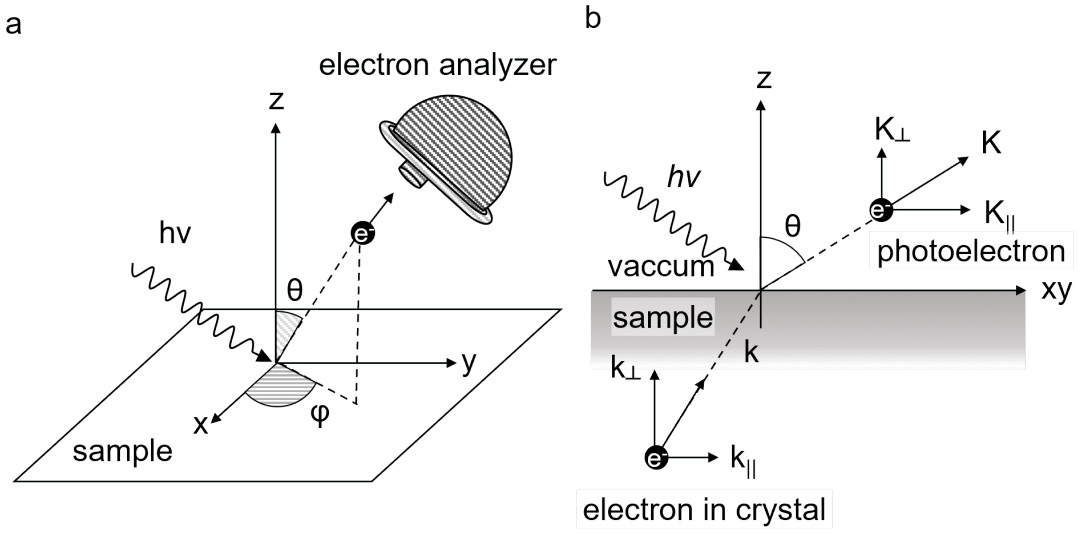

Figure 3.10 **Schematic image of photoemission.** (a) Schematic image of ARPES measurement. (b) Schematic image of in-plane momentum conservation of photoelectrons.

The perpendicular $k_\perp$ and in-plane $k_\parallel$ wavevectors of electrons excited in the crystal can be expressed by the following equations.

$$k_\perp = \frac{\sqrt{2m^* \left(E_k \cos^2\theta + V_0\right)}}{\hbar} \cos\theta, \quad k_\parallel = \frac{\sqrt{2m^* E_k}}{\hbar} \sin\theta \tag{3.35}$$

Comparing Eq.3.33 and Eq.3.35, we can see that the perpendicular wave vector $k_\perp$ is not conserved because it is affected by the internal potential during photoelectron emission. On the other hand, the in-plane wave vector satisfies the in-plane translational symmetry of the sample and is preserved, so the following equation holds.

$$K_\parallel = k_\parallel \tag{3.36}$$

Generally, it is difficult to determine the band dispersion because the perpendicular wave vector in the crystal and the perpendicular wave vector of the photoelectrons do not match. However, since low-dimensional electron systems have no momentum in the perpendicular direction, the band dispersion can be easily determined from Eq.3.36. The same is true for the atomic-layer superconductor $\left(\sqrt{7} \times \sqrt{3}\right)$-In in this study.

3.7 Experimental equipment

In this section, the experimental equipment used in my research will be introduced.

3.7.1 UHV - LT - Transport

A schematic diagram and a photograph of the apparatus for transport measurements used in this study are shown in Fig.3.11(a). The apparatus consists of a preparation chamber ($< 2.0 \times 10^{-8}$ Pa) for sample preparation and an analysis chamber ($< 2.0 \times 10^{-11}$ mbar) with an integrated LT-transport unit RT-STM unit. Both chambers are kept in UHV, and the experimental cycle of sample preparation, sample evaluation, and transport measurement can be performed without breaking UHV. In the preparation chamber, it is possible to degas the sample introduced from outside the chamber, clean Si substrate, and prepare the sample by metal deposition. In addition, sample electrode fabrication (subsection 3.4.2) and organic molecular deposition can also be performed. In addition, LEED equipment is installed to characterize the prepared samples. The analysis chamber incorporates RT- STM for further characterization of the surface structure of the sample. This STM applies a voltage to the probe and detects the tunneling current flowing through the sample. Transport measurements are performed on the high-quality samples characterized in the analysis chamber.

It is possible to cool down the transport head from room temperature to 1.7 K by liquid helium flow and pumping using a variable temperature cryostat (ARS Helitran). To prevent thermal radiation from room temperature, the transport head is surrounded by a helium return cooled radiation shield and a liquid nitrogen shield, as shown in Fig.3.11(b). A gold-coated spring probe is used as the terminal for transport measurement (Fig.3.11(c)). Good contact with the sample is always maintained by the spring in the contact probes and the contact resistance is less than several ohms even if the temperature changes. In the transport measurement, the temperature dependence of the sample resistance is obtained by running a current of $\pm$ 1 μA while measuring the sample temperature and detecting the voltage. In addition, the prepared samples can be transferred to other apparatus without exposure to the atmosphere using a UHV suitcase ($< 5.0 \times 10^{-11}$ mbar).

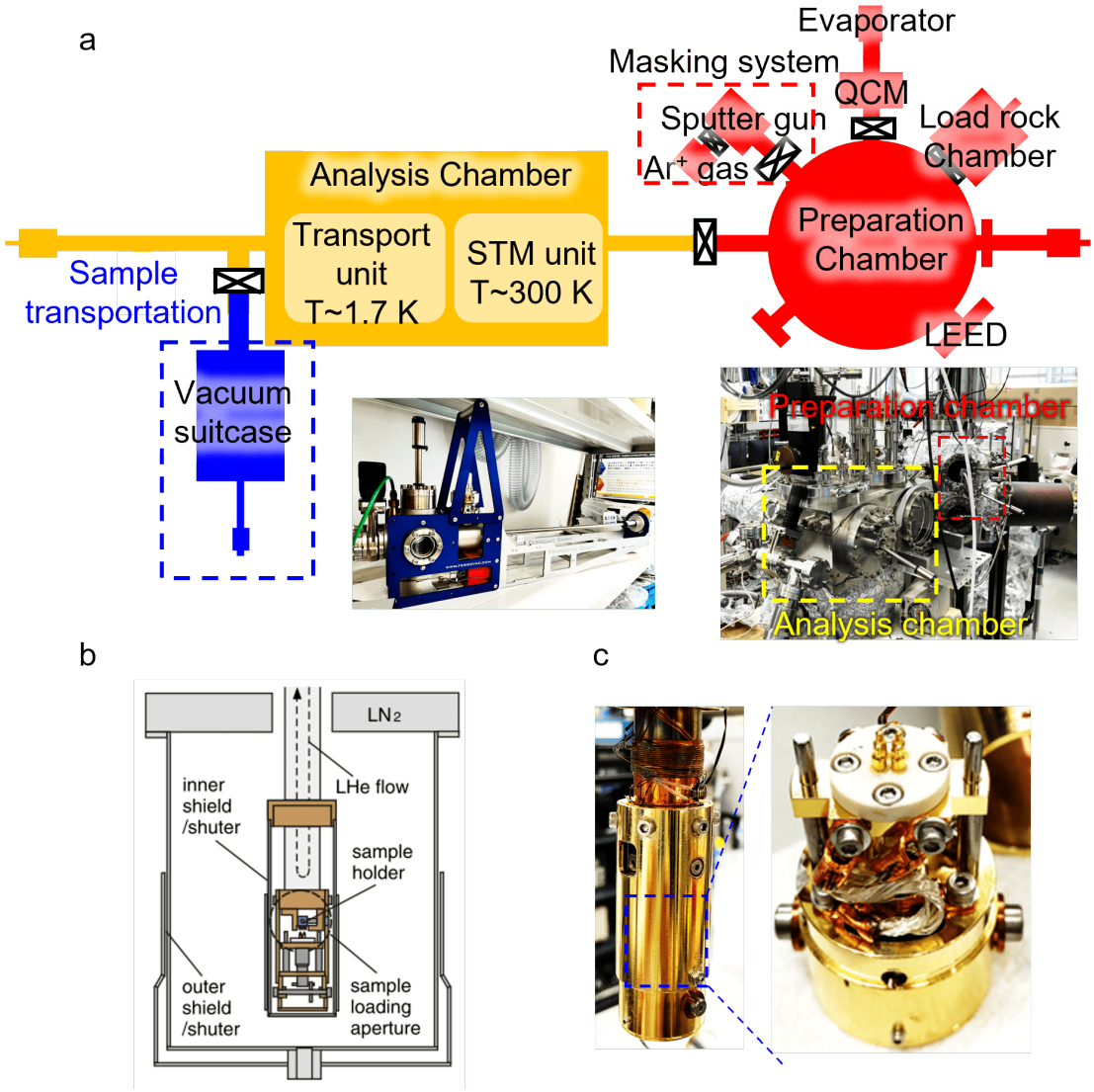

Figure 3.11 **Experimental setup of UHV-LT-transport measurement.** (a) Schematic diagram of the entire apparatus for UHV-LT-transport measurement. Samples can be transported to another device without breaking the UHV by using a vacuum suitcase in the blue frame. (b) Schematic illustration of the transport unit [25]. (c) Photograph of the spring probes for electrical contact.

3.7.2 UHV - LT - STM

In this study, we clarified thin film structures of organic molecules using LT-STM. Fig.3.12(a,b) shows a schematic diagram and photographs of the low-temperature STM apparatus used. This apparatus is based on the USM1200 manufactured by UNISOKU. The apparatus also consists of two preparation chambers ($< 7.0 \times 10^{-10}$ Torr) for sample preparation and an STM chamber ($< 7.0 \times 10^{-10}$ Torr). UHV is maintained in all chambers, and by directly transporting samples prepared and characterized in the preparation chamber to the STM chamber, "in-situ" observation at cryogenic temperatures is possible. The preparation chamber allows degassing of samples and probes introduced from outside the chamber, cleaning of Si substrates, and preparation of samples by metal or organic molecule deposition. Surface analysis is also possible with LEED equipment. STM measurements are possible at 78 K or 4.6 K by introducing liquid nitrogen or liquid helium into the cryostat containing the STM equipment. The Nanonis SPM controller from SPECS is used as a STM controller.

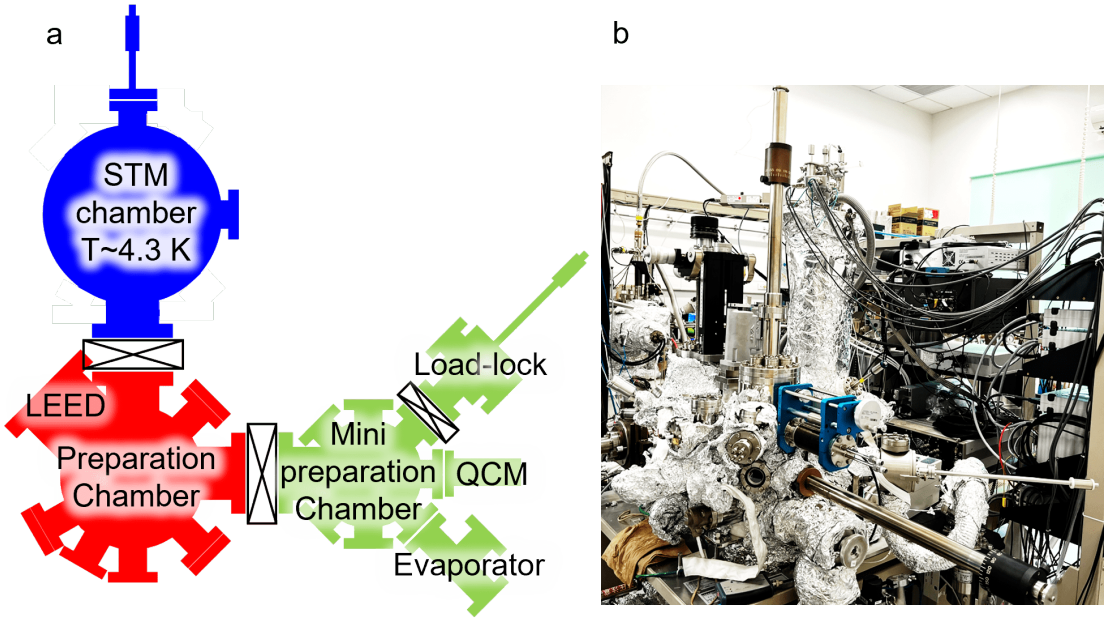

Figure 3.12 **Experimental setup of UHV-LT-STM.** (a) Schematic diagram of the entire apparatus for UHV-LT-STM. (b) Photograph of apparatus for UHV-LT-STM.

3.7.3 Molecular evaporator

A self-made molecular evaporator was used for the organic molecule deposition. Fig.3.13(a,b) show a schematic diagram and photographs of the molecular evaporator. A quartz crucible is used in the molecular evaporator. A tungsten (W) wire ($\phi = 0.3$ mm) is wound around the molecular crucible as a heating filament, and a DC current is applied to the W filament to heat and sublimate the molecules. The molecular deposition was performed in UHV ($< 4 \times 10^{-8}$ Pa), and the sample temperature was kept at room temperature during the deposition. The deposition amount was monitored using the quartz crystal microbalance method (QCM). QCM parameters were set to z ratio = 1, density = 1, tooling factor = 100 %. In molecular deposition using UHV-LT-Transport, we first measured the molecular deposited sample using RT-STM and accurately estimated the coverage from the obtained STM image. Next, by calibrating the coverage shown in the QCM with that estimated from the STM image, only the QCM was used in subsequent molecular deposition to deposit the desired amount.

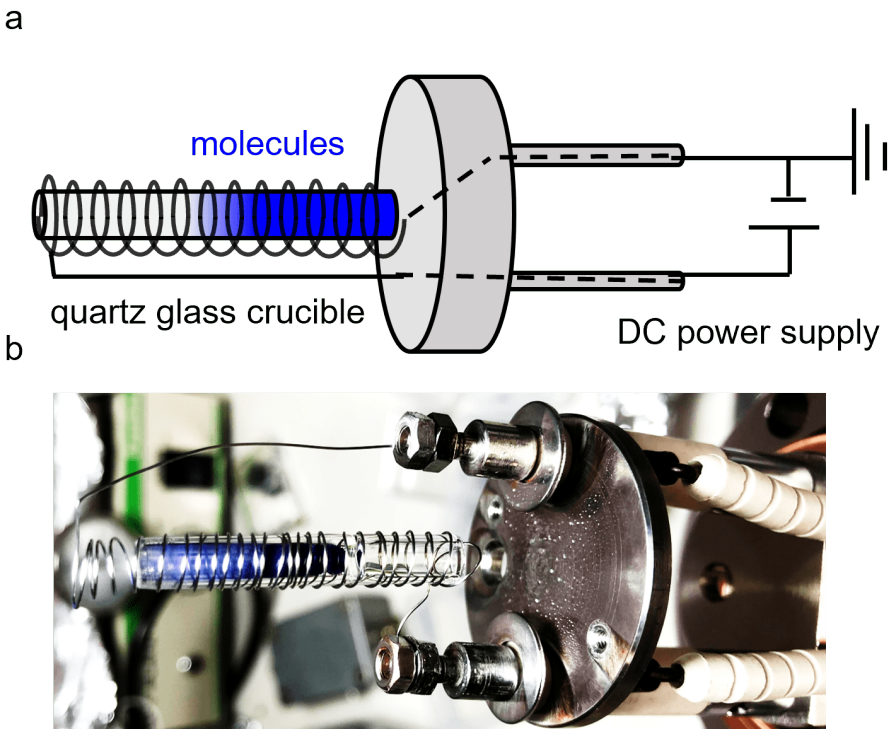

Figure 3.13 **Experimental setup of the molecular evaporator.** Schematic diagram (a) and photograph (b) of the molecular evaporator.

References

[1] 重川秀実 他,「走査プローブ顕微鏡」共立出版.

[2] Kazuhiro YOSHIHARA, 表面と真空. **61**, 9-14(2018).

[3] G. Binnig H. Rohrer, Ch. Gerber, and E. Weibel, Phys. Rev. Lett. **49**, 57-61(1982).

[4] G. Binnig, H. Rohrer, Ch. Gerber, and E. Weibel, Appl. Phys. Lett. **40**, 178-180 (1982).

[5] J. Bardeen, Phys. Rev. Lett. **6**, 57-59 (1961).

[6] J. Tersoff and D. Hamann, Phys. Rev. B. **31**, 805-813 (1985).

[7] N. D. Lang, Phys. Rev. B. **34**, 5947-5950 (1986).

[8] Vladimir A. Ukraintsev, Phys. Rev. B. **53**, 11176-11185 (1996).

[9] Jascha Repp and Gerhard Meyer, Phys. Rev. Lett. **94**, 026803 (2015).

[10] Shengyong Qin, Jungdae Kim, Qian Niu, Chih-Kang Shih, Science **324**, 1314-1317 (2009).

[11] Howon Kim, Shi-Zeng Lin, Matthias J. Graf, Yoshinori Miyata, Yuki Nagai, Takeo Kato, and Yukio Hasegawa, Phys. Rev. Lett. **117**, 116802 (2016).

[12] Shunsuke Yoshizawa, Howon Kim, Takuto Kawakami, Yuki Nagai, Tomonobu Nakayama, Xiao Hu, Yukio Hasegawa, and Takashi Uchihashi, Phys. Rev. Lett. **113**, 247004 (2014).

[13] Tong Zhang, Peng Cheng, Wen-Juan Li, Yu-Jie Sun, Guang Wang, Xie-Gang Zhu, Ke He, Lili Wang, Xucun Ma, Xi Chen, Yayu Wang, Ying Liu, Hai-Qing Lin, Jin-Feng Jia and Qi-Kun Xue, Nat. Phys. **6**, 104 (2010).

[14] T. Uchihashi, P. Mishra, M. Aono, and T. Nakayama, Phys. Rev. Lett. **107**, 207001 (2011).

[15] O. Kubo, Y. Shingaya, M. Nakaya, M. Aono, and T. Nakayama, Appl. Phys. Lett. **88**, 254101 (2006).

[16] Shinya Yoshimoto, Yuya Murata, Keisuke Kubo, Kazuhiro Tomita, Kenji Motoyoshi, Takehiko Kimura, Hiroyuki Okino, Rei Hobara, Iwao Matsuda, Shin-ichi Honda, Mitsuhiro Katayama, and Shuji Hasegawa, Nano Lett. **7**,956-959 (2007).

[17] C. Tegenkamp, Z. Kallassy, H. Pfnuï, H.-L. Guïter, V. Zielasek, and M. Henzler, Phys. Rev. Lett. **95**, 176804 (2005).

[18] K. Yoo and H.H. Weitering, Phys. Rev. Lett. **87**, 026802 (2001).

[19] Takashi Uchihashi, Puneet Mishra, Masakazu Aono, and Tomonobu Nakayama, Phys.

Rev. Lett. **107**, 207001 (2011).

[20] Takashi UCHIHASHI and Shunsuke YOSHIZAWA, 表面科学. **36**, 112-117 (2015).

[21] T. Uchihashi, P. Mishra, and T. Nakayama, Nanoscale Res. Lett. **8**, 167 (2013).

[22] P. Hohenberg and W. Kohn: Phys. Rev. **136**, B864-B871(1964).

[23] W. Kohn and L. J. Sham: Phys. Rev. **140**, A1133-A1138 (1965).

[24] 常田貴夫, 「密度汎関数法の基礎」講談社 (2012).

[25] Shunsuke Yoshizawa and Takashi Uchihashi, J. Phys. Soc. Jpn. **83**, 065001 (2014).

Chapter 4 Effect of ZnPc adsorption on atomic-layer superconductors

Since many of the references in Chapters 4 and 5 overlap, they are summarized at the end of Chapter 5.

4.1 Background

In this section, we first introduce $(\sqrt{7} \times \sqrt{3})$-In, the subject of this study, citing previous studies. Next, we summarize the correlation between the effect of organic molecules on $(\sqrt{7} \times \sqrt{3})$-In and its superconducting properties.

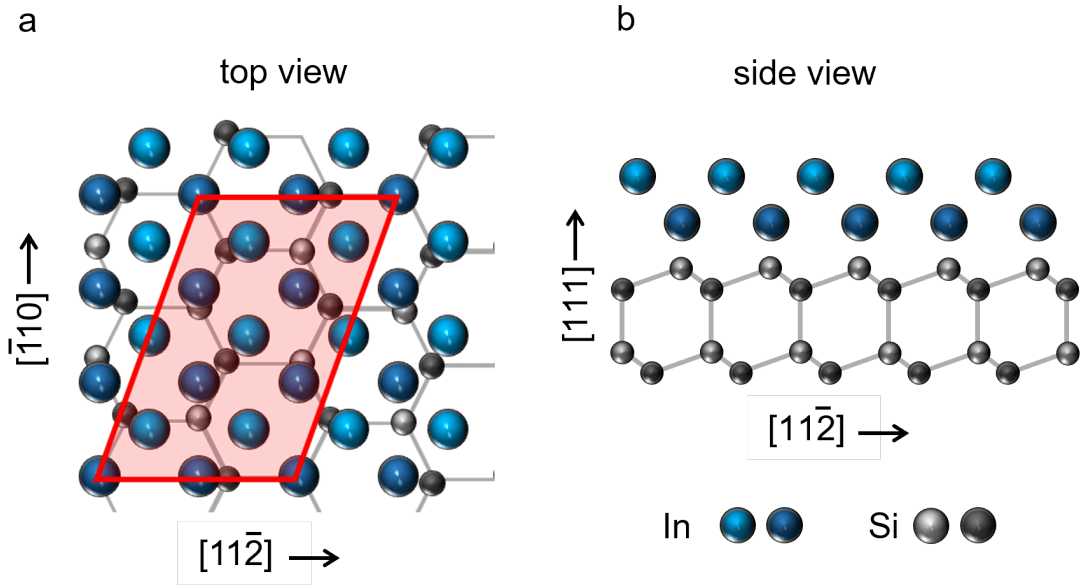

Figure 4.1 **Schematic illustrations of $(\sqrt{7} \times \sqrt{3})$-In atomic structure.** (a) Top view and (b) Side view images. The red frame in (a) represent $(\sqrt{7} \times \sqrt{3})$-In unit cell. The black arrows indicate [11$\bar{2}$], [1$\bar{1}$0] and [111] directions of the Si(111) substrate.

4.1.1 Atomic-layer superconductor $(\sqrt{7} \times \sqrt{3})$-In

$(\sqrt{7} \times \sqrt{3})$-In, a surface superstructure formed on a silicon substrate, can be regarded as an atomic-layer material in which bulk In is made as thin as possible. Fig.4.1 shows a structural model of $(\sqrt{7} \times \sqrt{3})$-In. $(\sqrt{7} \times \sqrt{3})$-In is considered to be two atomic-layers of balk In(001) planes grown on a Si substrate and deformed to maintain consistency. The unit cell has a long-period structure of $(\sqrt{7} \times \sqrt{3})$ for Si(111)-(1×1) (Fig.4.1(a), red box). The atomic arrangement structure of $(\sqrt{7} \times \sqrt{3})$-In has been well studied from both experimental and theoretical perspectives, and this structural model is widely accepted [1]-[3].

In general, surface superstructures exhibit physical properties that are very different from those of the corresponding bulk crystals. Many of them exhibit semiconductor or insulator-like electrical properties, depending on their structure [4, 5], even if composed of metal atoms. However, as shown in Fig.4.2(a)(b), $(\sqrt{7} \times \sqrt{3})$-In has a metallic band structure and a large Fermi surface [1, 6, 7]. The Fermi surfaces of $(\sqrt{7} \times \sqrt{3})$-In can be broadly classified into two types [8]. The blue line in Fig.4.2(c) is called a butterfly-like Fermi surface and is mainly composed of orbital hybridization between the In atomic-layer just above the Si surface and the topmost Si surface. The red Fermi surface in Fig.4.2(c) is called an arc-like Fermi surface, which originates from the atomic-layer of the topmost In surface and consists of a free electron-like circular Fermi surface that is folded back in the Brillouin zone. Both of the wave functions corresponding to these electrons decay sharply in the Si substrate and are only about an atomic-layer wide in the perpendicular

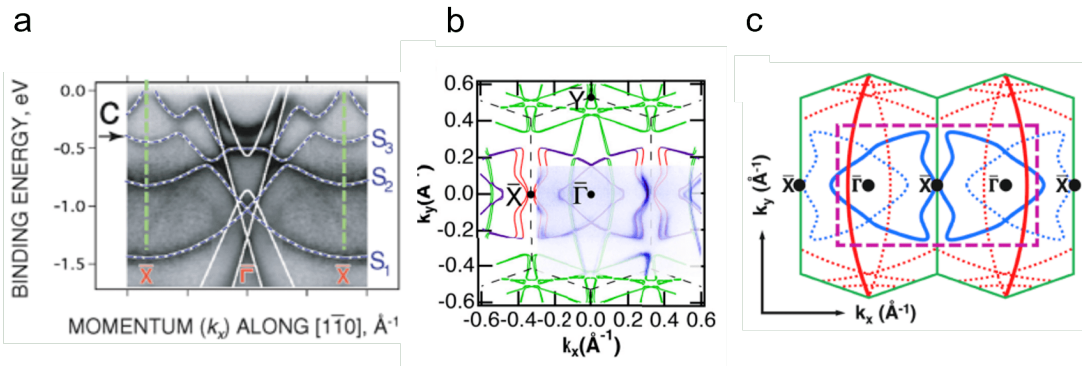

Figure 4.2 **Electronic state of $(\sqrt{7} \times \sqrt{3})$-In investigated by ARPES measurements.** (a) The band structure of $(\sqrt{7} \times \sqrt{3})$-In [6]. (b) The Fermi Surface of $(\sqrt{7} \times \sqrt{3})$-In [7]. The blue line indicates the experimental data. The other color lines indicate the theoretical calculation results. The Brillouin zone is indicated by black broken lines. (c) The schematic illustration of the Fermi Surface of $(\sqrt{7} \times \sqrt{3})$-In [8].

direction. In other words, this system forms an ideal two-dimensional electronic state at the surface.

Recently, it was discovered that $(\sqrt{7} \times \sqrt{3})$-In undergoes a superconducting transition upon cooling down to low temperatures. The observation of a superconducting gap in $(\sqrt{7} \times \sqrt{3})$-In was reported by Zhang et al [9]. Fig.4.3(a) shows the dI/dV spectra performed by STS with a superconducting probe. A peak structure characteristic of a superconductor-superconductor (S-S) junction is observed, confirming the existence of a superconducting energy gap and coherence peak near the Fermi level. The superconducting gap shape suggests that $(\sqrt{7} \times \sqrt{3})$-In is an s-wave superconductor with isotropic attractive interaction between electrons [9, 10]. The temperature dependence of the superconducting gap shown in Fig.4.3(b) follows the BCS theory. Thus, the superconducting gap measurement by STM can reveal the local electronic state of the superconductor. On the other hand, even though the existence of a superconducting gap implies the formation of Cooper pairs in local space, it does not necessarily mean that the Cooper pairs form ordered states on a wide spatial scale. In 2011, transport measurements of $(\sqrt{7} \times \sqrt{3})$-In

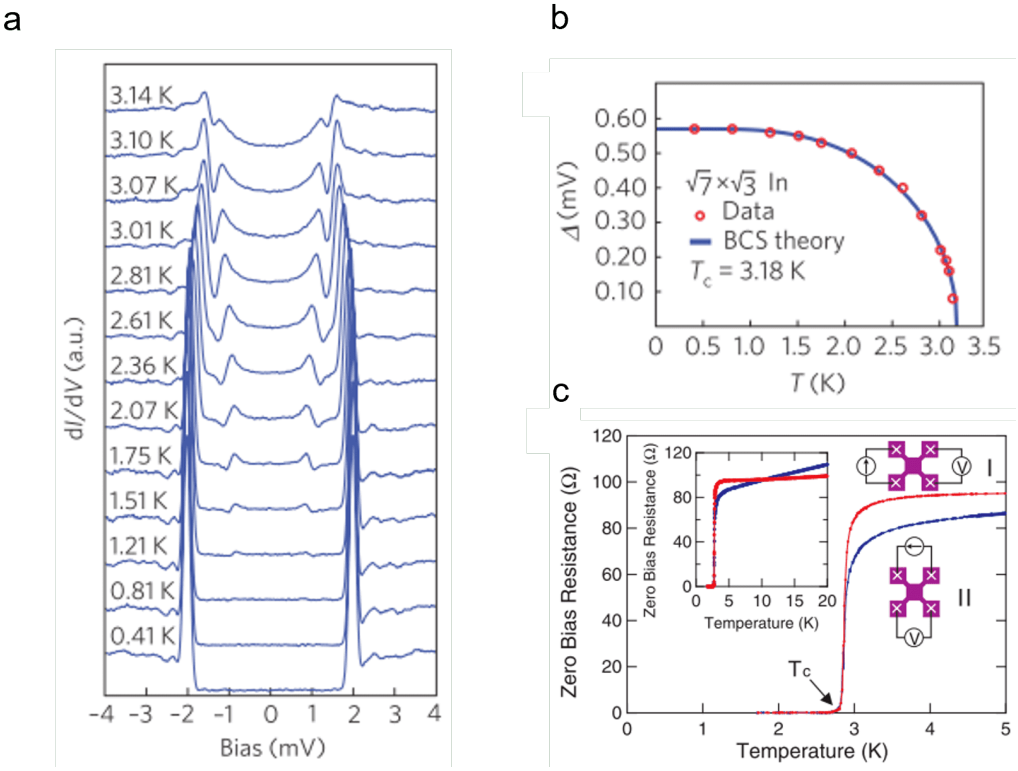

Figure 4.3 **Electrical properties of $(\sqrt{7} \times \sqrt{3})$-In investigated by STM and transport measurements.** (a) dI/dV spectras of $(\sqrt{7} \times \sqrt{3})$-In [9]. (b) Temperature dependence of superconducting gap [9]. (c) Temperature dependence of resistance indicating superconducting transition [11].

by Uchihashi et al. confirmed a phase transition to a zero-resistance state, indicating that a coherent superconducting state can be realized even in atomic-layer materials [11].

The T_c of $(\sqrt{7}\times\sqrt{3})$-In has been confirmed to be approximately 3 K [9],[11]-[14]. In general, T_c is expected to be much lower in two-dimensional systems than in three-dimensional systems due to localization and fluctuation effects caused by defects, but this transition temperature is almost the same as that of bulk In, which is 3.4 K. This is due to the fact that $(\sqrt{7}\times\sqrt{3})$-In has very high crystallinity with little disorder, in addition to being an atomic-layer material that is an extension of bulk In. As for other superconducting properties, the magnetic field response of the sheet resistance of $(\sqrt{7}\times\sqrt{3})$-In was measured by Yamada et al. and the GL coherence length $\xi_{GL}(0)$ was reported to be 25 nm [12]. The $\xi_{GL}\sim 47$ nm is also estimated from the vortex observation by Yoshizawa et al. On the other hand, since the effective in-plane magnetic field penetration length $\lambda_\perp$ of a two-dimensional superconductor of thickness d is given by $\lambda_\perp \approx \lambda^2/d$, the magnetic field penetration length $\lambda_\perp$ of $(\sqrt{7}\times\sqrt{3})$-In is estimated to be 4.4 mm [10, 11]. Therefore, from $\xi_{GL}(0) << \lambda_\perp$, $(\sqrt{7}\times\sqrt{3})$-In behaves as a type-Ⅱ superconductor.

So far, we have presented various physical properties of $(\sqrt{7}\times\sqrt{3})$-In. In summary, $(\sqrt{7}\times\sqrt{3})$-In is an atomic-layer superconductor with a well-defined atomic arrangement and a two-dimensional Fermi surface. In the superconducting state, it behaves as a type-Ⅱ s-wave superconductor according to BCS theory. This is convenient for studying the characteristics of atomic-layer superconductors. There are unconventional superconductors, such as cuprate ones, but the mechanism of superconductivity in these materials remains to be elucidated. However, $(\sqrt{7}\times\sqrt{3})$-In allows us to consider its properties both theoretically and experimentally within the framework of BCS theory. In addition, its well-known atomic structure and electronic structure allow for quantitative analysis. Thus, $(\sqrt{7}\times\sqrt{3})$-In is a useful platform for studying the general properties of atomic-layer superconductors.

4.1.2 T_c change of $(\sqrt{7}\times\sqrt{3})$-In by organic molecule adsorption

In general, atomic-layer superconductors are sensitive to surface and interface properties. This property can be used to change the superconducting state. In bilayer graphene and layered materials, superconducting transition and modulation of T_c can be induced by carrier doping through intercalation of alkali metals or application of gate voltage [15]-[17]. However, in the case of metal atomic-layer materials formed on the substrate surface, such a technique is not applicable because the deposited metal and gate electrodes destroy the atomic-layer material structure itself. However, organic molecules can be adsorbed without destroying the atomic-layer material because they interact with the metal surface only weakly, such as by van der Waals forces. This allows carriers to be doped from organic

molecules to the atomic-layer materials.

Yoshizawa et al. fabricated a metal phthalocyanine-$\left(\sqrt{7}\times\sqrt{3}\right)$-In heterostructure as shown in Fig.4.4(a) and reported that the T_c changes depending on metal-phthalocyanine (MPc) coverage [18]. Fig.4.4(b) shows the results of CuPc adsorption; it can be seen that the T_c of $\left(\sqrt{7}\times\sqrt{3}\right)$-In increases as the amount of CuPc adsorption is increased. This increase reaches a maximum at 0.8 ML, while above 1.2 ML, the T_c decreases with the coverage, indicating charge transfer between the CuPc film and $\left(\sqrt{7}\times\sqrt{3}\right)$-In, corresponding to hole doping from CuPc to $\left(\sqrt{7}\times\sqrt{3}\right)$-In. Yoshizawa et al. claimed that the origin of the T_c increase is due to charge transfer effects within the framework of BCS theory. In addition, Sagehashi et al. reported that the increase and decrease in T_c caused by CuPc

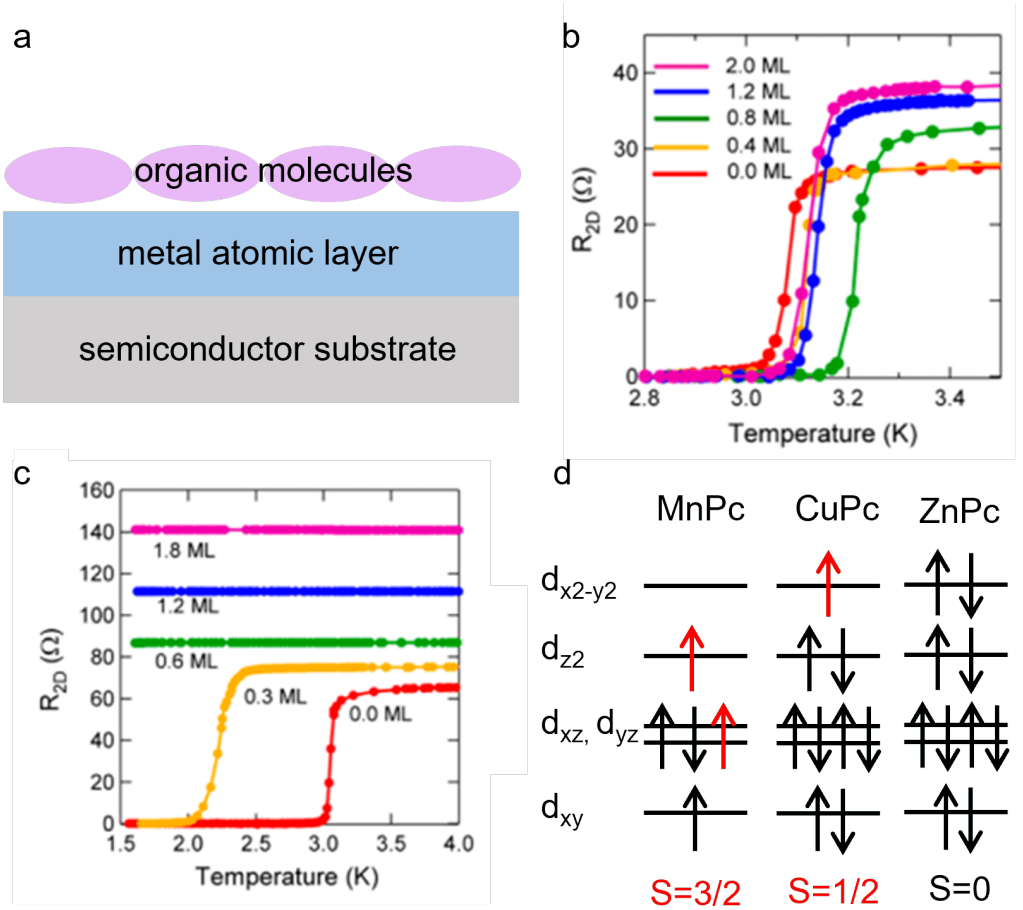

Figure 4.4 **Electrical properties of $\left(\sqrt{7}\times\sqrt{3}\right)$-In and organic molecular film heterostructures.** (a) Schematic diagram of atomic-layer superconductor and organic molecular layer grown on a semiconductor substrate. (b) Temperature dependences of the $\left(\sqrt{7}\times\sqrt{3}\right)$-In resistance modified by CuPc adsorption [18]. (c) Temperature dependences of the $\left(\sqrt{7}\times\sqrt{3}\right)$-In resistance modified by MnPc adsorption [18]. (d) Electron and spin states of the coordinated metal ions of MnPc, CuPc and ZnPc in an isolated system.

adsorption correspond well with the amount of charge transfer estimated from ARPES measurements [8].

On the other hand, when MnPc is adsorbed on $(\sqrt{7} \times \sqrt{3})$-In, T_c decreases and eventually superconductivity is completely suppressed (Fig.4.4(c)). This is believed to be caused by the exchange interaction between the spin magnetic moment of MnPc and the conduction electrons of $(\sqrt{7} \times \sqrt{3})$-In. The suppression of superconductivity due to the exchange interaction has also been observed in FePc thin film-$(\sqrt{7} \times \sqrt{3})$-In heterostructure [19, 20].

From the discussion so far, it seems that to increase the T_c of the $(\sqrt{7} \times \sqrt{3})$-In superconductor, we should deposit an organic molecule that does not have a spin magnetic moment and has a large hole doping. We note here that CuPc also has a spin magnetic moment. Fig.4.4(d) shows the spin states of the d orbitals of the central metal ions of MnPc, CuPc, and ZnPc in isolation; the spin states of MnPc and CuPc are S = 3/2 and 1/2, respectively. This means that if CuPc is adsorbed, T_c may be lowered by the spin magnetic moment. However, the spin magnetic moment of MnPc is perpendicular to the surface, while that of CuPc is horizontal to the surface. Therefore, as shown in Fig.4.5(a), the spin magnetic moment of CuPc adsorbed horizontally to the surface does not affect $(\sqrt{7} \times \sqrt{3})$-In just below the organic molecular thin film, and superconductivity is suppressed only for MnPc adsorption. Intriguingly, T_c was found to decrease in the case of F_{16}CuPc, which is expected to have a stronger acceptor property than CuPc and a large amount of charge transfer. This can be attributed to the adsorption structure of the organic molecules and the orientation of the spin magnetic moment: in the case of F_{16}CuPc, the spin magnetic moment is oriented horizontally, but as shown in Fig.4.5(b), the adsorption is tilted rather than horizontal to the surface. Therefore, it is possible that finite exchange interactions are at work and T_c is reduced. In other words, the adsorption structure of the molecule also has a significant effect on the change in T_c.

Thus, previous studies suggest that "charge transfer effect," "spin magnetic moment,"

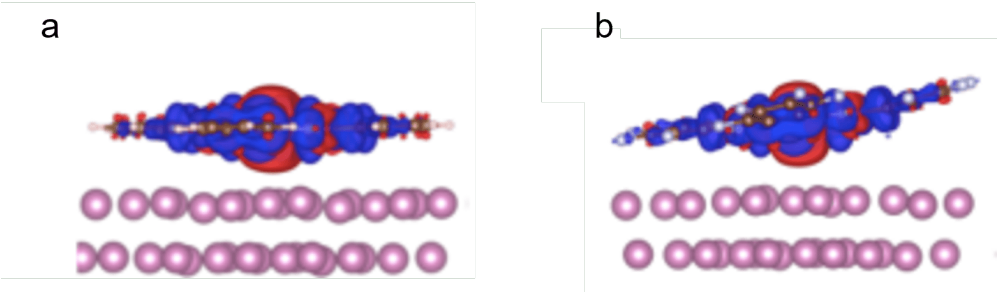

Figure 4.5 **Schematic diagram of (a) CuPc and (b)** F_{16}CuPc **adsorption structures on** $(\sqrt{7} \times \sqrt{3})$**-In [20].**

and "adsorption structure" contribute to the change in T_c. Among them, the suppression of superconductivity by spin magnetic moment has been reported for MnPc and FePc, and the experimental results can be explained by the spin states obtained by theoretical calculations. On the other hand, the T_c increase by the charge transfer effect (hole doping) of organic molecules has been reported only for CuPc. In F_{16}CuPc, which was expected to have a greater effect, on the contrary, T_c decreased. Although this can be explained by the difference in the adsorption structure, an accurate understanding has not been obtained. Therefore, it is not clear whether the origin of the T_c increase can really be attributed to charge transfer effects.

4.1.3 The purpose of this study

As mentioned in subsection 4.1.2, the T_c increase in the organic molecule-$\left(\sqrt{7}\times\sqrt{3}\right)$-In heterostructure was only observed when CuPc was adsorbed, and it is not clear whether hole doping is the origin of T_c increase. Therefore, the purpose of this study is to clarify the correlation between the change in T_c and the amount of charge transfer. As an organic molecule to be adsorbed, we employed zinc phthalocyanine (ZnPc), which is the same type of MPc and is expected to be free from spin effects (Fig.4.4(d))[21]-[23]. As shown in Fig.4.6, the adsorption structure of ZnPc is expected to be the same as that of CuPc, FePc, and MnPc since the central metal is only replaced by Zn. Therefore, there is no need to consider the difference in T_c change due to the adsorption structure. In other words, we can focus only on the charge transfer effect without considering the effects of spin magnetic moment and adsorption structure. Specifically, by comparing the amount of charge transfer and T_c change between the ZnPc adsorption system and the CuPc adsorption system, the correlation between the two can be investigated.

In this study, we investigate the effect of ZnPc on $\left(\sqrt{7}\times\sqrt{3}\right)$-In atomic-layer superconductors by using the following experimental and theoretical methods: The adsorption

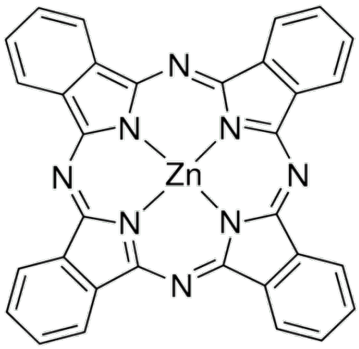

Figure 4.6 **Molecular structure of ZnPc [24].**

structure of ZnPc was investigated by STM measurements; the effect of ZnPc on the charge transfer and electronic structure was evaluated using ARPES measurements; the charge transfer effect and the presence of spin magnetic moment of ZnPc after adsorption were investigated by *ab initio* calculations based on DFT. The density of states near the Fermi level of $\left(\sqrt{7}\times\sqrt{3}\right)$-In was also determined by *ab initio* calculations. Transport measurements were made to measure the change of T_c with respect to the molecular coverage. We compare the "adsorption structure", "charge transfer", "spin magnetic moment", and "Amount of change in T_c" obtained from these methods with previous studies and comprehensively discuss the origin of the T_c increase.

4.2 Sample preparation

In this study, three types of Si wafers with different doping levels were used for each experiment. Non-doped Si wafers (resistivity $\rho > 1000$ Ωm) were used in the transport measurements to eliminate the influence of the substrate. By using non-doped Si, the current does not flow in the Si substrate in the temperature range below about 30 K, and we can focus only on the conduction characteristics of $\left(\sqrt{7}\times\sqrt{3}\right)$-In. On the other hand, LT-STM and ARPES measurements used N-doped Si wafers with $\rho < 0.01$ Ωcm and $\rho = 1-5$ Ωcm, respectively.

In order to obtain a clean surface of Si(111), the Si substrate was flashed several times at 1250 °C under a UHV environment. Fig.4.7(a) and Fig.4.7(b) show the results of cleaning the non-doped Si(111) used in the transport measurements. From both the LEED spots in Fig.4.7(a) and the STM image in Fig.4.7(b), the 7×7 structure, which is the characteristic structure of the Si(111) clean surface, can be confirmed. Furthermore, In was deposited on the cleaned Si(111) surface and annealed at about 300 °C for 10 seconds to fabricate a $\left(\sqrt{7}\times\sqrt{3}\right)$-In structure. Fig.4.7(c) shows the LEED measurement results. A 1×1 period derived from Si(111) and a $\left(\sqrt{7}\times\sqrt{3}\right)$ period due to the In atomic-layer can be confirmed (yellow frame). In addition, the RT-STM measurement results are shown in Fig.4.7 (d). A $\left(\sqrt{7}\times\sqrt{3}\right)$-In surface with few defects was confirmed. In the transport experiments, $\left(\sqrt{7}\times\sqrt{3}\right)$-In, which has domains in three directions and has few defects on the entire surface, was prepared and used.

ZnPc with a purity of $>$ 98 % was adopted as the adsorbate and deposited onto the sample from the crucible by a resistive heating method (see subsection 3.7.4). The ZnPc coverage for transport measurements was estimated using STM measurements. Also, the ZnPc coverage of the samples used in ARPES was estimated using QCM. One monolayer (ML) was defined as the coverage of one molecular film. All processes from sample preparation to RT-STM and LEED were performed in a UHV environment.

4.3 ZnPc molecular film structure on $(\sqrt{7} \times \sqrt{3})$-In surface

First, LT-STM was used to study the ZnPc adsorption structure on the $(\sqrt{7} \times \sqrt{3})$-In surface. The sample temperature during the measurement was 4.6 K, and a PtIr-tip was used. Fig.4.8(a) shows an STM image of the pristine $(\sqrt{7} \times \sqrt{3})$-In surface. A surface structure corresponding to the $(\sqrt{7} \times \sqrt{3})$ period can be confirmed. The blue frame indicates the unit cell of $(\sqrt{7} \times \sqrt{3})$-In. Black arrows indicate the $[11\bar{2}]$ and $[\bar{1}10]$ directions

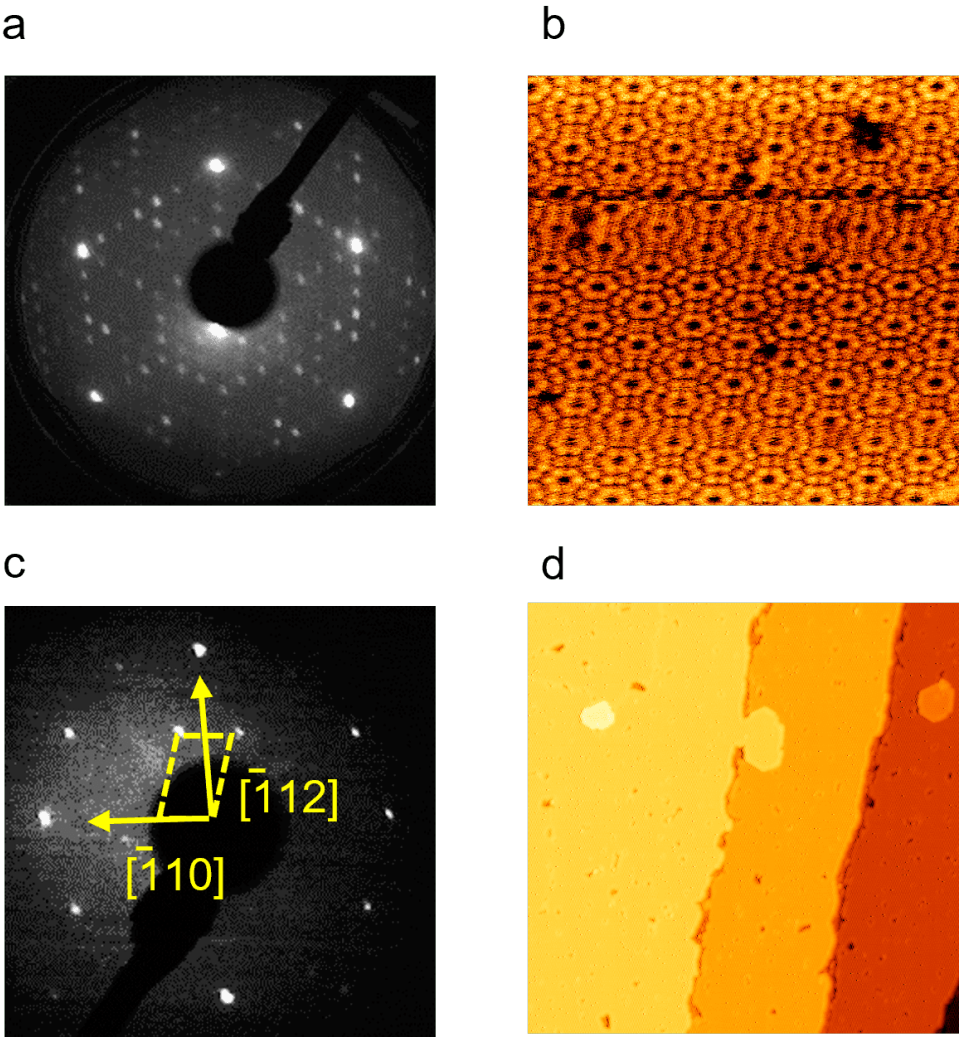

Figure 4.7 **Sample preparations for transport measurements.** (a) LEED pattern (50 eV) at RT and (b) STM image (image size: 20×20 nm^2, sample voltage: $V_s = -1.5$ V, tunnel current: $I_t = 300$ pA.) at RT of Si(111)-7×7. (c) LEED pattern (90 eV) at RT and (d) STM image (image size: 200×200 nm^2, sample voltage: $V_s = -1.5$ V, tunnel current: $I_t = 300$ pA.) at RT of $(\sqrt{7} \times \sqrt{3})$-In.

of the lattice vectors of the Si(111) substrate, obtained from atomic images of $(\sqrt{7} \times \sqrt{3})$-In [25]. Next, 0.5 ML of ZnPc was deposited and STM measurement was performed. Fig.4.8(b) shows the STM image of the ZnPc molecular film grown on the $(\sqrt{7} \times \sqrt{3})$-In surface. The ZnPc films are regularly arranged in a square lattice. When the sample was prepared again and the ZnPc coverage was further increased, the $(\sqrt{7} \times \sqrt{3})$-In surface was completely covered with one layer, as shown in the inset of Fig.4.8(b). Fig.4.8(c) shows an STM image with molecular resolution. Lattice vectors $[11\bar{2}]$ and $[\bar{1}10]$ are rotated by 60° from Fig.4.8(a) due to the domain difference. The square lattice of ZnPc was found to have a unit cell size of 1.4×1.4 nm^2 and to grow with the lattice vector rotated 45° parallel to the $[11\bar{2}]$ direction.

This structure is identical to those of previously reported MPc molecular films (M = Cu, Mn, Fe) grown on $(\sqrt{7} \times \sqrt{3})$-In [18, 19]. Therefore, it can be seen that the ZnPc molecular film is epitaxially grown as a result of the ZnPc unit cell matching well with the period of the $(\sqrt{7} \times \sqrt{3})$-In surface. However, although they have the same adsorption structure, the amount of charge transferred to the substrate surface is different in each system, which may lead to different T_c changes. Therefore, it is necessary to investigate the amount of charge transfer between ZnPc and $(\sqrt{7} \times \sqrt{3})$-In in detail.

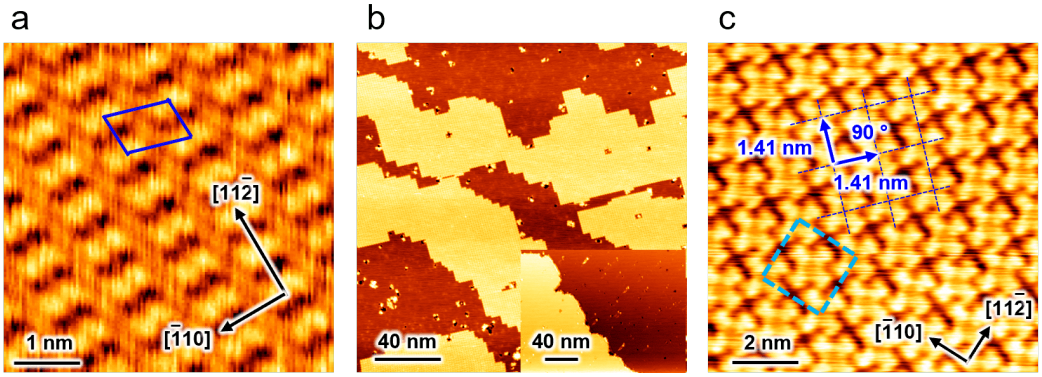

Figure 4.8 **ZnPc molecular film structure on $(\sqrt{7} \times \sqrt{3})$-In.** (a) STM image of the pristine $(\sqrt{7} \times \sqrt{3})$-In surface ($5 \times 5$ nm^2, $V_s = 0.5$ V, $I_t = 10$ pA.). The blue frame indicates the unit cell of $(\sqrt{7} \times \sqrt{3})$-In. Black arrows indicate the $[11\bar{2}]$ and $[\bar{1}10]$ directions of Si(111). (b)(c) STM image of ZnPc thin film grown on $(\sqrt{7} \times \sqrt{3})$-In. (b) ZnPc coverage 0.5 ML (200×200 nm^2, $V_s = -2.0$ V, $I_t = 10$ pA). Inset: ZnPc coverage 1.0 ML (200×150 nm^2, $V_s = -2.0$ V, $I_t = 10$ pA). (c) ZnPc thin film structure (10×10 nm^2, $V_s = -2.0$ V, $I_t = 10$ pA). The blue arrows indicate the unit vector, and the molecular lattice of ZnPc is rotated 45° from the $[11\bar{2}]$ direction. The cell size was 1.41×1.41 nm^2 and the angle was 90°.

4.4 Fermi surface change of $(\sqrt{7} \times \sqrt{3})$-In by ZnPc adsorption

To determine the amount of charge transfer by ZnPc, the Fermi surface change of $(\sqrt{7} \times \sqrt{3})$-In was investigated using ARPES. The ARPES measurements were carried out in collaboration with Sakamoto Laboratory at Osaka University. ARPES measurements were performed using laboratory-based equipment. All the measurements were conducted in a UHV environment ($< 10^{-8}$ Pa) and a sample is cooled down to 85 K. As the light source, p-polarized He-I synchrotron radiation ($h\nu = 21.2$ eV) was adopted. In addition, the energy resolution and wavenumber resolution of the hemispherical electrostatic analyzer in this ARPES measurements were set at 20 meV and 4×10^{-3}Å^{-1}.

First, we obtain a molecular orbital spectrum derived from ZnPc in order to confirm that ZnPc is adsorbed on $(\sqrt{7} \times \sqrt{3})$-In. For this purpose, SiO_2 was adopted as a substrate. The reason is that 1) the interaction is expected to be weak, and 2) since there is no state in the valence region, the molecular orbital spectrum of ZnPc can be confirmed without being buried in the spectrum derived from the substrate. The results are shown in Fig.4.9(a). In the molecular orbital spectrum of SiO_2 deposited with 1.2 ML of ZnPc, peaks attributed to ZnPc can be confirmed at approximately 1.8 eV, 4.0 eV, 7.5 eV, and 9.0 eV. Here, the coverage rate of 1.2 ± 0.4 ML indicates the coverage rate in case of depositing on $(\sqrt{7} \times \sqrt{3})$-In. Since the energy position of the molecular orbital spectrum

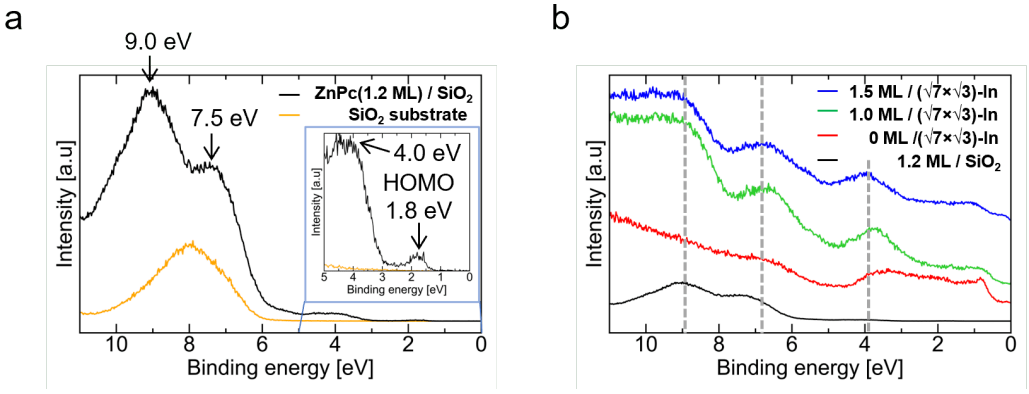

Figure 4.9 **PES measurements of ZnPc adsorption on SiO_2 substrate and $(\sqrt{7} \times \sqrt{3})$-In surface.** (a) Molecular orbital spectrums before (yellow line) and after (black line) ZnPc adsorption of 1.2 ± 0.4 ML. Black arrows indicate molecular orbitals of ZnPc. (b) Comparison of molecular orbital spectrums. Blue, green, and red lines show the molecular orbital spectrums of 0 ML, 1.0 ± 0.3 ML and 1.5 ± 0.5 ML of ZnPc deposited on $(\sqrt{7} \times \sqrt{3})$-In, respectively. The gray dashed line indicates the peak position derived from ZnPc.

peak derived from ZnPc was found, ZnPc was actually deposited on $(\sqrt{7} \times \sqrt{3})$-In and the molecular orbital spectrum was measured. As shown in Fig.4.9(b), molecular orbital spectra derived from ZnPc can be confirmed in both cases of 1.0 ± 0.3 ML and 1.5 ± 0.5 ML adsorption on $(\sqrt{7} \times \sqrt{3})$-In. Therefore, ARPES measurement also shows that ZnPc is adsorbed to $(\sqrt{7} \times \sqrt{3})$-In.

Then the Fermi surface was measured by ARPES. Fig.4.10(a) shows the result for the pristine $(\sqrt{7} \times \sqrt{3})$-In Fermi surface. The horizontal axis k_x and vertical axis k_y correspond to the $[\bar{1}10]$ and $[11\bar{2}]$ directions, respectively. The Fermi surfaces obtained in this experiment show good agreement with previous studies [6]-[8],[26, 27]. As mentioned in 4.1.1, the Fermi surface of $(\sqrt{7} \times \sqrt{3})$-In consists of two parts. One is an arc-like Fermi surface that can be confirmed between $k_x = -1.3$ Å^{-1} and $k_x = -1.4$ Å^{-1} in the left red frame. The second is a butterfly Fermi surface identified from $k_x = -1.0$ Å^{-1} to $k_x = -1.3$ Å^{-1}. The arc-like Fermi surface is attributed to the two-dimensional free-electron metal band [6, 7]. The structure confirmed in the $k_x > -0.98$ Å^{-1} region is the result of folding back of the Fermi surface in -1.4 Å^{-1} $< k_x < -0.98$ Å^{-1} at the Brillouin zone boundary. Next, the Fermi surface of $(\sqrt{7} \times \sqrt{3})$-In deposited with 1.0 ± 0.3 ML and 1.5 ± 0.5 ML of ZnPc was measured. The ARPES results are shown in Fig.4.10(b) and (c), respectively. The Fermi surface of $(\sqrt{7} \times \sqrt{3})$-In is maintained even after ZnPc adsorption. This result indicates that the structure of $(\sqrt{7} \times \sqrt{3})$-In is maintained even under the ZnPc molecular film. The Fermi surfaces of the pristine $(\sqrt{7} \times \sqrt{3})$-In and ZnPc-deposited $(\sqrt{7} \times \sqrt{3})$-In are not changed. This suggests that there is only a weak interaction such as a van der Waals force between ZnPc and $(\sqrt{7} \times \sqrt{3})$-In, not a strong interaction accompanied by orbital hybridization.

If $(\sqrt{7} \times \sqrt{3})$-In is doped with holes by ZnPc, the Fermi level shifts to lower energies, and as a result, the free-electron arc-like Fermi surface shrinks [8, 18]. Therefore, the size change of the arc-like Fermi surface before and after ZnPc adsorption was investigated. Fig.4.10(d) shows Momentum Distribution Curves (MDCs) measured along the white arrows in Fig.4.10(a), (b) and (c). The peak position error was estimated to be 0.007 Å^{-1} by Cauchy-Lorentz distribution function fitting. Fig.4.10(e) shows the MDCs in the yellow frame of Fig.4.10(d). The peak shift widths between the pristine and 1.0 ± 0.3 ML, 1.5 ± 0.5 ML were -0.0037 ± 0.007 Å^{-1} and $+0.00043 \pm 0.007$ Å^{-1}, respectively. That is, the sizes of the two Fermi surfaces are almost unchanged. Also, the k-space mapping of the arc-like Fermi surface in Fig.4.10(e) was plotted. This clearly indicates that the Fermi surface is not shifted by ZnPc adsorption, and that little charge is transferred from ZnPc to $(\sqrt{7} \times \sqrt{3})$-In. In contrast, the arc-like Fermi surface of $(\sqrt{7} \times \sqrt{3})$-In hole-doped by CuPc shrinks by up to 0.018 Å^{-1} in previous studies [8, 18].

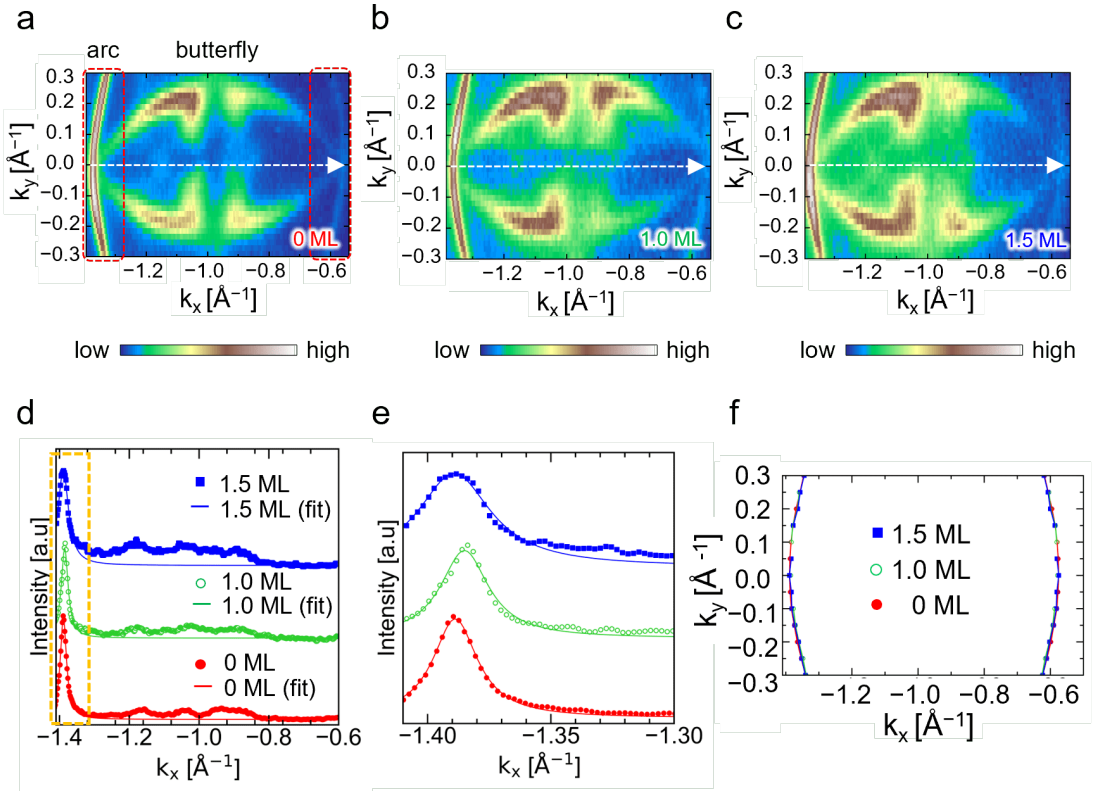

Figure 4.10 **ARPES measurements of $(\sqrt{7}\times\sqrt{3})$-In before and after adsorption of ZnPc molecules. Photoelectron mapping of the $(\sqrt{7}\times\sqrt{3})$-In Fermi surface in momentum space before.** (a) and after (b) adsorption of 1.0 ± 0.3 ML and after adsorption of 1.5 ± 0.5 ML ZnPc. The region encircled by the dashed red lines indicates an arc-like Fermi surface. (d) MDCs obtained along the white arrow (k_y = 0 Å^{-1}) in Fig.4.10(a-c) and peak positions of the arc-like Fermi surface of $(\sqrt{7}\times\sqrt{3})$-In (f) acquired for different ZnPc coverages. Solid red circles: 0 ML, open green circles: 1.0 ± 0.3 ML, solid blue squares: 1.5 ± 0.5 ML. (e) is the MDC inside the yellow dashed frame in Fig4.10(d).

4.5 Estimation of charge transfer amount by ZnPc adsorption

From the peak shift obtained by ARPES measurement, the amount of charge transfer can be estimated as follows. Since the radius of the Fermi surface of $(\sqrt{7}\times\sqrt{3})$-In is k_F = 1.417 Å^{-1}, the area of the Fermi surface is given by

$$S_F = \pi k_F^2 = 6.305 \text{ Å}^{-2} \tag{4.1}$$

In addition, in the arc-like Fermi surface which is the object of peak shift in ARPES measurement, the In layer of $(\sqrt{7}\times\sqrt{3})$-In can be approximated to the In(001) surface.

At this time, the area of the Brillouin zone of the In(001) unit cell is

$$S_{BZ} = \frac{2\pi}{a_x}\frac{2\pi}{a_y} = 3.707 \text{ Å}^{-2} \tag{4.2}$$

where $a_x = 3.200$ Å and $a_y = 3.325$ Å are given as lattice constants of $[\bar{1}10]$ and $[11\bar{2}]$. Therefore, the number n_{In} of conduction electrons per In atom is obtained as follows.

$$n_{In} = \frac{S_F}{S_{BZ}} = 1.700 \tag{4.3}$$

Assuming that the charge transfer reduces the Fermi radius by Δk_F, the number of conduction electrons n'_{In} per In atom after charge transfer is given by the following equation.

$$n'_{In} = \frac{\pi \left(k_F - \Delta k_F\right)^2}{S_{BZ}} \tag{4.4}$$

Therefore, the change in the number of conduction electrons per In atom due to charge transfer Δn_{In} is

$$\Delta n_{In} = n_{In} - n'_{In} = \frac{2\Delta k_F}{k_F} n_{In} \tag{4.5}$$

where the quadratic term in Δk_F has been neglected. Therefore, using the peak shift width $\Delta k_F = -0.0037 \pm 0.007$ Å^{-1} when 1.0 ML of ZnPc was deposited by ARPES measurement, $\Delta n_{In} = -0.0089 \pm 0.0168$ e. Furthermore, considering that the surface density ratio of Pc molecules and In atoms is 0.028 [18], the amount of charge transfer per molecule is $\Delta n_{mol} = -0.32 \pm 0.6$e. On the other hand, when 1 ML of CuPc is deposited, similar calculations using $\Delta k_F = -0.018 \pm 0.004$ Å^{-1} yield $\Delta n_{In} = -0.043 \pm 0.009$ e, $\Delta n_{mol} = -1.53 \pm 0.32$ e. Thus, it can be seen that the hole doping in the case of CuPc is clearly larger than that in the case of ZnPc.

4.6 Estimation of charge transfer and spin magnetic moment by the *ab initio* calculations

Using the *ab initio* calculations, the amount of charge transfer between ZnPc and $\left(\sqrt{7} \times \sqrt{3}\right)$-In and the magnitude of the molecular spin magnetic moment were evaluated. ZnPc has no spin in isolation. However, in general, organic molecules adsorbed on metal substrates change their electronic state in the isolated state by interactions with the substrate [28]. Therefore, ZnPc may also have a spin magnetic moment after adsorption. The *ab initio* calculations for ZnPc-adsorbed and CuPc-adsorbed $\left(\sqrt{7} \times \sqrt{3}\right)$-In were carried out as joint research by Minamitani Laboratory, Osaka University. Charge transfer and spin magnetic moment were calculated by the following method. DFT-based *ab initio* calculations were performed using the plane wave-based Vienna *ab initio* simulation package

(VASP) with the projected augmented wave (PAW) method [29, 30]. The $(\sqrt{7} \times \sqrt{3})$-In structure was obtained by optimizing a slab consisting of two In layers [1, 27] and hydrogen-terminated Si(111) 8 layers. The structural optimization was performed until the force acting between individual atoms was less than 0.02 eV/Å. The charge transfer between the ZnPc molecule and the $(\sqrt{7} \times \sqrt{3})$-In was estimated from the Bader analysis of the *ab initio* calculation results.

Fig.4.11 shows the differential charge distribution calculated by the *ab initio* calculations. Here, the differential charge distribution was defined as the difference between the charge density of the surface on which the molecule was adsorbed and the charge density of the original surface and the molecule. Fig.4.11(a) shows that electrons are accumulated in the interface region of ZnPc. Accumulated electrons are localized just below the central metal of ZnPc. Thus, finite charge transfer exists due to the adsorption of ZnPc in the *ab initio* calculations. The charge increase per ZnPc molecule was $\Delta n_{mol} = -0.76$ e. Fig.4.11(b) also shows the differential charge distribution when CuPc is adsorbed. As in the case of ZnPc, electrons are accumulated in the interfacial region just below the central metal of CuPc. The amount of charge transfer was $\Delta n_{mol} = -1.61$e. From the above results, it was found that the charge transfer amount by ZnPc was 47 % of that by CuPc in the *ab initio* calculations. Although this is quantitatively different from the ARPES result, it is qualitatively consistent in that the amount of charge transfer is clearly smaller in the case of ZnPc than in the case of CuPc.

The spin magnetic moment m_s of ZnPc after adsorption on $(\sqrt{7} \times \sqrt{3})$-In obtained

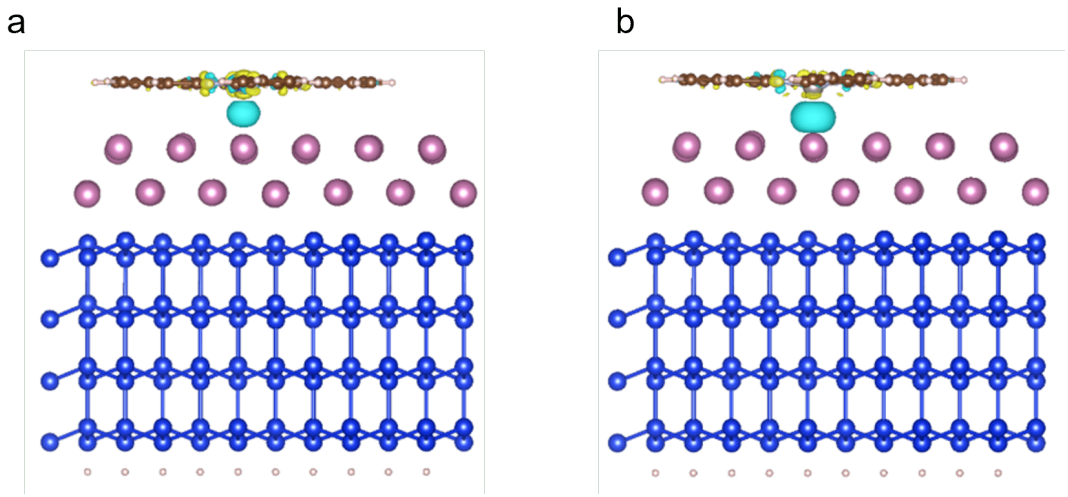

Figure 4.11 **Spatial distribution of difference charge (a) ZnPc and (b) CuPc adsorption on $(\sqrt{7} \times \sqrt{3})$-In surface.** The yellow and light-blue colors correspond to positive and negative charges, respectively. The isosurface value is 0.01 e/Bohr^3 for two cases.

by the *ab initio* calculations was 0.00 μ_B (μ_B : Bohr magneton). That is, ZnPc does not have a spin magnetic moment even after adsorption. On the other hand, the spin magnetic moment after adsorption of CuPc was found to be $m_s = 0.29\ \mu_B$ from a previous study [26]. However, as described in subsection 4.1.2, since the magnetic moment m associated with the In atomic-layer is $m = 0.00\ \mu_B$, exchange interaction doesn't work between the conduction electrons of $\left(\sqrt{7} \times \sqrt{3}\right)$-In and the spins of CuPc. In other words, it is not necessary to consider the effect of spin on superconductivity when either ZnPc or CuPc is adsorbed.

Summarizing the results of ARPES and the *ab initio* calculations, the amount of charge transfer from ZnPc is smaller than that from CuPc. Therefore, if the increase in T_c due to CuPc adsorption is due to hole doping, the increase in T_c due to ZnPc adsorption is expected to be smaller than that of CuPc. Moreover, considering that there is no suppression of superconductivity by spin, it is expected that T_c will hardly change.

4.7 T_c change due to ZnPc adsorption

Transport measurements were performed to clarify the effect of ZnPc adsorption on T_c. A shadow mask was used for the electrode preparation of the sample. The unmasked In layer surface was sputtered with an Ar^+ beam (E = 200 eV) to limit the current area through the sample (see subsection 3.4.2). A gold-coated spring probe for four-terminal measurement was pressed against the electrode area of the sample, and the resistance temperature dependence of the sample was measured while cooling to 1.7 K by liquid helium pumping. First, transport measurements were performed on the pristine $\left(\sqrt{7} \times \sqrt{3}\right)$-In, then ZnPc was sub-ML deposited and measured again. This cycle was repeated until the coverage $\theta = 1.5$ ML.

Fig.4.12(a) plots the sheet resistance temperature dependence of the sample for each ZnPc coverage. The pristine $\left(\sqrt{7} \times \sqrt{3}\right)$-In (red line) showed a sharp decrease in resistance at low temperatures. This indicates a superconducting transition and T_c of this sample was determined to be 2.81 K by fitting with a theoretical formula that incorporates fluctuations in two-dimensional superconductivity. As the coverage of ZnPc was increased, T_c tended to increase until the coverage $\theta < 1.0$ ML. T_c increased up to 3.13 K at coverage $\theta = 1.0$ ML (blue line). On the other hand, when the coverage $\theta = 1.5$ ML (light blue line), T_c decreased ($T_c = 3.10$ K) compared to that in the case of coverage $\theta = 1.0$ ML. In addition, in the case of the pristine $\left(\sqrt{7} \times \sqrt{3}\right)$-In, the resistance abruptly approaches 0 Ω, whereas the resistance change becomes broad at the coverage $\theta = 0.6$ ML or more. This suggests that ZnPc adsorption made T_c spatially non-uniform, but the detailed cause is unknown. Here T_c is close to the maximum value determined by fitting Eq.3.20 (see subsection 3.4.3) and considered.

Fig.4.12(b) plots the change in T_c of $(\sqrt{7} \times \sqrt{3})$-In depending on the coverage of ZnPc. Data for CnPc were also plotted for comparison [18]. Here, $\Delta T_c = T_c(\theta) - T_c(\theta = 0)$ is defined. The behaviors of ΔT_c of ZnPc and CuPc are similar in that they tend to increase up to a coverage $\theta = 1$ ML, and that ΔT_c tends to decrease above 1 ML. Nevertheless, the adsorption of ZnPc clearly increased T_c more than the case of CuPc. The maximum T_c increase was 0.32 K in ZnPc adsorption. This corresponds to 11 % of T_c for $(\sqrt{7} \times \sqrt{3})$-In. Also, this is 2.7 times greater than the maximum T_c increase of 0.12 K for CuPc. Unexpectedly, T_c of $(\sqrt{7} \times \sqrt{3})$-In was increased by ZnPc adsorption, although the charge transfer effect was almost non-existent. Table 4.1 summarizes the increase in T_c and the amount of charge transfer due to ZnPc obtained in this study and CuPc obtained in previous studies. As is clear from Table 4.1, the change in T_c does not match the behavior expected from the amount of charge transfer (hole doping). In other words, it was clarified that the origin of the T_c increase was not the charge transfer effect.

4.8 Discussion

To clarify the origin of T_c enhancement, this section discusses three things: 1) the effect of hole doping on $(\sqrt{7} \times \sqrt{3})$-In, 2) correlation between ΔT_c and the amount of hole doping in CuPc and ZnPc, 3) mechanism of T_c increase in $(\sqrt{7} \times \sqrt{3})$-In by ZnPc and CuPc adsorption.

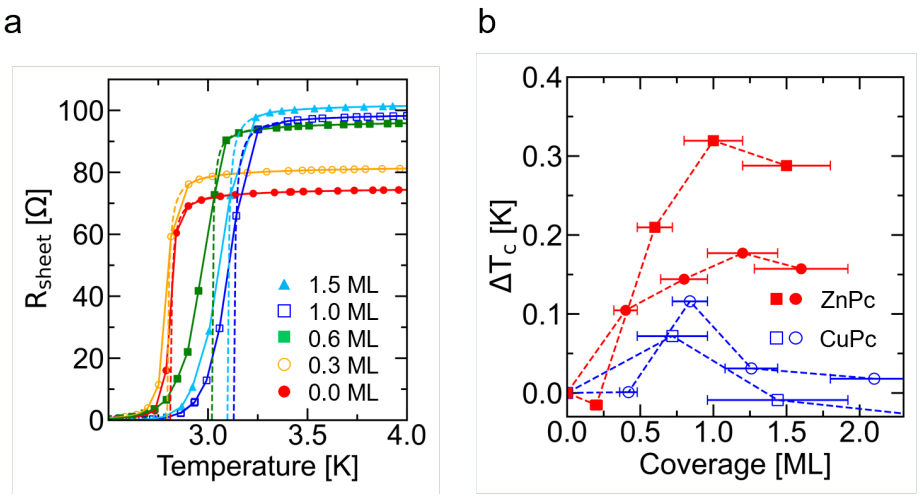

Figure 4.12 **Transport measurements of $(\sqrt{7} \times \sqrt{3})$-In before and after adsorption of ZnPc molecules.** (a) Temperature dependences of the sheet resistance of $(\sqrt{7} \times \sqrt{3})$-In acquired for different coverages of ZnPc. The dashed lines are the fits to thermal fluctuation theories of 2D superconductivity. (b) Variation of ΔT_c as a function of ZnPc coverage (solid red circles/squares). The result of the previous experiment using CuPc [18] is also plotted (open blue circles/squares).

Table 4.1 **List of the maximal changes in T_c (ΔT_c) and charge transfers(Δn_{mol}) induced by ZnPc and CuPc molecules.** The negative sign of Δn_{mol} corresponds to electron transfer from the In layers to the molecule.

physical quantity	method	ZnPc	CuPc
ΔT_c [K]	transport	0.32	0.12
Δn_{mol} [e]	ARPES	-0.31 ± 0.59	-1.51 ± 0.32
Δn_{mol} [e]	*ab initio* calc.	-0.76	-1.61

First, the effect of hole doping on $\left(\sqrt{7} \times \sqrt{3}\right)$-In is investigated. From BCS theory, T_c is expressed by the following equation [31].

$$T_c = 1.13 \frac{\hbar \omega_c}{k_B} \exp\left(-\frac{1}{N\left(E_F\right) V}\right) \tag{4.6}$$

where ω_c is the Debye frequency of phonons, $N(E_F)$ is the density of states per unit volume at the Fermi level, and V is the attractive potential between electrons. From Eq.4.6, if hole doping increases $N(E_F)$ of $\left(\sqrt{7} \times \sqrt{3}\right)$-In, the origin of the T_c increase should be the charge transfer effect. According to the energy dependence of the density of states of $\left(\sqrt{7} \times \sqrt{3}\right)$-In calculated by Park et al., hole doping reduces the density of states [1, 2]. However, the degree of contribution of each orbital of $\left(\sqrt{7} \times \sqrt{3}\right)$-In to superconductivity is unknown. Therefore, the projected density of states (PDOS) of each orbital in each layer of $\left(\sqrt{7} \times \sqrt{3}\right)$-In were calculated. The calculation conditions are as follows. The Quantum ESPRESSO package was used for DFT calculations [32]. The extended plane wave method was adopted, and the local density approximation (LDA) was used for the exchange-correlation function. The structure of $\left(\sqrt{7} \times \sqrt{3}\right)$-In was modeled by repeating slabs consisting of two In layers, a hydrogen-terminated Si(111) 6 layer, and a 3 nm-thick vacuum region. The cut-off energy of the wavefunction is 680 eV, and a $6 \times 8 \times 1$ k-point mesh is used for the Brillouin zone. The structure was optimized so that all forces on individual atoms were less than 2.6×10^{-3} eV/Å, without considering spin-orbit interactions. PDOS were calculated using the optimized structure.

Fig.4.13(a) shows the PDOS of each orbit in each layer. These PDOS were obtained by calculating the PDOS of the In atoms in the slab and integrating them for each In layer. It can be seen that the p-orbitals and s-orbitals of the In 1st layer and the p-orbitals of the In 2nd layer all reduce PDOS by hole doping. The arc-like Fermi surface is derived from the In 1st layer p-orbital and the In 2nd layer p-orbital, while the butterfly-like Fermi surface is derived from the 1st layer s-orbital, the In 2nd layer p-orbital, and the Si surface p-orbital [7, 8]. So hole doping reduces $N(E_F)$ on both Fermi surfaces. In other words, it can be interpreted that the charge transfer by CuPc reduces the $N(E_F)$ and causes a decrease in T_c.

Based on the fact that hole doping lowers T_c, the difference in T_c increase between ZnPc and CuPc is considered. Assuming that there is a common cause of T_c increase other than carrier doping in the adsorption of CuPc and ZnPc, it is possible to explain the experimental fact that the increase in T_c is small in CuPc with a large hole doping amount. If this assumption is correct, when ZnPc is adsorbed, there is almost no decrease in $N(E_F)$ due to hole doping, which is a factor that lowers T_c. On the other hand, in the case of CuPc, hole doping reduces T_c, canceling the increase in T_c due to other factors. As a result, it is considered that T_c increased more in the case of ZnPc adsorption than in the case of CuPc adsorption.

So what is this common cause that raised T_c? What is important is that the increase in T_c is not due to the charge transfer effect and that it is a factor common to both ZnPc and CuPc. Here, it is hypothesized that the origin of T_c enhancement is the push-back effect of organic molecules. In general, the finite potential barrier in the metal surface causes the electron wave function to leak into the vacuum side, and the electron density near the nucleus decreases accordingly. However, when the organic molecules are physically adsorbed to the metal substrate, the exuded electrons are pushed back toward the metal nucleus by Pauli repulsion with the electron orbits of the organic molecules. This is called the push-back effect, and is a universal phenomenon observed in many systems [33]. In particular, the push-back effect is expected to work strongly for molecules such as MPc, which have a planar shape that adsorbs flat to the substrate and have a

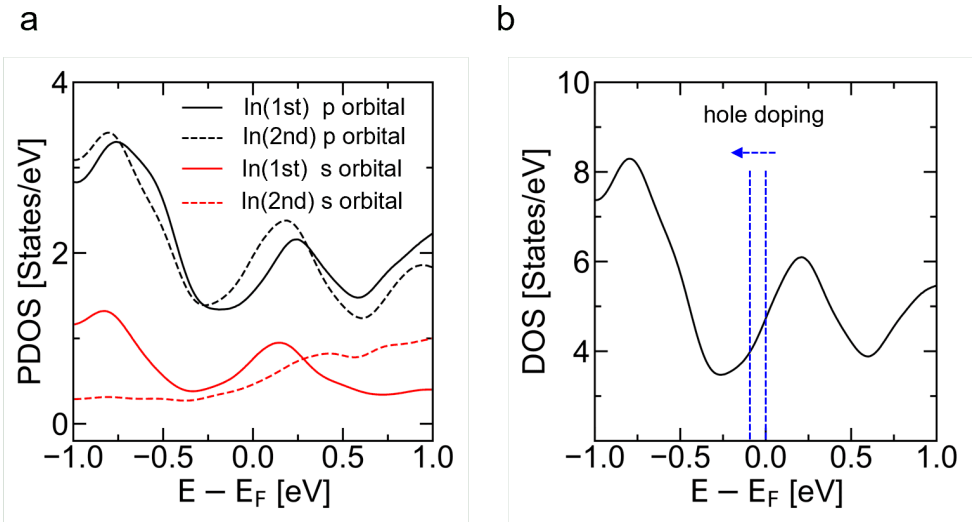

Figure 4.13 **Energy dependence of DOS of $(\sqrt{7}\times\sqrt{3})$-In obtained by** *ab initio* **calculations.** (a) DOS projected onto individual orbitals of In atoms. Black solid/dashed lines: p-orbitals of the first (top) and second (bottom) In layers. Red (gray) solid/dashed lines: s-orbitals of the first and second In layers. (b) Summation of PDOS in (a).

π orbital with an orbital perpendicular to the sample surface. By depositing ZnPc or CuPc, the leaked electrons from the In surface are pushed back to the vicinity of the In nucleus and the electron density near the In nucleus increases (Fig.4.14). As a result, the density of states per unit volume $N(E_F)$ and the attractive potential between electrons V are increased, and thus T_c is considered to have increased. It has been reported that in intercalation compounds of alkali metals and graphite, when the lattice spacing of graphite decreases, the density of electrons responsible for the intercalation band near the lattice increases, resulting in increased electron-phonon interaction and higher T_c [34, 35]. A similar phenomenon is thought to occur in surface systems by organic molecular adsorption.

The amount of change in T_c can be expressed by the following equation using Eq.4.6.

$$\frac{dT_c}{T_c} = \left(\frac{1}{N\left(E_F\right) V} \right) \frac{dV}{V} \tag{4.7}$$

Since the typical value of $N(E_F)V$ in BCS superconductors is 0.2 [31], increasing T_c from 2.81 K to 3.13 K requires a 2 % increase in $N(E_F)V$. This is considered to be a realistic value. However, it is difficult to obtain this value from the first principle, and verification of this hypothesis is a future task.

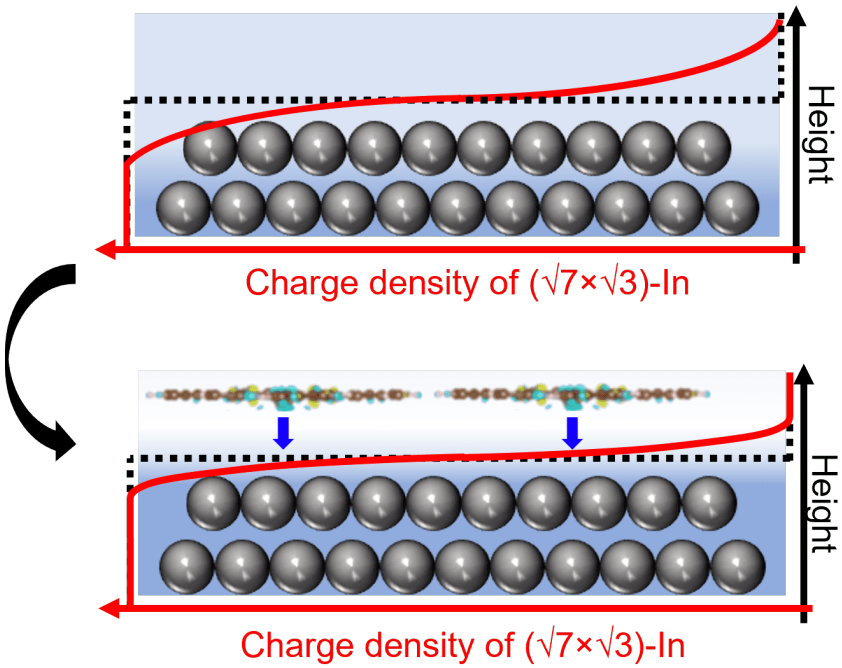

Figure 4.14 **Schematic diagram of push-back effect by MPc adsorption.** Electrons penetrating into the vacuum region are pushed back to the metal side by Pauli repulsion, resulting in an increase in DOS per unit volume and electron density near the metal lattice.

4.9 Conclusion

In this chapter, we report transport measurements of $\left(\sqrt{7} \times \sqrt{3}\right)$-In adsorbed with ZnPc and show that ZnPc adsorption increases the T_c by up to 11 %. This value exceeds the previously reported increase in T_c due to CuPc adsorption. Furthermore, STM measurements confirmed that the film structure of ZnPc is the same as that of MPc in previous studies. On the other hand, ARPES measurements and *ab initio* calculations show that the amount of charge transfer by ZnPc is clearly less than that by CuPc. These experimental facts indicate that the charge transfer between $\left(\sqrt{7} \times \sqrt{3}\right)$-In and organic molecules is not the origin of the T_c increase. Rather, the energy dependence of the PDOS of $\left(\sqrt{7} \times \sqrt{3}\right)$-In obtained by *ab initio* calculations suggests that hole doping by organic molecules lowers the T_c of $\left(\sqrt{7} \times \sqrt{3}\right)$-In. In this study, we propose the push-back effect by organic molecules as the origin of the T_c increase. The push-back effect is a universal effect in adsorption systems on surfaces, which explains why the T_c increases for both CuPc and ZnPc adsorption. Our results provide important clues to understanding the modulation of T_c observed in various other surface/interface atomic-layer superconductors.

Chapter 5 Effect of PTCDA adsorption on atomic-layer superconductors

5.1 Background and the purpose

As introduced in Chapter 4, atomic-layer superconductivity is affected by the adsorption of organic molecules in various ways. Conventionally, charge transfer and spin magnetic moment were considered to be the two main factors affecting T_c due to organic molecule adsorption, but the results of the research in Chapter 4 reveal that other effects such as push-back effects must also be considered. On the other hand, the adsorption structure of organic molecules is also expected to affect superconductivity through effects such as potential modulation of conduction electrons. Although previous studies [20] have discussed the effect of adsorption structure on T_c, the spin magnetic moment is involved in this phenomenon, which complicates the issue. Therefore, in order to investigate the influence of adsorption structure, it is desirable to use organic molecules that have a different structure from MPc and do not have spin.

In this study, 3,4,9,10-Perylenetetracarboxylic dianhydride (PTCDA) was chosen as an organic molecule to clarify the effect of the adsorption structure of organic molecules on the T_c of atomic-layer superconductors. PTCDA is suitable for this purpose because it does not have a spin magnetic moment, so there is no need to consider the effect of exchange interactions on superconductivity.

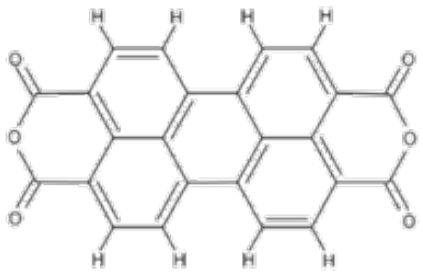

Figure 5.1 **Molecular structure of PTCDA** [36].

The molecular structure of PTCDA is shown in Fig.5.1 [36].PTCDA is a flat organic molecule with a two-fold symmetric structure and acid anhydride groups at both ends. PTCDA generally adsorbs flat to the substrate surface and forms various film structures due to competition between molecule-substrate and intermolecular interactions [37]-[42]. Intermolecular hydrogen bonding due to acid anhydride groups has been pointed out as the reason for the various structures [37]. In other words, strong directional interactions between molecules, including the influence of the substrate, result in the appearance of various structures. Fig.5.2(a) shows an STM image of a typical film structure of PTCDA [38]. This zigzag structure is called a herringbone structure and appears when the intermolecular substrate effects are weak, similar to the bulk phase. On the other hand, square structures, which are stabilized by intermolecular substrate interactions, have also been identified (Fig.5.2(b)) [37, 39]. Furthermore, the coexistence of square and herringbone structures has also been confirmed, and it has been reported that the herringbone structure is modulated at the boundary to fit the square structure (Fig.5.2(c)) [37]. Thus, PTCDA exhibits a variety of structures depending on molecular symmetry and hydrogen bonding by acid anhydride groups.

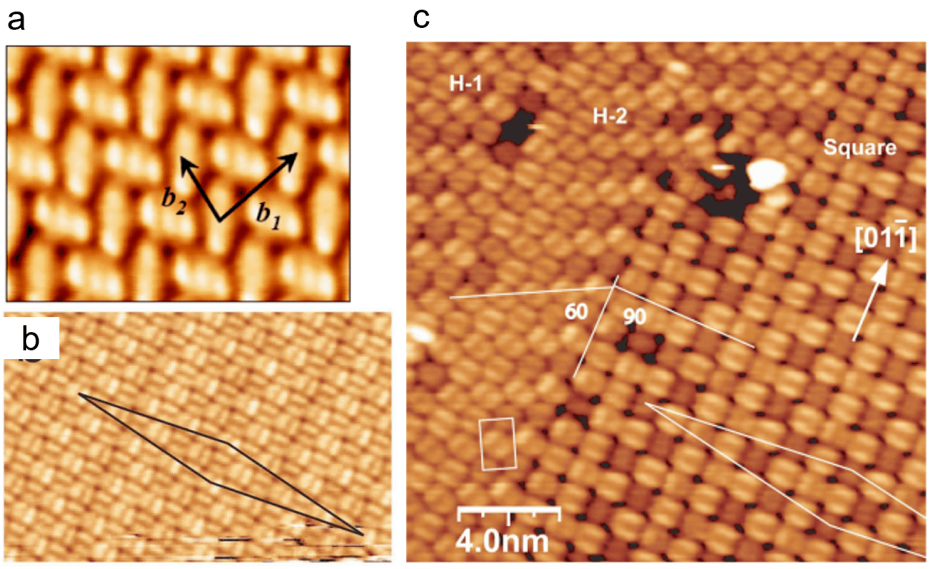

Figure 5.2 **Molecular thin film structure of PTCDA.** (a) STM image of PTCDA herringbone structure on Pb/Si(111) [38]. (b) STM image of PTCDA square structure on Ag/Si(111). (c) STM image of the mixture of PTCDA herringbone and square structure on Ag/Si(111). (b) and (c) were quoted from [37].

5.2 Sample preparation

The $(\sqrt{7} \times \sqrt{3})$-In samples were prepared in the same method as for transport, STM and ARPES measurements (see Section 4.3). PTCDA with a purity > 98 % was adopted as the adsorbed molecule. The deposition method is also the same as in Chapter 4. The coverage of PTCDA in the samples used for transport measurements was estimated using STM measurements. Also, the PTCDA coverage of the sample used in ARPES was estimated by fitting with Eq.5.1 from In 4d core level spectroscopy,

$$I = I_0 \exp\left(-\frac{t}{\lambda}\right) \tag{5.1}$$

where I_0, I, t, and λ denote the photoelectron intensity on the clean surface, the photoelectron intensity after adsorption, the film thickness, and the photoelectron mean free path in PTCDA, respectively. The value of the mean free path (λ = 6 Å) was taken from Ref.[43]. One monolayer (ML) was defined as the coverage that completely covers $(\sqrt{7} \times \sqrt{3})$-In.

5.3 T_c change due to PTCDA adsorption

Transport measurements were performed to clarify the effect of PTCDA adsorption on T_c. The same method as in Chapter 4 was adopted for the sample electrode preparation and measurement method.

Fig.5.3(a) plots the temperature dependence of the sample sheet resistance for each amount of adsorbed PTCDA. The T_c of the pristine $(\sqrt{7} \times \sqrt{3})$-In (red line) was 2.84 K. As the PTCDA coverage was increased, a marked decrease in T_c was confirmed, and it decreased to T_c = 1.96 K at a coverage θ = 0.9 ML (blue line). In addition, the normal resistance value R_n of the sample increased remarkably in the temperature range $T > T_c$. This R_n was obtained by fitting Eq.3.20 (see subsection 3.4.3). R_n of the pristine $(\sqrt{7} \times \sqrt{3})$-In was 29.0 Ω, but as the coverage increased, it decreased exponentially to 83.7 Ω at coverage θ = 0.3 ML and 230.1 Ω at θ = 0.6 ML. and reached 1048.6 Ω at θ = 0.9 ML. Fig.5.3(b) shows the temperature dependence of the sheet resistance of the sample when the coverage is increased to θ = 1.9 ML. The sheet resistance increases with decreasing temperature and exceeds 57.5 kΩ at T = 1.8 K. This trend was reproduced when the same experiment was repeated with a different sample. These results are summarized in Fig.5.3(c). It can be confirmed that the resistance value increases remarkably as the PTCDA coverage increases from the pristine $(\sqrt{7} \times \sqrt{3})$-In. Generally, the critical sheet resistance of the superconducting-insulator transition in a general two-dimensional system is given by the following equation [48].

$$R_c = \frac{h}{4e^2} = 6.45\ k\Omega \tag{5.2}$$

Therefore, it is likely that the increase in the sheet resistance changed the conductive properties to that of an insulator.

Fig.5.3(d) and (e) plot the changes in R_n and T_c of $(\sqrt{7}\times\sqrt{3})$-In as a function of the coverage of PTCDA. Data for ZnPc adsorbed $(\sqrt{7}\times\sqrt{3})$-In are also plotted for comparison [see Chapter 4]. R_n at PTCDA coverage θ = 1.9 ML was taken from the normal resistance 57.5 kΩ at 1.8 K. With ZnPc, the increase in R_n was about 39 % when 1.5 ML was adsorbed, but with the adsorption of PTCDA, it increased about 2000 times from R_n = 28.9 Ω of the pristine $(\sqrt{7}\times\sqrt{3})$-In. In addition, as shown in Fig.5.3(e),

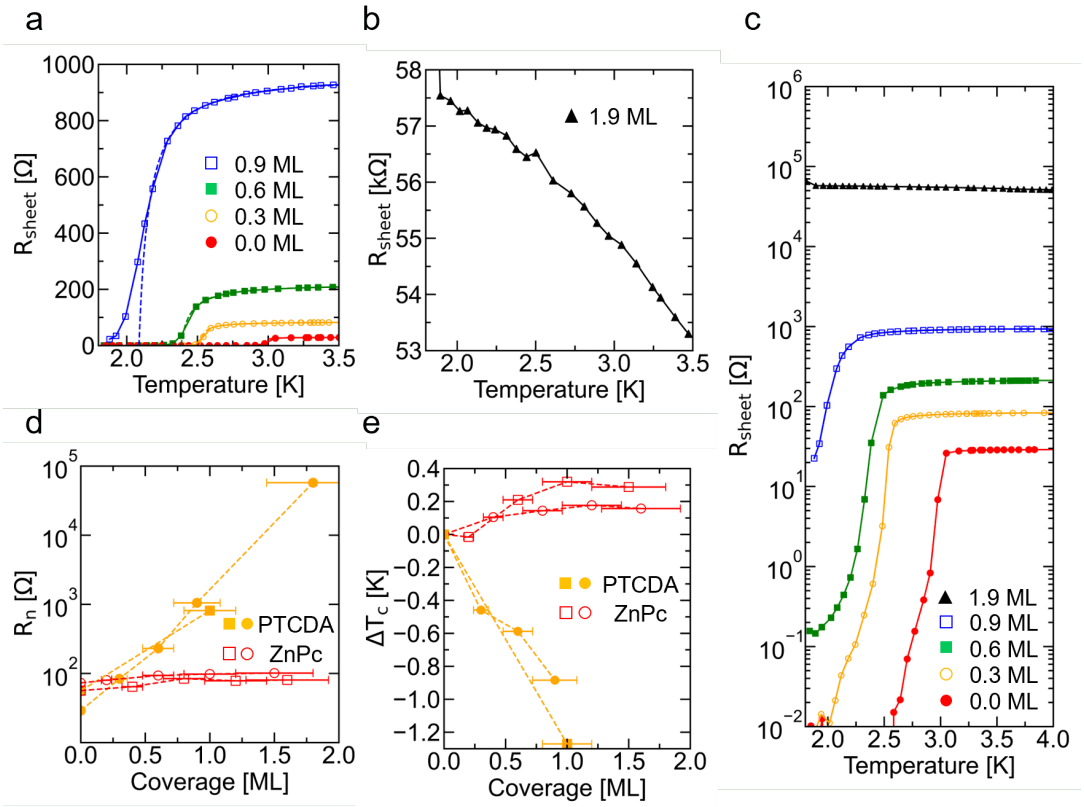

Figure 5.3 **Transport measurements of $(\sqrt{7}\times\sqrt{3})$-In before and after adsorption of PTCDA molecules.**(a) Temperature dependences of the sheet resistance of $(\sqrt{7}\times\sqrt{3})$-In acquired for different coverages of PTCDA. The dashed lines are the fits to thermal fluctuation theories of 2D superconductivity. (b) Temperature dependences of the sheet resistance of PTCDA (1.9 ML) on $(\sqrt{7}\times\sqrt{3})$-In. In (c), the results of (a) and (b) are plotted together. The y-axis is a log scale. (d) Variation of R_n as a function of PTCDA coverage (solid orange circles/ squares). The result of the previous experiment using ZnPc [Chapter.4] is also plotted (open red circles/ squares). (e) Variation of ΔT_c as a function of PTCDA coverage and ZnPc coverage.

adsorption of PTCDA causes a rapid decrease in T_c. The results of this experiment suggest that the adsorption of PTCDA introduces disorder in $(\sqrt{7} \times \sqrt{3})$-In, which increases the sample resistance and suppresses superconductivity. This result is unexpected since only weak interactions such as van der Waals forces generally work between organic molecules and metal surfaces. To elucidate the cause, it is necessary to obtain information on charge transfer and chemical bonding associated with PTCDA adsorption.

5.4 Charge transfer and chemical bonding between PTCDA and $(\sqrt{7} \times \sqrt{3})$-In

Photoelectron spectroscopy measurements were performed to evaluate charge transfer and chemical bonding between PTCDA and $(\sqrt{7} \times \sqrt{3})$-In; the former from the change of the Fermi surface of $(\sqrt{7} \times \sqrt{3})$-In due to PTCDA adsorption and the latter from the shift of the core level of In, O, C atoms composing the top surface of $(\sqrt{7} \times \sqrt{3})$-In and PTCDA. Measurements were carried out at the Sakamoto laboratory of Osaka University as joint research. All measurements were performed at a sample temperature of 20 K under a UHV environment ($< 10^{-8}$ Pa) using the Bloch beamline owned by MAX IV, a synchrotron radiation facility in Sweden. Synchrotron radiation with an energy of 650 eV in the X-ray region was used for core-level measurements of O 1s and C 1s of PTCDA, and synchrotron radiation with an energy of 40 eV in the ultraviolet region was used for other measurements. The energy resolution and wavenumber resolution of the hemispherical electrostatic analyzer in ARPES measurements are 5.5 meV and 0.0025 Å^{-1}.

As mentioned above, the adsorption of PTCDA greatly increased the resistance of $(\sqrt{7} \times \sqrt{3})$-In and strongly suppressed superconductivity. Therefore, we first measured the Fermi surface of $(\sqrt{7} \times \sqrt{3})$-In after PTCDA adsorption by ARPES and investigated whether the structure of $(\sqrt{7} \times \sqrt{3})$-In was retained. Fig.5.4(a) is the pristine $(\sqrt{7} \times \sqrt{3})$-In Fermi surface. Two Fermi surfaces, arc-like and butterfly-like Fermi surfaces, can be confirmed. Fig.5.4(b) shows the arc-like Fermi surface after PTCDA adsorption for 0.6, 1.1 and 2.0 ML. There is no significant change in the Fermi surface at all adsorption amounts other than the background increase due to molecular adsorption. In other words, the structure of $(\sqrt{7} \times \sqrt{3})$-In is maintained even when PTCDA is deposited up to 2.0 ML, suggesting that there is no chemical bonding due to orbital hybridization.

The charge transfer was estimated from the size change of the arc-like Fermi surface. Fig.5.4(c) shows the MDCs measured along the black arrows in Fig.5.4(b) for each coverage. Peaks due to the arc-like Fermi surface can be confirmed at about $k_y = \pm$ 0.46 Å^{-1} for all coverages. Fig.5.4(d) shows the MDCs within the gray box in Fig.5.4(c), where this peak slightly shifts as the coverage of PTCDA increases. The shifts from the pristine $(\sqrt{7} \times \sqrt{3})$-In were -0.0022 ± 0.0005 Å^{-1} (0.3 ML), -0.0030 ± 0.0002 Å^{-1}

(0.6 ML), -0.0048 ± 0.0025 Å^{-1} (1.1 ML), -0.0103 ± 0.0002 Å^{-1} (2.0 ML). These errors were determined by function fitting. At 2.0 ML, where the maximum peak shift $\Delta k_F = -0.0103 \pm 0.0020$ Å^{-1}, the charge transfer per molecule Δn_{mol} is -0.89 ± 0.17 e (see Section 4.6). Here, we assumed that only the molecules directly above the In layer contribute to the electric field transfer. This hole doping amount corresponds to 58 % of the value obtained for CuPc adsorption.

Fig.5.5(a) shows the photoelectron intensity of the $(\sqrt{7} \times \sqrt{3})$-In sample measured by varying the coverage of PTCDA. In addition to the peak near 1 eV observed in the pristine $(\sqrt{7} \times \sqrt{3})$-In, a new peak can be confirmed at the energy position indicated by

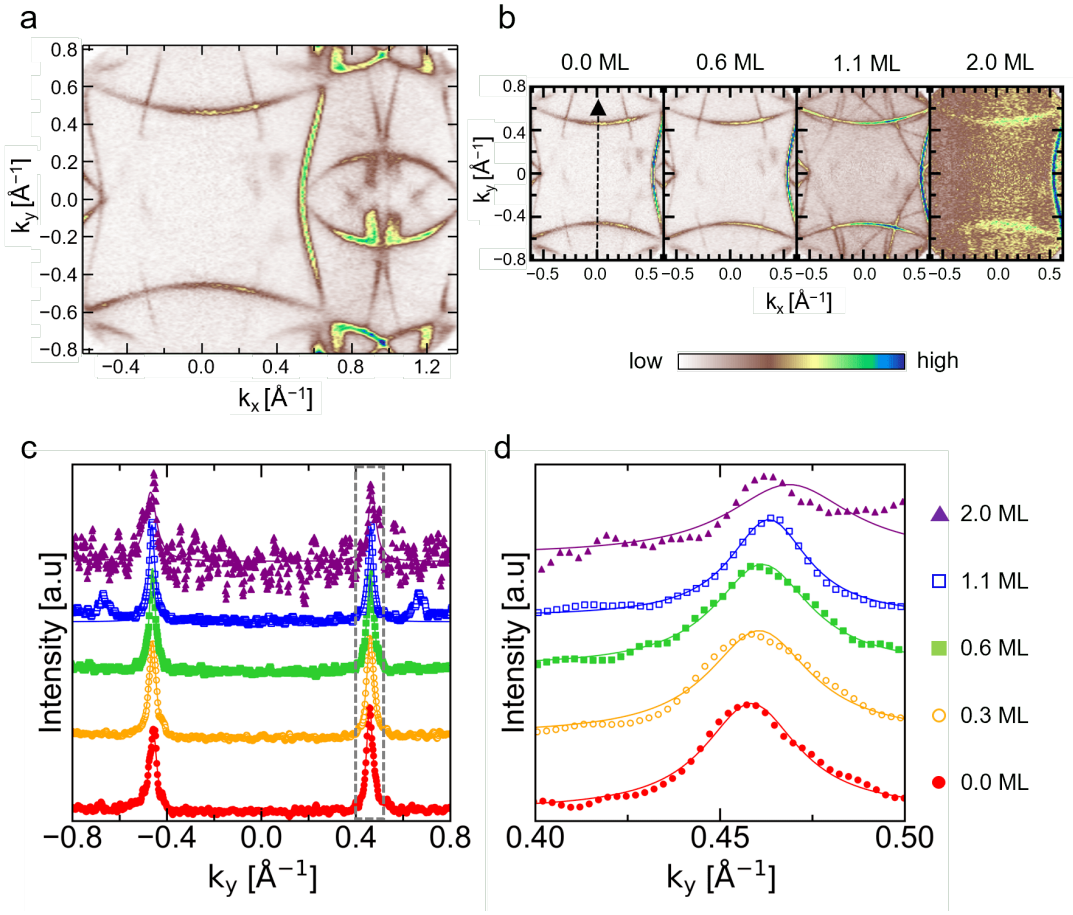

Figure 5.4 **ARPES measurements of $(\sqrt{7} \times \sqrt{3})$-In before and after adsorption of PTCDA molecules.**(a) Photoelectron mapping of the pristine $(\sqrt{7} \times \sqrt{3})$-In Fermi surfaces which consist of arc-like and butterfly-like Fermi surface in momentum space. (b) Photoelectron mappings of arc-like Fermi surface acquired for different PTCDA coverages. (c) MDCs obtained along the black arrow ($k_x = 0$ Å^{-1}) in (b). Solid red circles: 0 ML, open orange circles: 0.3 ML, solid green squares: 0.6 ML, open blue squares: 1.1 ML, solid purple triangles: 2.0 ML. (d) is the MDC inside the grey dashed frame in (c).

the dotted line. Since this peak intensity increases as the amount of adsorption increases, it is assigned to the molecular orbital of PTCDA. The energy at the peak position shows good agreement with previous studies [44]. No peak shift occurred at a coverage of 0 ML $\leq \theta \leq$ 2.0 ML, and a new electronic state due to orbital hybridization between PTCDA and $(\sqrt{7} \times \sqrt{3})$-In could not be confirmed.

Finally, core-level measurements were performed. Fig.5.5(b-d) show results for In 4d, O 1s and C 1s core-level measurements. As can be seen in Fig.5.5(b), the In 4d spectra did not shift after PTCDA adsorption, indicating the absence of chemical bonding at the

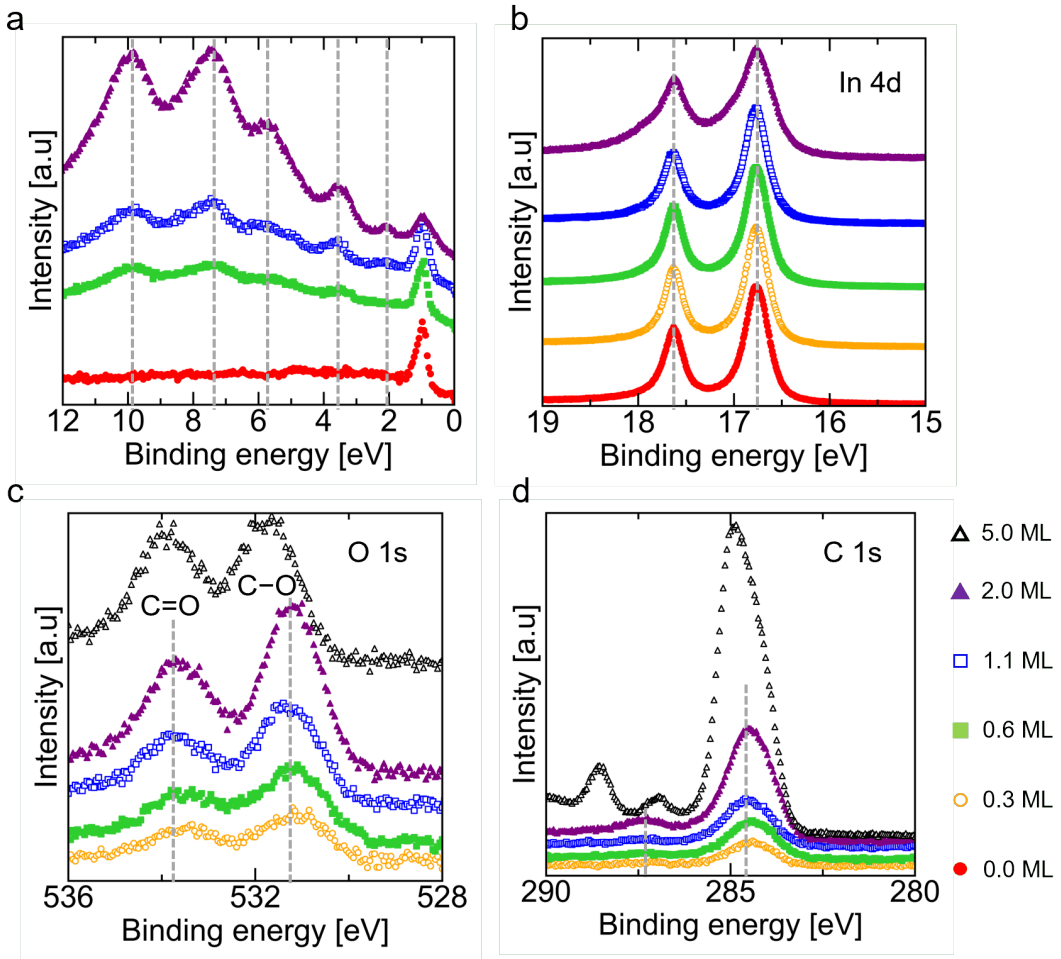

Figure 5.5 **PES measurements of PTCDA adsorption on $(\sqrt{7} \times \sqrt{3})$-In surface.**(a) Molecular orbital spectra. Grey dashed lines indicate molecular orbitals of PTCDA. (b) In 4d core-level spectra for $(\sqrt{7} \times \sqrt{3})$-In adsorbed PTCDA layers of different thickness. (c) O 1s and (d) C 1s core-level spectra for PTCDA layers of different thickness on $(\sqrt{7} \times \sqrt{3})$-In surface. Grey dashed lines indicate core-level peaks. Solid red circles: 0 ML, open orange circles: 0.3 ML, solid green squares: 0.6 ML, open blue squares: 1.1 ML, solid purple triangles: 2.0 ML, open black triangles: 5.0 ML.

In atoms. On the other hand, two peaks at the O 1s of PTCDA were confirmed. The peak at approximately $E_b = 534$ eV corresponds to O double-bonded to C, and the peak at approximately $E_b = 531$ eV corresponds to O single-bonded to C. Compared to 5.0 ML, both two peaks were shifted to the lower binding energy side at coverage below 2.0 ML, where interaction between molecules and substrates may occur. Similarly, C 1s spectra were also observed to shift below 2.0 ML. However, these are due to the electron doping of PTCDA by charge transfer effects and the process of energy loss due to the interaction with the outer shell electrons when the photoelectrons are emitted, not due to chemical bonding [49].

These results are summarized as follows. 1) The $\left(\sqrt{7} \times \sqrt{3}\right)$-In structure is retained after PTCDA adsorption. 2) There is a charge transfer of $\Delta n_{mol} = -0.89 \pm 0.17$ e per molecule. 3) There is no chemical bond between PTCDA and the topmost In atoms, and the PTCDA thin film is physically adsorbed on $\left(\sqrt{7} \times \sqrt{3}\right)$-In.

5.5 PTCDA molecular film structure on $\left(\sqrt{7} \times \sqrt{3}\right)$-In surface

In order to investigate the cause of the rapid increase in sample resistance due to PTCDA, which was mentioned in Section 5.3, we measured the molecular film structure using LT-STM. LT-STM was used as the equipment. The sample temperature during the measurement was 78 K and 4.7 K, and a PtIr-tip was used. There was no difference in the PTCDA molecular film structure depending on the sample temperature.

Fig.5.6(a) shows an STM image of a PTCDA thin film (0.8 ML) grown on the $\left(\sqrt{7} \times \sqrt{3}\right)$-In surface. As can be seen from the dotted line, the PTCDA thin film tends to grow in the direction of the Si(111) crystal axis. It is suggested from the STM image, that PTCDA thin films with two different heights are grown on the same terrace. These correspond to the first layer (within the red dotted line frame in Fig.5.6(a)) and the second layer (within the blue dotted line frame in Fig.5.6(a)) of the PTCDA thin film. Fig.5.6(b) shows the height profile measured on the black arrow in Fig.5.6(a). The heights of the first and second layers of the PTCDA thin film are 20 pm and 240 pm, respectively, compared to the $\left(\sqrt{7} \times \sqrt{3}\right)$-In surface. In the STM image, the first layer appears to be about the same height as the surrounding $\left(\sqrt{7} \times \sqrt{3}\right)$-In, but it doesn't mean that the molecules are adsorbed on the lower level by destroying the outermost In atomic-layer. This is because 1) there is no chemical bond between PTCDA and $\left(\sqrt{7} \times \sqrt{3}\right)$-In as described in Section 5.4, and 2) if the In atomic-layer is destroyed, many In clusters should form on the surface. The phenomenon that the adsorbed PTCDA film appears very low in STM images has also been reported in other systems [38].

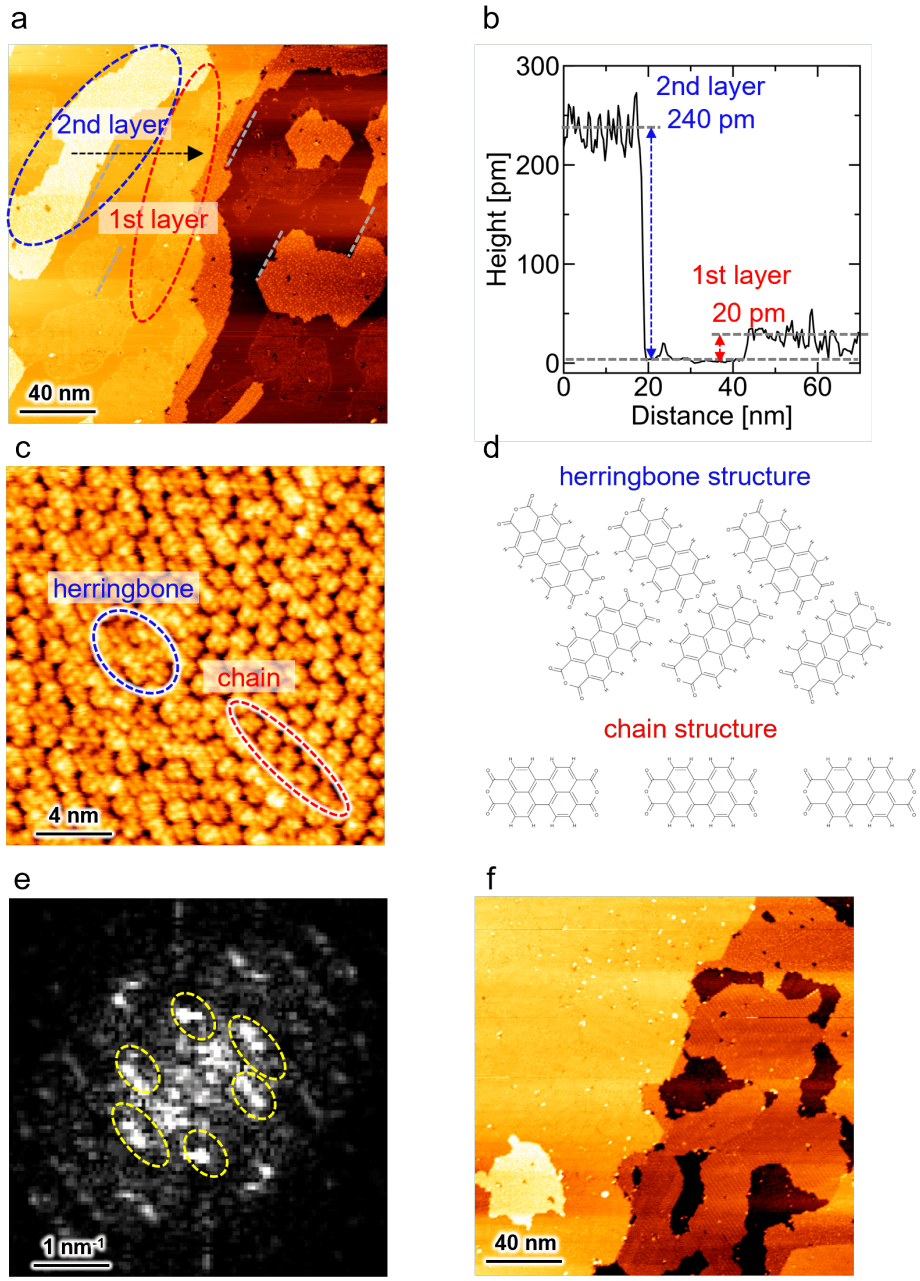

Figure 5.6 **PTCDA molecular film structure on $(\sqrt{7} \times \sqrt{3})$-In.** (a) STM image of PTCDA thin film (0.9 ML) grown on $(\sqrt{7} \times \sqrt{3})$-In (200 × 200 nm^2, $V_s = -2.0$ V, $I_t = 10$ pA, T = 4.7 K). The gray dotted line indicates the crystallographic orientation of the substrate. The red and blue dotted circles indicate the first and second layers of PTCDA film. (b) shows the height profile along the black arrow in (a). (c) STM image of PTCDA film structure on $(\sqrt{7} \times \sqrt{3})$-In (20 × 20 nm^2, $V_s = -2.0$ V, $I_t = 10$ pA, T = 78 K). The red and blue dotted frame indicate the chain and herringbone structure. (d) PTCDA chain and herringbone structural models. (e) is FFT image of (c) (5 × 5 nm^{-2}). The spots within the yellow dotted frame reflect the subtle periodic structure of the film structure. (d) STM image of PTCDA thin film (1.6 ML) grown on $(\sqrt{7} \times \sqrt{3})$-In (200 × 200 nm^2, $V_s = -2.0$ V, $I_t = 10$ pA, T = 4.7 K).

Fig.5.6(c) shows the STM image of the first layer of the PTCDA film, and the assembling structure of PTCDA can be confirmed. The molecular film has a structure similar to the energetically stable herringbone structure (inside the blue dotted line in Fig.5.6(c)), but its periodicity is poor, and the intermolecular distance and angle are inhomogeneous. In addition to the herringbone structure, the PTCDA film also contains a chain structure in which the acid anhydride groups of PTCDA are oriented facing each other (inside the red dotted line in Fig.5.6(c)). A schematic diagram of this herringbone structure and chain structure is shown in Fig.5.6(d). The chain structure is energetically unstable due to Coulombic repulsion between the polarized anhydride groups, and the intermolecular distance is larger than that of the herringbone structure. This chain structure is not generally observed on metal surfaces, but is sometimes observed on directional surface structures such as Si(111)-(4×1)-In surfaces [46].

Fig.5.6(e) shows the results of fast Fourier transform (FFT) of the STM image in Fig.5.6(c). Broad peaks with approximately 6-fold symmetry correspond to both herringbone and chain structures. The broadening of the peak width indicates that the PTCDA film maintains some degree of periodicity but has a strongly disordered structure. Also, elongated peaks aligned in one direction mean that the molecular film includes a two-fold symmetry structure. This two-fold symmetry is thought to be derived from the rectangular molecular shape of PTCDA.

So far, we have shown that a chain structure partially appears in the PTCDA film which is energetically unstable due to Coulomb repulsion. Since PTCDA generally forms a herringbone structure with good periodicity when the interaction with the substrate is weak, such an unnatural structure suggests that the interaction with the substrate surface is somewhat strong. In Section 5.4, we found that there is no chemical bond between PTCDA and $(\sqrt{7} \times \sqrt{3})$-In, but there exists a finite charge transfer. From this, it is suggested that Coulomb attraction acts between the molecule and the surface. It is likely that an irregular structure containing energetically unstable chain structures appears due to multiple factors such as the Coulomb repulsion between PTCDA molecules, the difference in symmetry, and lattice mismatch between $(\sqrt{7} \times \sqrt{3})$-In and PTCDA.

When 1.6ML of PTCDA thin film was deposited and STM measurement was performed, the $(\sqrt{7} \times \sqrt{3})$-In surface was completely covered with PTCDA as shown in Fig.5.6(f). In the transport measurement, the sample became an insulator due to the adsorption of 1.9 ML of PTCDA. At this point the PTCDA film completely covered the $(\sqrt{7} \times \sqrt{3})$-In surface.

5.6 Discussion

In Chapter 4, it was mentioned that when ZnPc was adsorbed on the $(\sqrt{7} \times \sqrt{3})$-In surface, the T_c increase of about 11 % was observed, which is the largest in the MPc system. Also, the increase in R_n is only about 39 % at maximum. On the other hand, the T_c of $(\sqrt{7} \times \sqrt{3})$-In decreased rapidly due to the adsorption of PTCDA, and at $\theta = 1.9$ ML, the temperature dependence of the sheet resistance changed like that of an insulator. In addition, along with this, the normal resistance value increased to about 2000 times. This result indicates that ZnPc only acts as a very weak scatterer for conduction electrons in the In atomic-layer, whereas PTCDA acts as a strong scatterer. It is surprising to see the result that PTCDA acts as a strong scatterer even though it is physically adsorbed on the $(\sqrt{7} \times \sqrt{3})$-In surface in the same way as ZnPc. In the following, we discuss the cause of strong electron scattering due to PTCDA adsorption.

As can be seen from the STM images, ZnPc forms a square lattice that is well lattice-matched with the In layer on the $(\sqrt{7} \times \sqrt{3})$-In surface. This is probably because ZnPc has four-fold symmetry, while the outermost In atomic-layer of $(\sqrt{7} \times \sqrt{3})$-In also has approximately four-fold symmetry. Therefore, a regular assembling structure can be formed. In this case, according to Bloch's theorem, the conduction electrons are not scattered under the periodic potential. On the other hand, PTCDA is a molecule with 2-fold symmetry, which is different from the substrate, and has polarized anhydride groups at both ends, so the intermolecular interaction is strong and directional. For this reason, it is considered that the disordered assembling structure was formed as a result of interaction and competition with the substrate. In addition, since the acid anhydride group of PTCDA is polarized, a strong electric field can be formed around it. It has been confirmed both theoretically and experimentally that PTCDA on Ag(111) has a strong electrostatic potential distribution due to the polarization of the anhydride group [47]. Due to these reasons, PTCDA electrons are thought to act as strong scatterers for conduction electrons. This effect should be prominent in surface-sensitive atomic-layer materials such as $(\sqrt{7} \times \sqrt{3})$-In.

5.7 Conclusion

In this chapter, we describe transport measurements of $(\sqrt{7} \times \sqrt{3})$-In adsorbed with PTCDA and show that PTCDA adsorption suppresses superconductivity and rapidly increases resistance. It was found that increasing the coverage eventually leads to a transition to an insulating-like state. On the other hand, ARPES measurements of the Fermi surface and core level measurements indicate that $(\sqrt{7} \times \sqrt{3})$-In retains its structure under the PTCDA film and that there is little chemical bonding between the two. Furthermore,

STM measurements show that the PTCDA film structure is not periodic and that there are localized herringbone and chain structures. The seemingly contradictory phenomena of the rapid increase in resistance and the very weak interaction are proposed to be explained by the irregularity of the molecular film array structure and the polarization of the acid anhydride groups of PTCDA. This phenomenon is a clear illustration of the surface sensitivity of atomic layer materials. The present results suggest that the regularity of the organic molecular film structure is important for increasing the T_c of atomic layer superconductors, and provide important guidance for the selection of organic molecules in the future.

References

[1] Jae Whan Park, and Myung Ho Kang, Phys. Rev. Lett. **109**, 166102 (2012).

[2] Jae Whan Park, and Myung Ho Kang, Phys. Rev. B. **92**, 045306 (2015).

[3] Tetsuroh Shirasawa, Shunsuke Yoshizawa, Toshio Takahashi, and Takashi Uchihashi, Phys. Rev. B. **99**, 100502 (2019).

[4] Takashi Uchihashi and Urs Ramsperger, Appl. Phys. Lett. **80**, 4169-4171 (2002).

[5] Toru Hirahara, Taku Komorida, Yan Gu, Fumitaka Nakamura, Hiroshi Idzuchi, Harumo Morikawa, and Shuji Hasegawa, Phys. Rev. B. **80**, 235419 (2009).

[6] Eli Rotenberg, H. Koh, K. Rossnagel, H. W. Yeom, J.Schäfer, B. Jrenzer, M. P. Rocha, and S. D. Kevan, Phys. Rev. Lett. **91**, 246404 (2003).

[7] Takahiro Kobayashi, Yoshitaka Nakata, Koichiro Yaji, Tatsuya Shishidou, Daniel Agterberg, Shunsuke Yoshizawa, Fumio Komori, Shik Shin, Michael Weinert, Takashi Uchihashi, and Kazuyuki Sakamoto, Phys. Rev. Lett. **125**, 176401 (2020).

[8] Ryunosuke Sagehashi, Takahiro Kobayashi, Takashi Uchihashi, Kazuyuki Sakamoto, Surf. Sci. **705**, 121777 (2021).

[9] Tong Zhang, Peng Cheng, Wen-Juan Li, Yu-Jie Sun, Guang Wang, Xie-Gang Zhu, Ke He, Lili Wang, Xucun Ma, Xi Chen, Yayu Wang, Ying Liu, Hai-Qing Lin, Jin-Feng Jia and Qi-Kun Xue, Nat. Phys. **6**, 104 (2010).

[10] Shunsuke Yoshizawa, Howon Kim, Takuto Kawakami, Yuki Nagai, Tomonobu Nakayama, Xiao Hu, Yukio Hasegawa, and Takashi Uchihashi, Phys. Rev. Lett. **113**, 247004 (2014).

[11] Takashi Uchihashi, Puneet Mishra, Masakazu Aono, and Tomonobu Nakayama, Phys. Rev. Lett. **107**, 207001 (2011).

[12] Manabu Yamada, Toru Hirahara, and Shuji Hasegawa, Phys. Rev. Lett. **110**, 237001 (2013).

[13] Shunsuke Yoshizawa and Takashi Uchihashi, J. Phys. Soc. Jpn. **83**, 065001 (2014).

[14] Takashi Uchihashi, Puneet Mishra and Tomonobu Nakayama, Nanoscale Res. Lett. **8**, 167 (2013).

[15] Satoru Ichinokura, Katsuaki Sugawara, Akari Takayama, Takashi Takahashi, and Shuji Hasegawa, ACS Nano. **10**, 2761-2765 (2016).

[16] A. T. Bollinger, G. Dubuis, J. Yoon, D. Pavuna, J. Misewich and I. Božović, Nature **472**, 458 – 460 (2011).

[17] Yu Saito, Yuichi Kasahara, Jianting Ye, Yoshihiro Iwasa, Tsutomu Nojima, Science **350**, 409 – 413 (2015).

[18] Shunsuke Yoshizawa, Emi Minamitani, Saranyan Vijayaraghavan, Puneet Mishra, Yasumasa Takagi, Toshihiko Yokoyama, Hiroaki Oba, Jun Nitta, Kazuyuki Sakamoto, Satoshi Watanabe, Tomonobu Nakayama, and Takashi Uchihashi, Nano Lett. **17**, 2287-2293 (2017).

[19] Takashi Uchihashi, Shunsuke Yoshizawa, Emi Minamitani, Satoshi Watanabe, Yasumasa Takagi and Toshihiko Yokoyama, Mol. Syst. Des. Eng. **4**, 511-518 (2019).

[20] Naoya Sumi, Yoichi Yamada, Masahiro Sasaki, Ryuichi Arafune, Noriaki Takagi, Shunsuke Yoshizawa, and Takashi Uchihashi, J. Phys. Chem. C, **123**, 8951 − 8958 (2019).

[21] Abimbola Ogunsipe, David Maree, Tebello Nyokong, J. Mol. Struct. **650**, 131–140 (2003).

[22] Nthapo Sehlotho, Tebbello Nyokong, J. Mol. Catal A. Chem. **219**, 201–207 (2004).

[23] Meng-Sheng Liao and Steve Scheiner, J. Chem. Phys. **114**, 9780-9791 (2001).

[24] Zahoor Ul Islam, Muhammad Tahir, Waqar Adil Syed, Fakhra Aziz, Fazal Wahab, Suhana Mohd Said, Mahidur R. Sarker, Sawal Hamid Md Ali and Mohd Faizul Mohd Sabri, Energies, **13**, 962 (2020).

[25] J. Kraft, S.L.Surnev, F.P.Netzer, Surf. Sci. **340**, 36-48 (1995).

[26] Shunsuke Yoshizawa, Takahiro Kobayashi, Yoshitaka Nakata, Koichiro Yaji, Kenta Yokota, Fumio Komori, Shik Shin, Kazuyuki Sakamoto and Takashi Uchihashi, Nat. Commun. **12**, 1462 (2021).

[27] Kazuyuki Uchida and Atsushi Oshiyama, Phys. Rev. B **87**, 165433 (2013).

[28] S. Stepanow, P. S. Miedema, A. Mugarza, G. Ceballos, P. Moras, J. C. Cezar, C. Carbone, F. M. F. de Groot, and P. Gambardella, Phys. Rev. B **83**, 220401 (2011).

[29] G. Kresse and J. Furthmüller, Phys. Rev. B **54**, 11169-11186 (1996).

[30] G. Kresse and J. Furthmüller, Computational Materials Science **6**, 15-50 (1996).

[31] M. Tinkham, Introduction to Superconductivity (McGraw-Hill, New York, 1996), 2nd ed..

[32] Paolo Giannozzi, Stefano Baroni, Nicola Bonini, Matteo Calandra, Roberto Car, Carlo Cavazzoni, Davide Ceresoli, Guido L Chiarotti, Matteo Cococcioni, Ismaila Dabo, Andrea Dal Corso, Stefano de Gironcoli, Stefano Fabris, Guido Fratesi, Ralph Gebauer, Uwe Gerstmann, Christos Gougoussis, Anton Kokalj, Michele Lazzeri, Layla Martin-Samos, Nicola Marzari, Francesco Mauri, Riccardo Mazzarello, Stefano Paolini, Alfredo Pasquarello, Lorenzo Paulatto, Carlo Sbraccia, Sandro Scandolo, Gabriele Sclauzero, Ari P Seitsonen, Alexander Smogunov, Paolo Umari1 and Renata M Wentzcovitch, J. Phys. Condens. Matter **21**, 395502 (2009).

[33] Gregor Witte,Simon Lukas, Paul S. Bagus, and Christof Wöll, Appl. Phys. Lett. **87**, 263502 (2005).

[34] J. S. Kim, L. Boeri, J. R. O' Brien, F. S. Razavi, and R. K. Kremer, Phys. Rev. Lett. **99**, 027001 (2007).

[35] Gianni Profeta, Matteo Calandra, and Francesco Mauri, Nat. Phys. **8**, 131-134 (2012).

[36] CAO Liang, ZHANG WenHua, HAN YuYan, CHEN TieXin, ZHENG ZhiYuan, WAN Li, XU FaQiang, IBRAHIM Kurash, QIAN HaiJie and WANG JiaOu, Chinese Sci Bull. **56**, 3575-3577 (2011).

[37] J. B. Gustafsson, H. M. Zhang, and L. S. O. Johansson, Phys. Rev. B **75**, 155414 (2007).

[38] N. Nicoara, J Méndez and J M Gómez-Rodríguez, Nanotechnology. **27**, 365706 (2016).

[39] S. Mannsfeld, M. Törker, T. Schmitz-Hübsch, F. Sellam, T. Fritz, and K. Leo, Org. Electron. **2**, 121-134 (2001).

[40] H. M. Zhang and L. S. O. Johansson, J. Chem. Phys. **144**, 124701 (2016).

[41] Dongchul Shin, Zheng Wei, Hyungjoon Shim, Geunseop Lee, Appl. Surf. Sci. **372**, 87–92 (2016).

[42] Zheng Wei, Heechul Lim, and Geunseop Lee, Appl. Phys. Lett. **98**, 071912 (2011).

[43] Tina Graber, Frank Forster, Achim Schöll, Friedrich Reinert, Surf. Sci. **605**, 878–882 (2011).

[44] S. Duhm, A. Gerlach, I. Salzmann, B. Bröker, R.L. Johnson, F. Schreiber, N. Koch, Org. Electron. **9**, 110-118 (2008).

[45] J. B. Gustafsson, H. M. Zhang, E. Moons, and L. S. O. Johansson, Phys. Rev. B **75**, 155413 (2007).

[46] Dongchul Shin, Zheng Wei, Hyungjoon Shim, Geunseop Lee, Appl. Surf. Sci. **372**, 87–92 (2016).

[47] Prokop Hapala, Martin Švec, Oleksandr Stetsovych, Nadine J. van der Heijden, Martin Ondráček, Joost van der Lit, Pingo Mutombo, Ingmar Swart and Pavel Jelínek, Nat. Commun. **7**,11560 (2016).

[48] D. B. Haviland, Y. Liu, and A. M. Goldma, Phys. Rev. Lett. **62**, 2180-2183 (1989).

[49] 稲垣俊輔, 修士論文 (2023).

Chapter 6 Conclusions

In this study, we adsorbed organic molecules ZnPc and PTCDA on the surface of atomic-layer superconductor $\left(\sqrt{7}\times\sqrt{3}\right)$-In and measured the change of T_c by transport measurement. $\left(\sqrt{7}\times\sqrt{3}\right)$-In showed an increase in T_c due to the adsorption of ZnPc, and comparison with previous studies revealed that the origin of T_c increase was not the charge transfer proposed in previous studies. On the other hand, when PTCDA was adsorbed on $\left(\sqrt{7}\times\sqrt{3}\right)$-In, the superconductivity was suppressed, and finally it showed insulator-like conducting properties. This is thought to be caused by irregularities in the thin film structure of organic molecules. These results are summarized below.

6.1 ZnPc adsorbed $\left(\sqrt{7}\times\sqrt{3}\right)$-In

Transport measurements showed that $\left(\sqrt{7}\times\sqrt{3}\right)$-In was increased by ZnPc adsorption. The maximum ΔT_c was observed at a coverage of $\sim$ 1 ML, with an 11 % increase in T_c. This value is 2.7 times higher than ΔT_c due to CuPc adsorption reported in previous studies. Furthermore, from STM measurements, it was observed that the ZnPc thin film on the $\left(\sqrt{7}\times\sqrt{3}\right)$-In surface has a structure similar to that of the CuPc thin film. By ARPES, we investigated the size change of the Fermi surface of $\left(\sqrt{7}\times\sqrt{3}\right)$-In due to ZnPc adsorption, and estimated the amount of charge transfer. As a result, the amount of charge transferred per molecule $\Delta n_{mol} = -0.31 \pm 0.59$e. This is about 20 % compared to the charge transfer $\Delta n_{mol} = -1.53 \pm 0.32$e per molecule of CuPc. The charge transfer per molecule of ZnPc and CuPc obtained by *ab initio* calculations were $\Delta n_{mol} = -0.76$e and $\Delta n_{mol} = -1.61$e, respectively. This result qualitatively agrees with the ARPES results in that the amount of charge transferred by ZnPc is clearly smaller than that by CuPc.

These results show that $|\Delta n_{mol}|$(ZnPc) $<$ $|\Delta n_{mol}|$(CuPc) while ΔT_c(ZnPc) $>$ ΔT_c(CuPc). From this, we concluded that the origin of the T_c increase due to the adsorption of organic molecules is not due to the charge transfer. On the other hand, the origin of the increase in T_c has not been clarified. In this study, we proposed the push-back effect of organic molecules as the origin of T_c increase. It is likely that the push-back effect of organic molecules increases the density of states per unit volume $N(E_F)$ and the attractive potential V between electrons, resulting in an increase in T_c.

6.2 PTCDA adsorbed $\left(\sqrt{7}\times\sqrt{3}\right)$-In

Transport measurements show that PTCDA adsorption suppresses the superconductivity of $\left(\sqrt{7}\times\sqrt{3}\right)$-In. It should be noted that PTCDA adsorption significantly increased the resistance of $\left(\sqrt{7}\times\sqrt{3}\right)$-In. Finally, at a coverage of 1.9 ML, the conduction of $\left(\sqrt{7}\times\sqrt{3}\right)$-In showed insulating properties. On the other hand, from the Fermi surface measurement by ARPES, the shape of the Fermi surface of $\left(\sqrt{7}\times\sqrt{3}\right)$-In does not change even after PTCDA adsorption, so the structure of $\left(\sqrt{7}\times\sqrt{3}\right)$-In is retained under the PTCDA film. It was found that no peak shift due to chemical bonding between PTCDA and $\left(\sqrt{7}\times\sqrt{3}\right)$-In was detected from core-level measurements. We conclude that PTCDA is physically adsorbed on $\left(\sqrt{7}\times\sqrt{3}\right)$-In due to van der Waals interaction and there is slight charge transfer. STM measurements revealed random arrangement of PTCDA on the $\left(\sqrt{7}\times\sqrt{3}\right)$-In surface.

Although the interaction between PTCDA and $\left(\sqrt{7}\times\sqrt{3}\right)$-In was weak, the adsorption of PTCDA significantly increased the resistance. Based on this, we proposed the following hypothesis. PTCDA is randomly arranged on the $\left(\sqrt{7}\times\sqrt{3}\right)$-In surface and polarized at both ends of the molecule. Therefore, PTCDA induces a strong random potential and scatters the conduction electrons of $\left(\sqrt{7}\times\sqrt{3}\right)$-In. It is believed that this caused an increase in resistance and suppression of superconductivity.

6.3 Insight obtained from this study

The results of ZnPc adsorption showed that the origin of the increase in T_c due to adsorption of organic molecules was not hole doping. We mentioned that the push-back effect of organic molecules is a candidate for the origin of the T_c increase. From this, there are two possibilities to further increase the T_c of $\left(\sqrt{7}\times\sqrt{3}\right)$-In: electron doping or enhancement of the push-back effect. As for the former, it is conceivable to increase T_c by adsorbing organic molecules with high donor properties. As for the latter, it is expected to enhance the push-back effect by densely arranging organic molecules with the π-electron system of a benzene ring in a flat configuration.

From the research results of PTCDA adsorption, we proposed that superconductivity is suppressed by the disorder of the molecular film. This result serves as a guideline for selecting organic molecules, in terms of whether or not they are ordered on atomic-layer superconducting materials.

This result will provide important insight for increasing the T_c of atomic-layer superconductors and understanding the mechanism of T_c modulation.

Acknowledgments

With the support and cooperation of Prof. Dr. Takashi Uchihashi and so many others, I was able to pursue my research in the doctoral program. I would like to express my gratitude to them.

My supervisor, Prof. Dr. Uchihashi, accepted me willingly, even though I had not studied superconductivity and transport measurement. I am convinced that being able to study closely with his research style of constructing and clarifying research one by one in a logical and step-by-step manner will be an asset for the rest of my life. Dr. Tomonori Nakamura taught me the importance of always continuing my efforts. Every time I saw Dr. Nakamura always silently continuing his research, I felt a sense of humility. Dr. Ryohei Nemoto eventually took care of me from my fourth year of undergraduate studies to my third year of doctoral studies. I believe that what I learned from Dr. Nemoto is at the root of my current abilities. Student Mr. Wenxuan Qian is a valuable person who gave me the experience of teaching research to others, as I had no junior colleagues. On the other hand, Mr. Qian is my English conversation teacher. I look forward to his further growth and success at Uchihashi Lab. Ms. Tomoko Kobayashi, our secretary, has always supported me behind the scenes. Thanks to Ms. Kobayashi, I was able to proceed with my research comfortably.

My collaborators in this doctoral dissertation, Prof. Dr. Kazuyuki Sakamoto, Prof. Dr. Emi Minamitani, and student Mr. Shunsuke Inagaki of Osaka University, and Dr. Shunsuke Yoshizawa of National Institute for Materials Science, not only provided research results but also allowed this research to grow through fruitful discussions. To Prof. Dr. Sakamoto, I am indebted and enjoyed interacting with him from my fourth year of undergraduate studies to my third year of doctoral studies. I am grateful to Prof. Dr. Minamitani for her very sharp remarks. Mr. Inagaki taught me even the basics of ARPES, of which I lacked knowledge. Dr. Yoshizawa carefully taught me DFT calculations. Seeing him handle experiments, theoretical calculations, and programming on his own made me realize my lack of effort and gave me a chance to grow. The collaborative research with all of you has been a valuable asset for me.

Prof. Dr. Takahide Yamaguchi, Dr. Katsumi Nagaoka, and Prof. Dr. Ryuichi Arafune of the Surface Quantum Phase Materials Group in the National Institute for Materials Science, as well as Dr. Yosuke Sasama and Dr. Taisuke Kageura, who have

moved to a more prosperous position, have taught me how to be a researcher through seminars and daily interaction.

It was an irreplaceable experience for me to be able to live and work in a research environment surrounded by doctors, which I could not have experienced at university while I was in the laboratory. Finally, I would like to express my deepest gratitude to my parents and grandparents for their kindness in sending me off to too-long student life. With the support of my friends, juniors, and seniors who are not listed here, I was able to complete my doctoral dissertation. Thank you very much.